

✓
RADC-TR-76-54
Final Technical Report
March 1976



SPACE OBJECT IMAGING

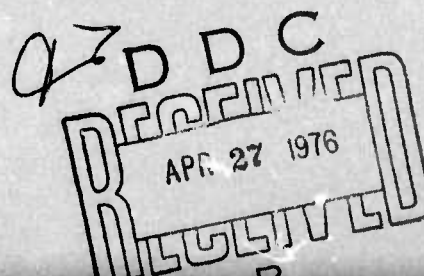
Hughes Research Laboratories

Sponsored by
Defense Advanced Research Projects Agency
ARPA Order 2646

Approved for public release;
distribution unlimited.

The views and conclusions contained in this document are those of the authors and should not be interpreted as necessarily representing the official policies, either expressed or implied, of the Defense Advanced Research Projects Agency or the U. S. Government.

Rome Air Development Center
Air Force Systems Command
Griffiss Air Force Base, New York 13441



AD A 028492

DISCLAIMER NOTICE

THIS DOCUMENT IS THE BEST
QUALITY AVAILABLE.

COPY FURNISHED CONTAINED
A SIGNIFICANT NUMBER OF
PAGES WHICH DO NOT
REPRODUCE LEGIBLY.

This report has been revised by the RADC Information Office (OI) and is releasable to the National Technical Information Service (NTIS). At NTIS it will be releasable to the general public including foreign nations.

This technical report has been reviewed and is approved for publication.

APPROVED:

Donald W. Hanson
DONALD W. HANSON
Project Engineer

ACCESSION for	
NTIS	<input checked="" type="checkbox"/>
DDC	<input type="checkbox"/>
UNCLASSIFIED	<input type="checkbox"/>
JUSTIFICATION	
BY	
DISTRIBUTION/AVAILABILITY CODES	
Dist.	FILE # / SPECIAL
A	

Do not return this copy. Retain or destroy.

SPACE OBJECT IMAGING

C. R. Giuliano
J. A. Jenney
L. Miller
M. E. Pedinoff
D. Y. Tseng
S. M. Wandzura

Contractor: Hughes Research Laboratories
Contract Number: F30602-74-C-0227
Effective Date of Contract: 17 April 1974
Contract Expiration Date: 17 August 1975
Amount of Contract: \$228,000.00
Program Code Number: 5E20
Period of work covered: Apr 74 - Jun 75

Principal Investigator: C. R. Giuliano
Phone: 213 456-6411

Project Engineer: Donald W. Hanson
Phone: 315 330-3145

Approved for public release;
distribution unlimited.

This research was supported by the Defense Advanced Research Projects Agency of the Department of Defense and was monitored by Donald W. Hanson (OCSE), Griffiss AFB NY 13441.

UNCLASSIFIED

SECURITY CLASSIFICATION OF THIS PAGE (When Data Entered)

19 REPORT DOCUMENTATION PAGE		READ INSTRUCTIONS BEFORE COMPLETING FORM
1. REPORT NUMBER RADC-TR-76-54	2. GOVT ACCESSION NO.	3. RECIPIENT'S CATALOG NUMBER
4. TITLE (and Subtitle) SPACE OBJECT IMAGING	5. TYPE OF REPORT & PERIOD COVERED Final Technical Report, 17 Apr 1974 - 16 June 1975	6. PERFORMING ORG. REPORT NUMBER N/A
7. AUTHOR(s) C. R. Giuliano, M. E. Pedinoff J. A. Jenney, D. Y. Tseng L. Miller, S. M. Wandzura	8. CONTRACT OR GRANT NUMBER(s) F30602-74-C-0227 ARPA Order - 2646	9. PROGRAM ELEMENT, PROJECT, TASK AREA & WORK UNIT NUMBERS 62301E 26460301 IAF-2646
9. PERFORMING ORGANIZATION NAME AND ADDRESS Hughes Research Laboratories 3011 Malibu Canyon Road Malibu CA 90265	10. REPORT DATE March 1976	11. NUMBER OF PAGES 206
11. CONTROLLING OFFICE NAME AND ADDRESS Defense Advanced Research Projects Agency 1300 Wilson Blvd Arlington VA 22209	12. SECURITY CLASS. (of this report) UNCLASSIFIED	13a. DECLASSIFICATION/DOWNGRADING SCHEDULE N/A
14. MONITORING AGENCY NAME & ADDRESS (if different from Controlling Office) Rome Air Development Center (OCSE) Griffiss AFB NY 13441	16. DISTRIBUTION STATEMENT (of this Report) Approved for public release; distribution unlimited.	
17. DISTRIBUTION STATEMENT (of the abstract entered in Block 20, if different from Report) Same		
18. SUPPLEMENTARY NOTES RADC Project Engineer: Donald W. Hanson (OCSE) Copies are available in DDC.		
19. KEY WORDS (Continue on reverse side if necessary and identify by block number) Atmospheric Optics, Imaging.		
20. ABSTRACT (Continue on reverse side if necessary and identify by block number) This report consists of two major parts. The first part contains a description of the Seeing Monitor, a system that was designed, fabricated, and tested on this program. The Seeing Monitor is an optical instrument that samples star images on a millisecond time scale and provides information on atmospheric seeing conditions. In this system star images are scanned in orthogonal directions by a spinning reticle wheel and the light transmitted through the wheel is processed to yield the modulation transfer function of the atmosphere, (Cont'd)		

172 600

UNCLASSIFIED

SECURITY CLASSIFICATION OF THIS PAGE(When Data Entered)

the seeing angle, and image wander information. The Seeing Monitor test results show satisfactory performance for stars of visual magnitude up to about 6.5 and a dynamic range for seeing angles of 0.1 to 10 arc seconds.

The second part of the report describes a series of experiments and computer simulations that were performed in preparation for a feasibility demonstration experiment of Polarization Reference Imaging (PRIM) at AMOS. The experiments performed in the laboratory at HRL as well as the ruby laser experiments at AMOS all indicate that the demonstration experiment is feasible. Computer simulations performed on this program provided additional information not available in the experimental phase that impacts the expected PRIMS image quality as a function of speckle averaging, signal to noise, multiple glints, and glint amplitude. The experiments that were performed showed the feasibility of a PRIMS transmitter scheme using short (20-30 nsec) optical pulses and a PRIMS receiver that employs time division multiplexing by way of fiber optic delay lines. The AMOS laser tests demonstrated that the AMOS ruby laser can be made to operate at its maximum pulse repetition rate (20 ppm) in a single longitudinal mode without appreciable loss of output energy.

UNCLASSIFIED

SECURITY CLASSIFICATION OF THIS PAGE(When Data Entered)

PREFACE

This final report was prepared by the Hughes Research Laboratories, Malibu, California under Contract No. F30602-74-C-0227. It describes work performed from 16 April 1974 to 15 July 1975. The Program Manager is C. R. Giuliano who assumed this role in the last half of the program from J. A. Jenney. The authors of this report are listed on the front cover. In addition to the authors we wish to acknowledge the contributions of W. P. Brown, V. Evtuhov, and T. R. O'Meara who served as technical advisors for the whole range of technical problems that arose during the program. We also wish to acknowledge the key contribution of T. Calderone who contributed heavily to the successful implementation and testing of the Hughes Seeing Monitor. Finally we wish to express our appreciation to the Avco Everett Research Laboratories personnel at the ARPA Maui Observation Station (AMOS), especially P. L. Zieske and P. N. Everett whose interest and cooperation during the Seeing Monitor acceptance tests and the ruby laser tests at AMOS ensured that this work was carried out in a satisfactory manner.

TABLE OF CONTENTS

SECTION		PAGE
	LIST OF ILLUSTRATIONS	7
I	INTRODUCTION	11
	A. Background	11
	B. Summary of Report	14
	C. Recommendations for Future Work	17
II	SEEING MONITOR	21
	A. Introduction	21
	B. System Design	21
	C. System Implementation	24
	D. Electronic Processing System	31
	E. Outputs and Controls	39
	F. Signal-to-Noise Calculations	41
	G. System Tests	46
III	PRIMS EXPERIMENTAL DESIGN TEST PROGRAM	55
	A. Introduction	55
	B. Chopped Argon Laser Experiment	57
	C. Pulsed Ruby Laser Experiment	64
	D. Acousto-optic Modulator Development	68
	E. Synchronization of Acoustic Pulse with Laser Pulse	68
	F. Beam Alignment Techniques	69
	G. Optical Power Handling Capabilities	70
	H. Experimental Results	70
	I. Comparative Testing of RCA C31024A Photomultiplier	78
	J. Fiber Optic Delay Line Development	79

SECTION	PAGE
K. Signal Processing Study	88
L. Summary and Conclusions	93
IV AMOS LASER MODIFICATIONS	95
A. Experimental Approach	95
B. Experimental Tools	95
C. Experimental Setup	95
D. Experimental Results	97
E. Operating Parameters in Need of Optimization . .	104
V PRIM COMPUTER SIMULATION	106
A. Introduction	106
B. Computer Simulation Scheme	106
C. PRIMS Reconstructed Images	111
D. Conclusions	128
VI PUBLICATIONS AND PRESENTATIONS	129
APPENDICES	
A SEEING MONITOR INDICATORS, OUTPUTS, AND CONTROLS . . .	131
B SEEING MONITOR - DIGITAL OPERATION	137
C SEEING MONITOR SIGNAL-TO-NOISE CALCULATIONS	143
D SEEING MONITOR CALIBRATION PROCEDURES AND SUPPORT DATA	155
E NOISE-EQUIVALENT QUANTUM EFFICIENCY MEASUREMENTS . . .	177
F ALIGNMENT TECHNIQUE FOR PRIMS TRANSMITTER	185
G PULSE TESTING OF RCA C31094A PHOTOMULTIPLIER	189
H OPTIONAL FIBER PROPAGATION LOSS EXPERIMENTS	197
I CLADDING REMOVAL FROM OPTICAL FIBERS	203

LIST OF ILLUSTRATIONS

Figure		Page
1	PRIMS format with two frequency-two polarization transmitter and two-frequency single polarization receiver	13
2	Block diagram of the Seeing Monitor system	25
3	Views of the Seeing Monitor electronics and optomechanical package	26
4	Block diagram of the electronic processing system	33
5	Block diagram of one of the processing channels showing details of MTF and seeing angle processing	34
6	Block diagram of wander detector	37
7	Wander detector processing	38
8	View of control electronics front panel	40
9	Relative response for photopic vision	44
10	Spectral response of EMI extended red S20 photocathode (9658R)	45
11	Seeing angle standard deviation versus stellar magnitude	47
12	Chopped argon experiment	59
13	PRIMS phase detector system	59
14	Video and rf signals in chopped argon experiment	61
15	Phase detector output signals in chopped argon experiment	62
16	Pulsed ruby experiment apparatus	65
17	Block diagram of pulsed ruby experiment	66
18	Medium power photomixing of 30 nsec pulses	71
19	Photomixing and in phase and quadrature phase detection	73

Figure		Page
20	Unfiltered phase detector output and error signals due to pulse spectrum	75
21	Preliminary low level measurements	77
22	Ten element fiber optic delay line system with mode suppression on input and output	80
23	Details of cladding mode suppressor	81
24	Anomalous pulse attenuation due to cladding mode propagation	83
25	Pulse amplitude versus delay time without cladding mode suppression	84
26	Fiber optic response to multimode laser pulse	86
27	Pulse amplitude versus delay time with partial cladding mode suppression	87
28	Interpulse delay data	89
29	Interpulse delay data	90
30	PRIMS digital data recorder	91
31	AMOS ruby laser experimental setup	96
32	AMOS oscillator performance prior to modification	98
33	Modified oscillator performance	100
34	Oscillator performance at 20 ppm	101
35	Multimode pulses through amplifiers	102
36	Single mode pulses through amplifiers	103
37	PRIM computer simulation block diagram	107
38	Pictorial summary of PRIM system performance capability	112
39	PRIM system performance as a function of speckle averaging	114
40	PRIM system performance as a function of signal-to- noise ratio	116

Figure		Page
41	PRIM system performance as a function of glint amplitude	118
42	PRIM system performance as a function of glint distribution	120
43	PRIM system performance as a function of receiver signal digitization	122
44	PRIM system performance as a function of receiver averaging	124
45	Auto-correlation function of object, with and without glint	126

I. INTRODUCTION

A. Background

There are two general objectives to the current Space Object Imaging (SOI) program. The first is to build a Seeing Monitor to measure the statistics of atmospheric seeing at the AMOS observatory. The second is to investigate by experiment and by computer simulation the feasibility of performing a demonstration of a Polarization Reference Imaging System (PRIMS) at AMOS employing the existing AMOS ruby laser.

The current Space Object Imaging contract is a continuation of work done under DARPA/MICOM Contract DAAH01-73-C-0629. The AMOS seeing monitor is based on a spinning reticle photometer employed under the previous contract for searching for brief periods of nearly undegraded atmospheric seeing. These experiments are described in the final technical report of the DARPA/MICOM contract entitled Space Object Imaging Techniques, June 1974 (Ref. 1). The above report can also be referred to for a more complete discussion of the PRIMS concepts. However, a brief review of the PRIMS concept and the conclusions of the previous work will be given here for completeness.

1. PRIMS Concept

PRIMS is an active advanced SOI concept, developed by Hughes, which eliminates atmospheric distortion in imaging space objects. A true image is obtained by utilizing a strong glint originating from the object as a point reference source to provide the proper phasing information for the receiver array. A PRIMS receiver samples the reflected reference and object fields in the aperture plane and, usually by employing heterodyne receivers and coherent phase detection, generates in phase (I) and quadrature (Q) signals that yield the amplitude and phase of the object field. A Fourier transform, e. g.,

with a digital computer, then produces a true image of the object. PRIMS operates in either the visible or infrared and does not require interferometrically stable receiver arrays.

The reference source and object field are "tagged" by orthogonal polarizations so that many variations are possible for implementing the PRIMS concept. These differ mainly in the transmitting and receiving formats employed. Two basic formats are (1) two-frequency and dual polarization transmitter with two-frequency and single-polarization receiver (see Fig. 1), and (2) one-frequency and single-polarization transmitter, with two-frequency and dual-polarization receivers. Linear array scanning systems, attractive for large baseline applications, have also been described.¹ The advantage of any particular system over others depends on such factors as type of receivers desired, dynamic range of the reflected object field, etc.

The PRIMS concept, when applied to synchronous orbits, has the potential of achieving true image resolutions unmatched by other systems proposed to date. Operating at $10.6 \mu\text{m}$, the system has the potential of achieving angular resolution of 0.0015 arc-sec . A comparison of the relevant parameters for low orbit and synchronous orbit operation is shown in Table 1.

Table 1. Comparison of Low Orbit and Synchronous Orbit Operation

Range, km	Object Size, m	Wave- length, μm	Angular Resolution, arc-sec	Resolution Size, cm	Array Baseline	Maximum Receiver Size
40,000	10	10.6	0.0015	30	1.4 km	47 m
400	4	10.6	0.15	30	14 m	1.1 m
400	4	0.69	0.15	30	1 m	7.5 cm

T1799

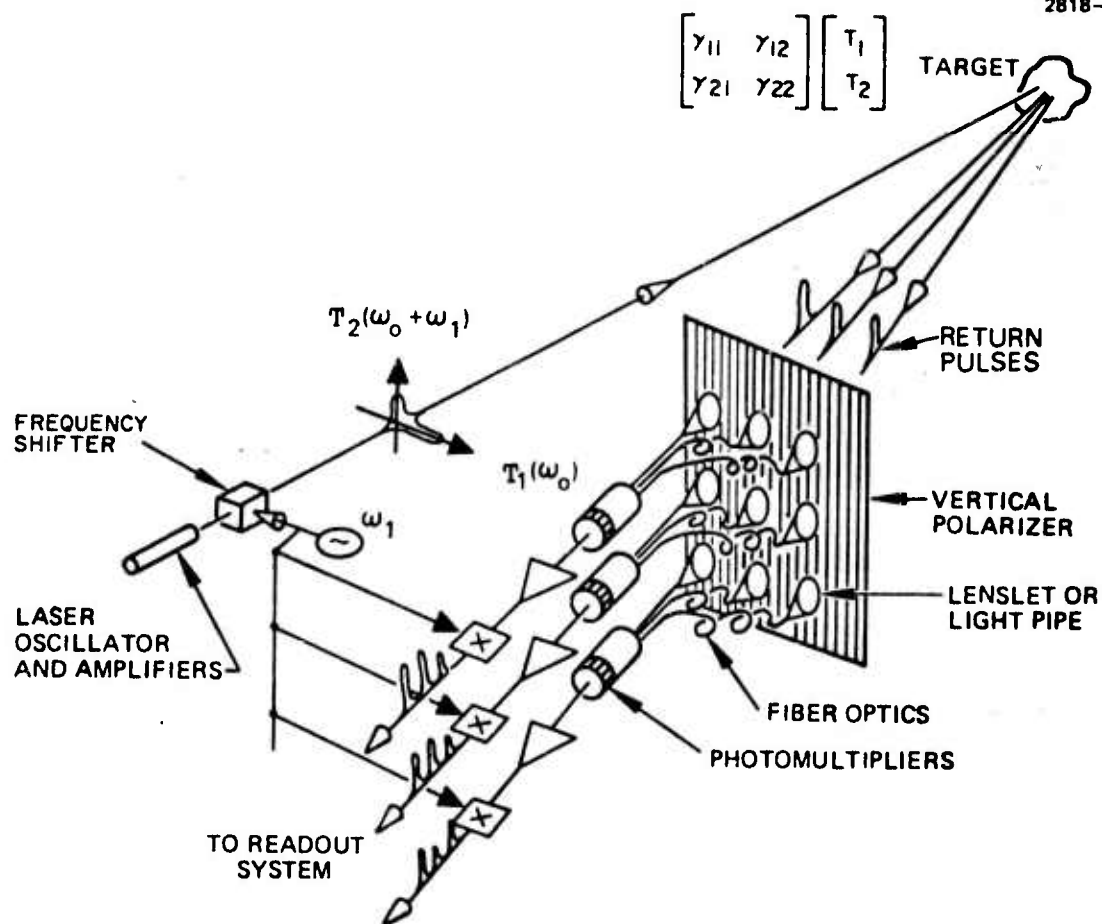


Figure 1. PRIMS Format with two frequency-two polarization transmitter and two-frequency single polarization receiver.

2. Summary of Conclusions from Previous PRIMS Studies

The PRIMS studies conducted under the DARPA/MICOM contract can be briefly summarized as follows:

- A table-top PRIMS experiment demonstrated the feasibility of the concept and, in particular, that atmospheric phase terms cancel in a PRIMS receiver.
- Preliminary measurements of cross-polarized returns from laboratory scale objects showed glint structures and depolarization adequate for PRIMS operation at both visible and 10 μm wavelengths.
- Straightforward techniques were defined for handling target situations in which several glints are present simultaneously.
- Transmitter scanning thinned-array concepts were investigated that will allow implementation of 10.6 μm high orbit PRIMS systems at manageable cost levels.
- PRIMS has two advantages over correlography systems: PRIMS produces a true image rather than a correlogram and PRIMS requires considerably fewer pulses to achieve satisfactory imagery.
- PRIMS is insensitive to errors in receiver positioning, local oscillator frequencies need not be exactly the same at each receiver and local oscillator phase cancels exactly at each receiver.

B. Summary of Report

This report consists of two major parts. The first part deals with the Hughes Seeing Monitor. This instrument, which was designed, built, and delivered on the present contract, samples star images on a millisecond time scale and processes the information obtained from these samples to yield information on atmospheric seeing conditions.

Section II describes the optical and electronic design of the Seeing Monitor and the manner in which the design has been implemented to yield modulation transfer function (MTF), seeing angle, and image wander information for star images that are simultaneously scanned in orthogonal directions with a spinning reticle wheel. The reticle wheel which has a chopping pattern that changes exponentially with angle transforms spatial frequencies into temporal frequencies in the light transmitted through the wheel. This light is detected by photomultipliers and processed to yield the output data. The instrument employs an image rotator that allows the directions of maximum asymmetry in star images to be selected and measured. The optical and electronic design details of the Seeing Monitor are followed by a signal-to-noise analysis that predicts the sensitivity of the instrument for stars of different magnitudes. Finally, the results of laboratory tests and calibrations, and tests that were taken at AMOS on the B = 30 48 in. telescope are described, and a comparison of the measured performance with the predicted performance is made.

All of the performance goals that were set for the Seeing Monitor have been achieved in the delivered instrument. The dynamic range of seeing angle that was set for the Seeing Monitor is 0.1 to 10 arc-sec; the measured dynamic range for the B = 30 48 in. telescope is 0.14 to 10 arc-sec. This falls short of the desired performance at the low end, but for the longer focal length 60 in. telescope (960 in. versus 741 in. for the B = 30) for which the Seeing Monitor was originally designed the lower end of the dynamic range will be 0.10 arc-sec. Based on a semiquantitative evaluation of the performance during the final acceptance tests at AMOS the Seeing Monitor was found to perform acceptably for stars of visual magnitude 6.7. For the larger aperture 60 in. telescope comparable performance is expected for stars of visual magnitude in excess of 7.

The second part of this report deals with establishing the feasibility of PRIMS directed toward a demonstration experiment using the

AMOS ruby laser as an illumination source. All of the results obtained on this program lead to the conclusion that a PRIMS demonstration experiment is feasible. Section III describes a series of laboratory experiments in which the basic PRIMS transmitter scheme was demonstrated. In these experiments the light from a pulsed laser source (both argon ion and Q-switched ruby lasers) was split into two beams having orthogonal polarizations, one of which was frequency shifted by means of a pulsed 150 MHz acousto-optic modulator and then recombined with the other into a single beam. Feasibility of the PRIMS receiver was demonstrated in a series of experiments in which heterodyne detection and phase synchronous detection of the 30 nsec pulses generated by the PRIMS transmitter was accomplished. Another feature of the PRIMS receiver — time division multiplexing — was demonstrated by the successful testing of a ten-element fiber optic delay line and a number of issues such as fiber cleaving, etching, and cladding removal were addressed.

Section IV describes a series of measurements and modifications that were performed on the AMOS ruby laser system aimed at demonstrating its feasibility as a PRIMS transmitter. The essential modification that is critical to PRIMS was the operation of the AMOS laser Q-switched in a single longitudinal mode. Evidence is presented showing that the system was made to yield pulses from 20 to 30 nsec in duration that were temporally coherent throughout the duration of the pulse. Moreover, this behavior was demonstrated not only for single pulse operation but also when the laser system was repetitively pulsed at 20 ppm.

Finally, Section V contains the results of PRIMS computer simulations in which a number of key issues were addressed and answered. These studies were undertaken to determine the characteristics of the PRIM concept relative to pertinent system parameters such as speckle averaging, signal to noise, and digitizing schemes. For these studies computer-generated PRIMS images were obtained under a variety of conditions and compared with both diffraction limited

images and images simulated through atmospheric turbulence. From the computer simulation studies it is concluded that near diffraction limited image quality can be obtained from a PRIMS system under the following conditions:

- Five or more overlays for speckle averaging
- Signal to noise of three or greater
- Glint amplitude of 125 or greater
- Glint amplitude differential of 2 to 1 or greater in multiglint situations
- Digitizing to 2 bits or more.

C. Recommendations for Future Work

Based on the results obtained on the present program it remains to demonstrate the PRIMS principle by obtaining diffraction-limited images of distant targets through a turbulent atmosphere. Details of a visible PRIMS demonstration experiment are presented in Hughes Technical Proposal 75M-0533/D5855, June 1975; a summary of our recommendations is given below.

For the visible PRIMS demonstration experiment, we propose to employ the AMOS ruby laser as a transmitter and 1.5 m telescope as a receiver to obtain an image of a cooperative stationary target located at the AMOS West Maui site, a distance of approximately 40 km from the AMOS Observatory site. The choice of a stationary target instead of an orbiting satellite for a PRIMS demonstration experiment is dictated primarily by the relocation of the AMOS ruby laser system into the small beam director (SBD) facility. A linearly polarized beam from the laser on passing through the coelostat mirror arrangement of the SBD will, in general, be rotated to a different plane of polarization. If a metal mirror is used at the last stage of the coelostat, the linearly polarized input will in general become elliptically polarized, a situation that is intolerable for PRIMS. The use of the SBD for PRIMS

experiments on orbiting satellites requires a real time polarization compensation scheme for both transmitter and receiver that would employ polarizers and half-wave plates whose angular position would be chosen so as to preserve the linear polarization purity of the two collinear transmitted beams. While the implementation of this polarization compensation scheme would involve straightforward electromechanical techniques, the additional cost and complexity is not warranted for the purpose of an initial PRIMS demonstration.

The choice of a stationary cooperative target for PRIMS offers additional advantages over that of an orbiting satellite. First, the support requirements for gathering data are substantially less for this kind of experiment than for one in which a satellite is the target. Data can be taken in a more leisurely manner and at times that are convenient and compatible with other AMOS missions. System performance can be easily measured under a variety of atmospheric conditions. The properties of the target can be chosen and important parameters can be varied (relative glint strength, surface depolarized reflectivity, multiple glint structure, etc.) simply and inexpensively. Finally, speckle averaging which is implemented by providing multiple shot image overlays (10 to 50) can be easily accomplished using a stationary target and the AMOS laser at its 20 ppm repetition rate. The target must remain essentially fixed in its aspect relative to the receiver during the speckle averaging process and for this reason the desired number of exposures can be obtained on orbiting satellites only under special conditions using the AMOS laser at its present repetition rate capability. (Schemes for upgrading the AMOS laser to a short term high repetition rate Q-switched capability have been discussed in a Hughes Research Laboratories informal proposal to DARPA.)

Implementation of the PRIMS demonstration experiment summarized as follows:

The AMOS ruby laser will be employed as the target illuminator. It will be modified to operate Q-switched in a single longitudinal

mode with a pulse duration of 20 to 30 nsec. Appropriate polarizers, wave plates, and an acousto-optic modulator will be incorporated in the laser setup so that the output beam consists of two orthogonally polarized components, one component shifted in frequency relative to the other by approximately 150 MHz. The PRIMS transmitter modifications will be sufficiently flexible so that the laser can be returned to its original condition simply and quickly.

A PRIMS receiver will be built consisting of relay optics, optical fibers, photomultipliers, and processing electronics. The receiver will use the AMOS 1.5 m telescope to collect the light, and recollimating optics will be employed to relay the 1.5 m aperture onto a 100 element array of optical fibers. Light from the array will be time division multiplexed onto ten fast photomultipliers. Processing electronics will be built consisting of ten polar phase detectors followed by fast analog-to-digital converters and tape recorder output. The image will be recovered from the data by performing an inverse Fourier transform on the complex array of samples using a digital computer.

In summary, the proposed experiment is designed to verify the feasibility of the PRIMS concept via an experimental demonstration under controlled transmitter, receiver, and target conditions. Because the proposed demonstration experiment employs a ground-based target the AMOS support requirements are substantially less than those needed to man operations that involve orbiting satellites, and as such represents a less costly means of performing a demonstration experiment than one requiring support of a full operations crew at AMOS.

II. SEEING MONITOR

A. Introduction

The Seeing Monitor is a spinning reticle photometer that will measure atmospheric seeing conditions on the AMOS B = 30 telescope. It samples star image widths to provide data that can be processed to yield the mean and variance of the seeing angle, the time autocorrelation function of the seeing angle, and the modulation transfer function (MTF) of the atmosphere and telescope. The star image widths are sampled in orthogonal directions that can be selected with an image rotator to match one of the MTF directions with the direction of maximum spatial frequency response of the atmosphere. The seeing angle and MTF data cover the range from 0.1 to 10 arc-sec and the sample time is 10^{-3} sec to ensure that the individual samples do not time-average the star image widths.

The reticle wheel transforms spatial frequencies of the image into temporal frequencies in the light transmitted through the wheel. This light is detected by photomultipliers and processed to yield the MTF and other data.

In the next section the various features of the Seeing Monitor are described. The following sections then discuss the way in which these features are implemented, presenting the designs of the optical and electronic systems. Finally a signal-to-noise analysis is presented and the results of laboratory and telescope tests are given.

B. System Design

1. The MTF

The Modulation Transfer Function (MTF) provided by the Seeing Monitor is the amplitude of the Fourier transform of a mathematical projection of the star image on an axis. The independent variable for the MTF is spatial frequency k , which has units of the reciprocal of a displacement in space. Representing the projection of the star image (on the x -axis) as $I(x)$, the corresponding MTF is

$$\text{MTF}(k) = \text{MTF}(0) \exp [-(2\pi k)^2 \sigma^2 / 2] . \quad (2)$$

Then $k_{1/2}$ is such that $\text{MTF}(k_{1/2}) = 1/2 \text{MTF}(0)$. Hence $(2\pi k_{1/2})^2 \sigma^2 / 2 = \ln 2$ giving

$$k_{1/2} = \sqrt{2 \ln 2} / \pi \theta^s = 0.37 / \theta^s . \quad (3)$$

Each of the two seeing angles θ_x^s and θ_y^s is output once per millisecond as a serial digital signal. These signals are suitable for recording on two channels of a tape recorder with digital record capability. An analog output of θ^s is also provided for monitoring on an oscilloscope.

3. Image Wander

As an auxiliary function, the Seeing Monitor also measures and outputs the instantaneous position of the star image. This output is called wander; it is provided as an analog signal for oscilloscopic monitoring. The bandwidth for this wander determination is 200 Hz. The 200 Hz bandwidth is deliberately made smaller than the bandwidth associated with the 1 kHz sampling rate in order to provide a higher signal-to-noise ratio for the wander signal. It has been found by previous experiments that the image position moves slowly compared with the fluctuations in image quality; in fact, we observed during initial testing at AMOS that image motions do not have significant frequency components above 50 Hz.

The wander signals from the x- and y-channels are also digitized and multiplexed onto a single third digital channel (the first two digital channels are those for θ_x^s and θ_y^s). The sampling rate for the digital wander signal is 250 times per second.

4. Rotation and Magnification Information

Digital representations of the position of the image rotator and the position of the range (magnification) selector are also multiplexed onto the third digital channel to provide documentation of their settings. The rotator setting is represented by a 6-bit gray-coded number and the range is indicated by a two-bit binary number from 1 to 3.

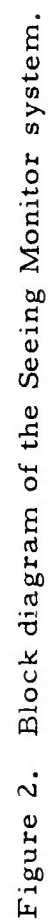
C. System Implementation

1. Optical System Introduction

Figure 2 gives a block diagram of the Seeing Monitor system. Figure 3 shows photographs of the control electronics box and views of the on-board optics and electronics package. The image at the telescope prime focus is reimaged on a spinning reticle wheel. The wheel is composed of twelve sectors, each of which has an identical chopping pattern of alternate clear and opaque bars; the size of the bars and their spacing decreases exponentially over the sector. Use of an exponential decrease allows a 32 to 1 frequency range to be covered in such a way that the signal-to-noise ratio for the Seeing Monitor outputs is the same for all conditions of seeing; i.e., the seeing angle is determined to the same relative accuracy for all seeing conditions. The wheel spins at 5000 rpm, so each sector takes 1 msec to traverse the star image. By the use of a beamsplitter, two star images are actually formed on the wheel at places 90° apart, thus allowing simultaneous orthogonal scans of the star image. These correspond to the two channels of MTF processing. A photomultiplier behind the wheel at the position of each of the two images measures the instantaneous transmitted light in each channel. The MTFs of the star image are obtained by electronically processing the photomultiplier outputs.

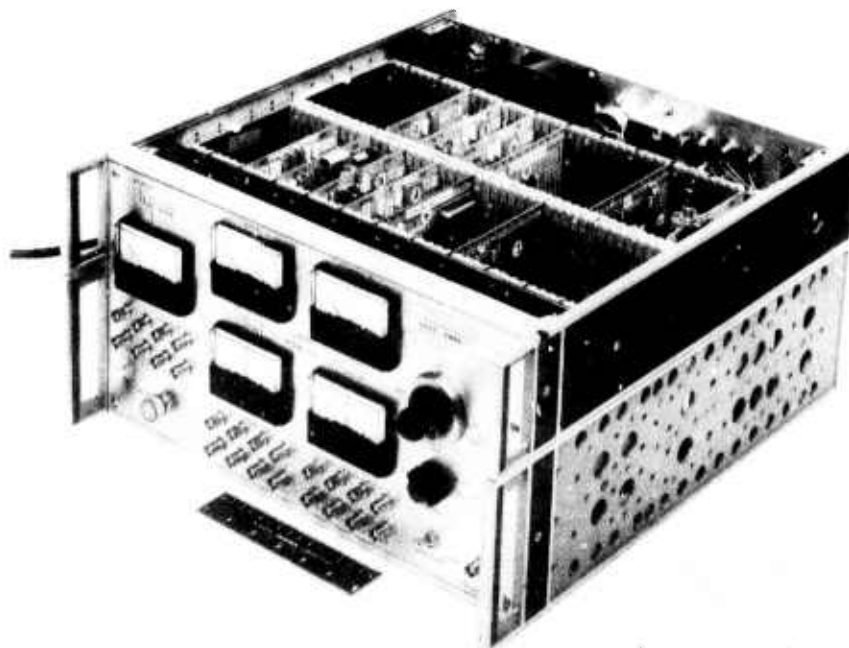
2. General Considerations

The optics include six lenses, six mirrors, a dove prism, and a cemented-cube beamsplitter. To maintain maximum light throughput, the lenses, dove prism, and beamsplitter are antireflection coated and the mirror surfaces have a high-reflectivity metallic coating. For ease of mounting, the mirrors are right isosceles prisms using external reflection from the hypotenuse. The mirrors were specified to have one-quarter wave flatness over 80% of their surfaces. The beamsplitter and dove prism were specified for diffraction-limited optical quality, and, using a Twyman-Green interferometer, their wavefront distortion has been measured at less than one-eighth wavelength over their entire surfaces. The lenses are cemented doublets; interferometric tests have verified that all the lenses except L_2 and L_3 are diffraction limited for the f-cones and fields of view of the Seeing Monitor optics. See Appendix D for further elaboration on lens performance.



M10579

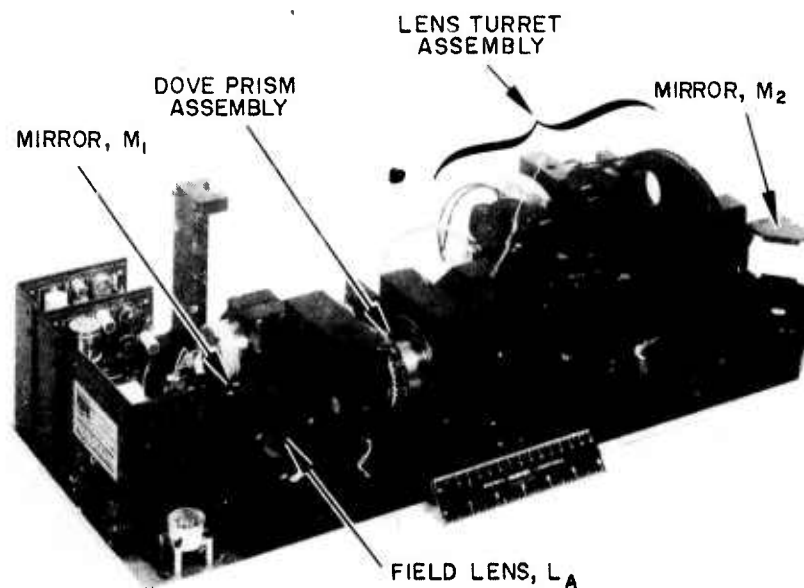
4708-37



CONTROL ELECTRONICS BOX

M10582

4708-38



ONBOARD OPTICS ASSEMBLY

Figure 3. Views of the Seeing Monitor Electronics and optomechanical package.

M10581

4708-39

ONBOARD ELECTRONICS
CHANNEL 1 CHANNEL 2

RETICLE WHEEL

BEAM
SPLITTER
CUBE

FOLDING
MIRROR

PHOTOMULTIPLIER
HOUSING,
CHANNEL 1

RETICLE WHEEL BOX, COVER REMOVED

M10580

4708-40

LIGHT
FROM
MIRROR
M₂
ENTERS
HERE

RETICLE WHEEL BOX, ASSEMBLED

Figure 3. Continued.

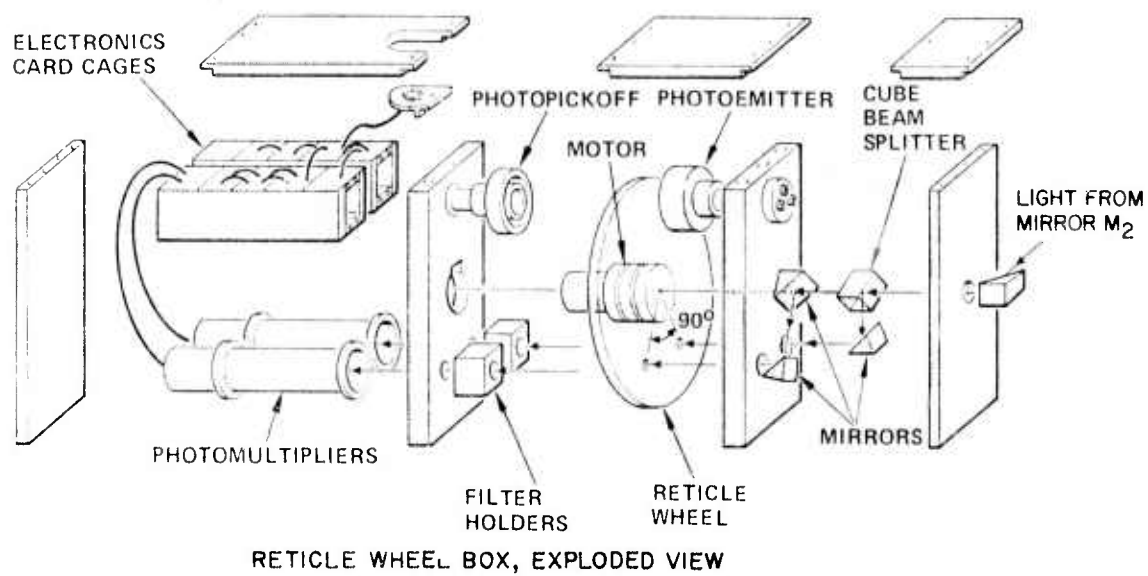


Figure 3. Continued.

3. Magnification Selection

The image at prime focus P_1 is reimaged at intermediate focal plane P_2 . This image is then relayed to the focal plane at the reticle wheel by one of three lenses on a turret. These three lenses provide the three magnifications required for the range selection feature. The magnifications for the three settings are given in Table 2 along with the effective focal length f_{eff} which is obtained by multiplying the Seeing Monitor magnification by the telescope focal length (741 in. was chosen as the $B = 30$ telescope focal length).

The turret is activated by a motor-clutch combination; a detent-cam follower arrangement provides alignment repeatable at each of the three settings. To eliminate drift of field of view and of focus, the cam and turret assemblies are designed for high precision and minimum compliance. The resulting repeatability of the field of view was found during our initial AMOS tests to be better than 1 arc-sec in each case.

4. Image Rotation

Between image planes P_1 and P_2 the light is collimated and passed through an 0.6 in. x 0.6 in. x 3.0 in. dove prism. The dove prism is mounted on bearings so that it may be rotated about its long axis. Rotation of the dove prism by a synchro system then provides the required image rotation. The synchro system consists of a nonamplified 60 Hz synchro transmitter and receiver pair.

Table 2. Seeing Monitor Magnification for Different Turret Settings

Turret Setting	Magnification	$f_{\text{eff}} = M \times 741 \text{ in.}$
0.1 to 2 arc sec	3.67	2720
0.3 to 6	1.39	1030
0.5 to 10	0.745	552

The placement of the dove prism in a collimated region of the beam eliminates the effect of the prism's dispersion or the focal length of the system. Lens L_A is a Huygens-type field lens that causes the telescope objective to be imaged at the center of the dove prism. This condition provides for minimum vignetting (in fact, no vignetting over our field of view). Lens L_B collimates the light from the image, and lens L_C refocuses the collimated light onto image plane P_2 .

5. The Beamsplitter

The beamsplitter is a 1-in. cemented cube of BK-7 glass with a dielectric diagonal layer that reflects $50\% \pm 8\%$ of red light at 45° . The dielectric reflecting medium was chosen because of its low absorption compared to that of a metallized layer.

6. Optical Alignment

The optical system is prealigned in the laboratory to ensure that (1) all lenses are centered on the optical axis, (2) the lens are parallel with the optical axis, (3) the path lengths are equalized following the beamsplitter, (4) the dove-prism axis of rotation is aligned with the optical axis, and (5) the dove prism's optical axis is parallel with the axis of rotation.

Using a laboratory simulation of the telescope's prime-focus image at P_1 , the position of lens L_A is adjusted to obtain collimated light at the dove prism, and the position of lenses L_1 , L_2 , and L_3 is then adjusted for best focus (as determined by monitoring photomultiplier tube output).

Trimming screws are provided on mirror M_1 to adjust the position of the field of view after the seeing monitor is mounted on the telescope. An adjustment is provided on lens L_A to compensate for the residual difference between the assumed prime focal plane and the actual one when the Seeing Monitor is on the telescope.

7. Reticle Wheel

The reticle wheel is 6 in. in diameter and rotates at 5000 rpm. The diameter was chosen as the largest that would conveniently fit in the Seeing Monitor package. The 5000 rpm was then chosen as the highest speed at which the glass wheel could operate without danger of fracture. Each sector of the wheel subtends 30° ($\pi/6$ rad). In order to obtain brightness

and wander information, the region 0 to 6° is divided into one wide opaque zone and one wide clear zone. The arrangement of these two wide zones allows the light received during the first 0.200 msec (while this region is under the image) to be used for determining the brightness of the image and its position in the Seeing Monitor's field of view. Light gathered during the remaining 0.800 msec period (while the region 6 to 30° is under the image) is used for determining the MTF of the image. Over this 6 to 30° region the reticle wheel's chopping frequency increases exponentially with angle, covering approximately a 32-to-1 frequency range of 11 to 350 Hz.

The optical transmission of the wheel as a function of angular position θ is

$$W(\theta) = S[\phi_0 \exp(\theta/\theta_0)] \quad 0 \leq \theta \leq \pi/6$$

$S(\phi)$ is a square wave function defined as

$$S(\phi) = \begin{cases} 0 & \text{if } \sin \phi \geq 0 \\ 1 & \text{if } \sin \phi < 0 \end{cases}$$

The values of θ_0 and ϕ_0 for the chopping pattern are 0.1150 rad and 5.022 rad, respectively. While $\theta = 0$ is defined as the beginning of the dark sector of the first zone of the reticle wheel chopping pattern the above equation is valid only from the beginning of the second zone. See Appendix D, Table D-1 for a detailed tabulation of the reticle wheel pattern.

D. Electronic Processing System

1. Introduction

The effect of the reticle wheel is to convert spatial frequencies of the image into temporal frequencies in the total light flux transmitted through the wheel. The electronic processing system for each channel puts out a voltage proportional to the magnitude of the Fourier component of the

photomultiplier output at the instantaneous chopping frequency (magnitude meaning the square root of the sum of the squares of the sine and cosine components). This voltage is then proportional to the MTF at the spatial frequency corresponding to that temporal frequency; it is the MTF output signal mentioned earlier.

Figure 4 is a block diagram of the electronic processing system. The system consists of a section for motor-speed control and the two identical channels for processing the outputs of the two photomultipliers.

2. Speed Control

The reticle wheel is driven by a dc motor, and the voltage is controlled by a servo system. The servo system determines the speed of the wheel by measuring the time between the beginnings of successive sectors of the reticle wheel. A photoelectric pickoff operating in near infrared (9000 \AA) generates a pulse when it detects a clear stripe on an auxiliary track on the wheel at the beginning of each sector. The time between successive pulses is clocked using the 2.048 MHz crystal oscillator and a binary counter and latch. The speed error thus detected is fed back to the motor voltage to close the loop. (The sum of the direct error and its integral is fed back to eliminate velocity handoff.)

3. Modulation Transfer Function and Seeing Angle

Figure 5 gives a detailed block diagram of one of the two processing channels. Each of these channels processes its photomultiplier output to obtain MTF, seeing angle, and wander information. The photomultiplier signal drives an in-phase and a quadrature synchronous demodulator. That is, in one demodulator the photomultiplier signal is multiplied by a sine wave corresponding to fundamental of the instantaneous square-wave chopping pattern and in the other demodulator, it is multiplied by a cosine wave, which is the above sine wave shifted 90° . These sine and cosine waves, which track the increasing frequency of the chopping pattern, are generated from patterns stored in read-only memories. The read-only memories are digital devices that have permanently stored within them 2048 words. The words are read out one at a time by applying successive (11-bit) addresses to the address terminals. The words themselves consist of four bits, representing a four-digit binary number. The binary number indicates the

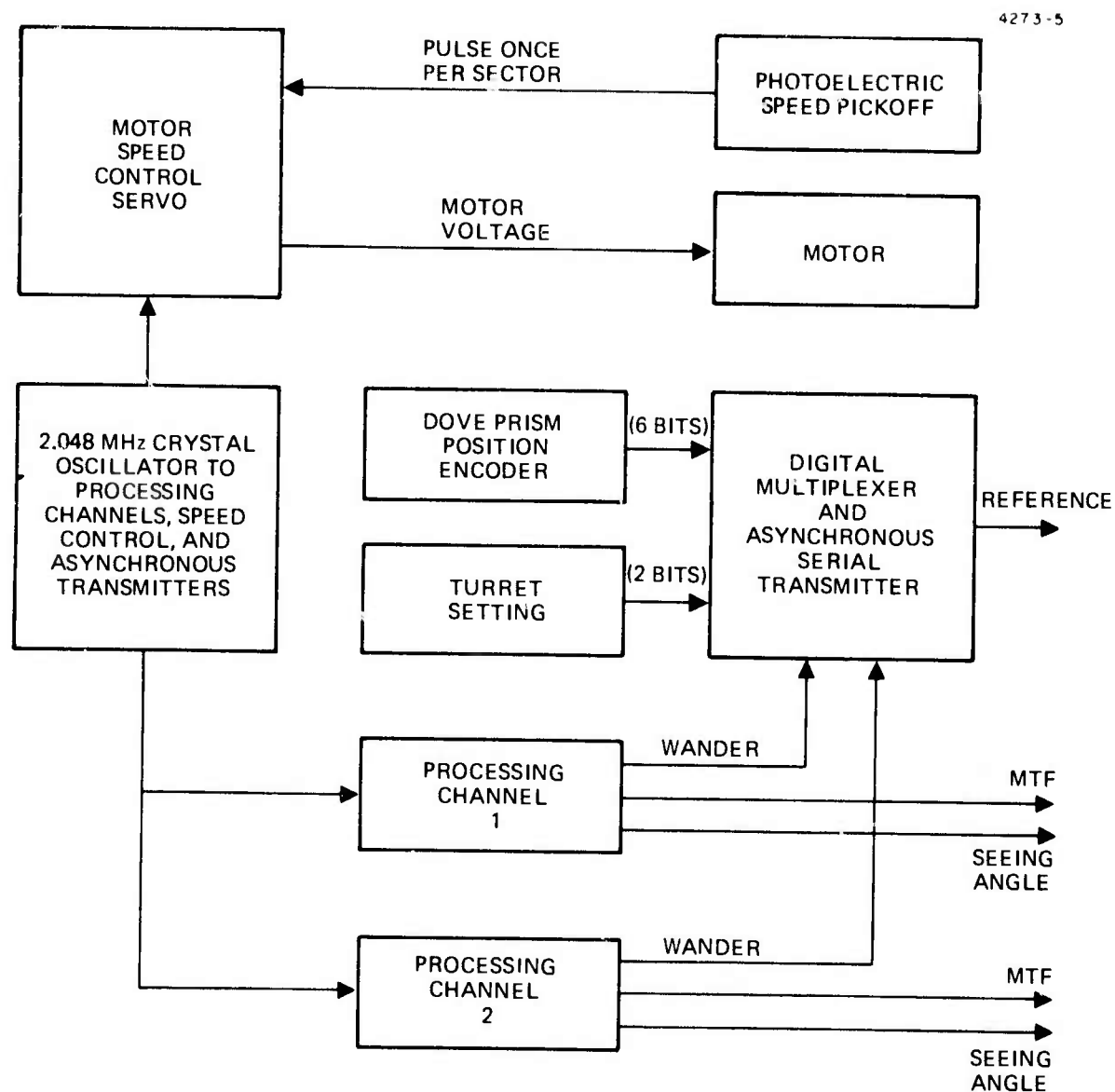
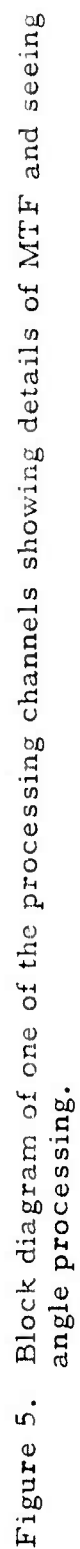


Figure 4. Block diagram of the electronic processing system.



instantaneous value of the sine or cosine. The four bits are converted to an analog voltage by using four parallel gated current sources weighted by 1, 2, 4 and 8 (this is the standard digital to analog conversion technique).

The demodulators are high-speed analog multipliers followed by low-pass filters. The Root-Sum-Square is taken of the two demodulator outputs to give the MTF for the spatial frequency corresponding to the instantaneous chopping frequency.

4. Light-Level Control

The Seeing Monitor has two subsystems that enable it to adapt to changes in the light level of the star image: a gain control for the photomultipliers to provide constant average anode current over many orders of magnitude of light levels, and a brightness detector in the processing electronics that detects residual brightness fluctuations. The gain control adjusts the photomultiplier cathode and dynode chain voltage to maintain 0.9 mA average anode current, and includes a rapid shutdown circuit to protect the photomultipliers from sudden large increases in light level. The characteristic response time of the gain control is 100 msec. The brightness detector forms the difference of the photomultiplier signals from the wide light and dark areas of the reticle wheel to give the overall signal level. This level is in fact $MTF(0)$, the zero-spatial-frequency MTF value. The response of the brightness detector is selected to be 10 msec to provide fast response but good immunity to quantum noise. This $MTF(0)$ signal is divided by two and used as the threshold for determining seeing angle (i.e. the point k where $MTF(k) = 1/2 MTF(0)$).

5. Operation of the Wander Detector

It is necessary for the processing channel to know the position of the star image in the field of view so that it can generate demodulating sine and cosine waves corresponding to the chopping frequency at the exact position of the image. Referring to Fig. 5, the wander detector provides an indication of the position of the star image by generating a sync pulse when the no-light-to-light transition occurs at the beginning of the sector (this transition occurs when the boundary between the wide dark and light zones is at the position of the image).

To minimize the effect of quantum noise on the sync pulse timing, the wander detector averages information obtained over about five 1-msec periods. The demodulating sine and cosine waves are synchronized to this transition time by using the wander detector's sync pulse to initialize the counter that generates the read-only memory address. The wander information is also provided as an output in both analog and digital form.

Figures 6 and 7 illustrate the operation of the wander detector. The wander detector generates a voltage VW proportional to its estimate of the current position of the image. A START pulse is generated W μ sec after the photopickoff pulse (REF) where the time W is proportional to the voltage VW. (This conversion of voltage to time-delay is done using a linear ramp initiated by REF and a comparator.) The wander detector's output is the START pulse; it is used to synchronize the read-only-memory sine and cosine generators.

The voltage VW is held on an integrator. For each sector, an update is made to voltage VW in order to servo VW to follow the motion of the image. This update is done by injecting currents proportional to the photomultiplier signal or its inverse over three time intervals. It is equivalent to adding to VW the voltage increment E_u : $VW_{\text{new}} = VW_{\text{old}} + E_u$ where $E_u = K(I_{EA+EC}/2 - I_{EB})$. I_{EB} is defined as the integral of the photomultiplier output over the time interval EB and I_{EA+EC} is the integral of the photomultiplier output during the time intervals EA and EC. The time interval EA is initiated a fixed time t_1 after the START pulse is generated. EB follows and then EC. EA, EB, and EC are each 62.5 μ m long.

Figure 7 illustrates the case where the photomultiplier signal due to the initial 100 μ sec-wide dark and light zones is centered on the combined interval $EA \cup EB \cup EC$. For the case illustrated, the dark-to-light transition t_{DL} occurs at the middle of interval EB, and the correction voltage E_u is zero (within errors due to quantum noise). In this illustrated case, the Seeing Monitor's estimate of image position is correct.

If the image moves clockwise tangentially, the photomultiplier output SGP will appear later in time, i.e., shift to the right in Fig. 7. For as long as this condition exists, the correction voltage E_u will be positive, causing VW to increase; W will therefore increase and START will occur later in time (with respect to the photopickoff pulse, which gives absolute wheel

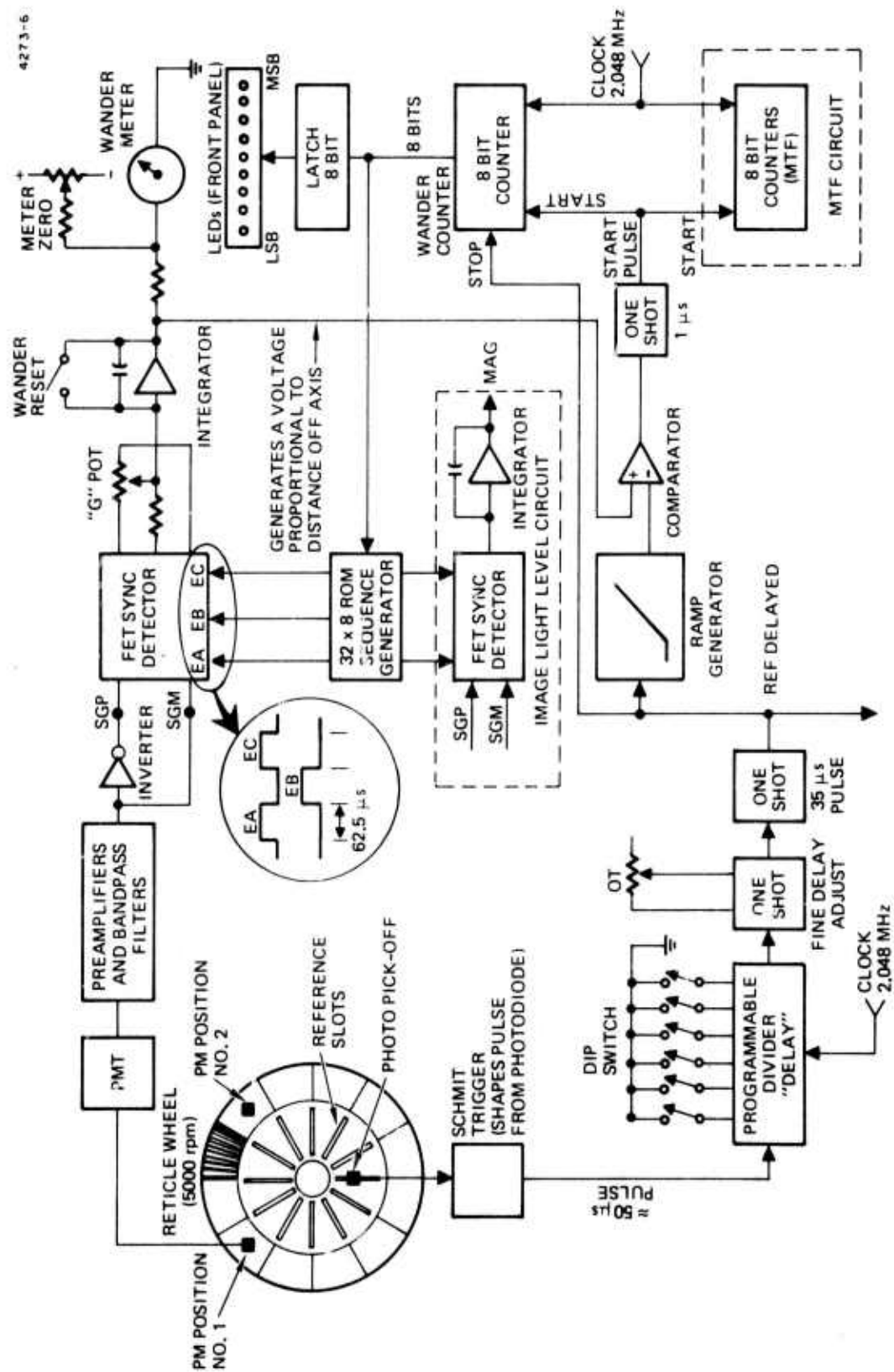


Figure 6. Block diagram of wander detector.

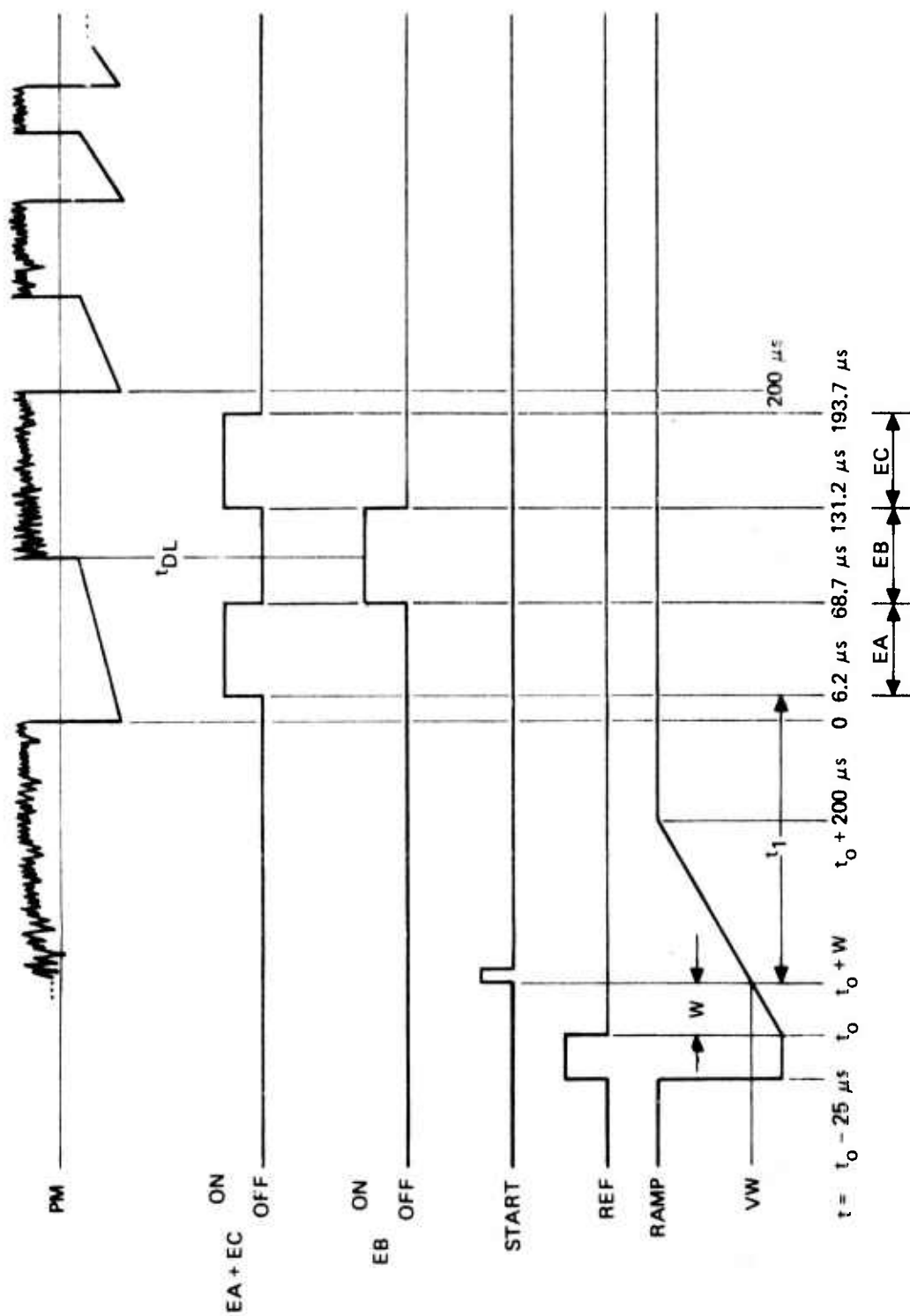


Figure 7. Wander detector processing.

position). The intervals EA, EB, and EC occur a fixed time after START, so these will occur later in time. This correction will occur until t_{DL} again bisects EB. Thus START is servoed to occur at a fixed time before the image-position-defined transition t_{DL} . (This time is in fact $t_1 + 93.75 \mu\text{sec.}$)

The resistance R and capacitance C are chosen to provide a 5 msec time constant for the servo system. Since the wander detector uses $5 \times 187.5 \mu\text{sec}$ of photomultiplier signal in each time constant, its noise-equivalent bandwidth is 550 Hz; this is much smaller than the 3.0 kHz bandwidth of the MTF processing section, so the quantum noise on the START pulse will add negligible noise to the MTF.

E. Outputs and Controls

This section briefly lists the indicators, switches, controls, and electrical outputs that characterize the Seeing Monitor. The basic controls shown in the photograph of the control electronics box (Fig. 8) are power on-off button, motor on-off switch, image orientation knob, and magnification range selection switch. Table 3 lists the indicator, controls, and electrical outputs located at the control electronics box. A brief description of the function and characteristics of these is given in Appendix A. Appendix B shows the manner in which the serial digital data output from the Seeing Monitor is converted to parallel digital data in the Data Receiver, a separate unit that was delivered with the Seeing Monitor.

Table 3. Seeing Monitor Indicators, Controls, and Electrical Outputs

INDICATORS		
Seeing Lights		
Seeing Meter		
Wander Meter		
Wander Lights		
Brightness Meter		
SWITCHES AND CONTROLS		
Sensitivity Switch		
Motor Switch		
Range Switch		
Image Orientation Control		
Wander Reset		
ELECTRICAL OUTPUTS (BNC Connectors)		
Wander	Stop Pulse	Motor Control
Seeing front panel	MTF	Motor Speed
Seeing back panel	MTF	PM
Start Pulse	Brightness	REF
		Auxiliary

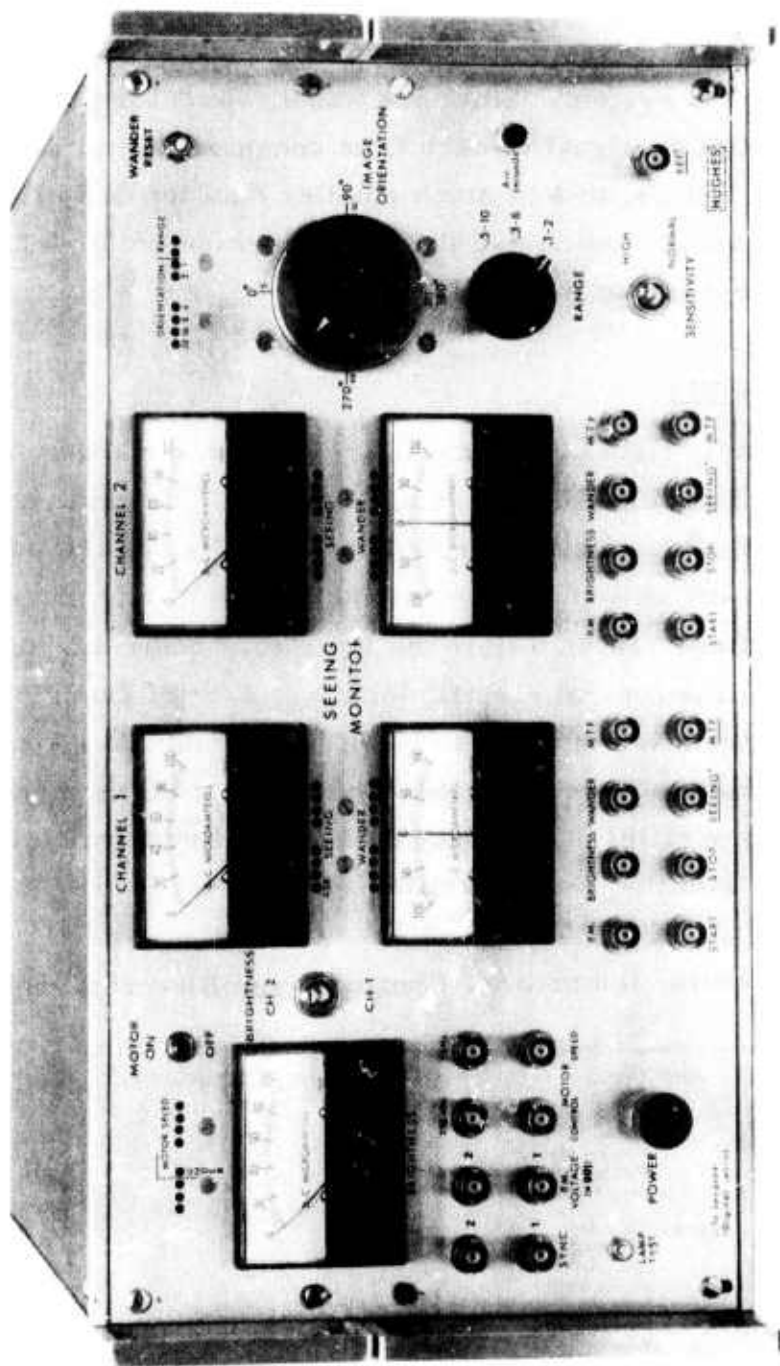


Figure 8. View of control electronics front panel.

F. Signal-to-Noise Calculations

In this section the response of the Seeing Monitor to optical signals is summarized. Appendix C contains detailed signal-to-noise calculations in which the Seeing Monitor MTF output is related to the spatial Fourier components D_I and D_Q of the projection of the star image. The response of the MTF output to quantum noise is calculated and the signal-to-noise ratio for the system's determination of seeing angle is derived. The signal-to-noise ratio is expressed as $\sigma(\theta^S)/\theta^S$ where θ^S is seeing angle and σ indicates standard deviation. Finally the signal-to-noise ratio is related to the visual magnitude of the observed star by evaluating the signal-to-noise equation for the expected light flux on the reticle wheel and using a measured value for the noise-equivalent quantum efficiency of the photomultipliers.

The result of the analysis in Appendix C is

$$\sigma(\theta^S)/\theta^S = \frac{1}{\sqrt{2} \tau_f \bar{I}} \quad (4)$$

where $\bar{I} = \int dx dy I(xy)$ is the total intensity of light (given in photoelectrons per second) falling on the reticle wheel. The bandwidth of the demodulator filters is 3.0 kHz and the characteristic time constant is $\tau_f = (\pi \times 3.0 \text{ kHz})^{-1} = 1.06 \times 10^{-4} \text{ sec}$.

We wish to express \bar{I} in photoelectrons per second generated at the photocathode of the photomultiplier tubes and then to relate this quantity to the Seeing Monitor performance for stars of different visual magnitudes, m_V . The intensity of light detected by the eye from a star of visual magnitude m is

$$I = I_o / 2.512^m = \int_0^{\infty} J(\lambda) \sigma(\lambda) d\lambda \quad (5)$$

where

$$I_o = 3.1 \times 10^{-13} \text{ W/cm}^2$$

$J(\lambda)$ = the spectral distribution of radiation from the star
in W/cm^2 per wavelength interval $d\lambda$

$\sigma(\lambda)$ = the spectral response function of the eye normalized at the response peak.

$J(\lambda)$ approximates the black body distribution for the surface temperature of the star. For stars whose surface temperatures are 6000°K and higher $J(\lambda)$ varies slowly over the wavelength interval of interest and for the purpose of this analysis J will be taken as constant.

Hence

$$I = I_o / 2.512^m = J \int_0^{\infty} \sigma(\lambda) d\lambda \equiv J\Sigma \quad (6)$$

and

$$J = \frac{I_o}{2.512^m \Sigma} \quad (7)$$

The number of photoelectrons emitted per second per unit area from the surface of the S20 photocathode is

$$\bar{I}/\text{Area} = \int_0^{\infty} J(\lambda) S(\lambda) d\lambda \approx J \int_0^{\infty} S(\lambda) d\lambda \quad (8)$$

where $S(\lambda)$ is the S20 photocathode response in photoelectrons per second per watt. Hence

$$\bar{I}/\text{Area} = \frac{I_o \int_0^{\infty} S(\lambda) d\lambda}{2.512^m \Sigma} \equiv \frac{I_o S}{2.512^m \Sigma} \quad (9)$$

To obtain \bar{I} for the photomultipliers in the Seeing Monitor on the B = 30 telescope, we must use the following expression

$$\bar{I} \text{ (Photoelectrons/sec)} = \frac{I_o S}{2.512^m \Sigma} \times A_T \times \eta_T \times \eta_s \quad (10)$$

where

$A_T = 10^4 \text{ cm}^2$, the AMOS B = 30 telescope aperture corrected for obscuration

$\eta_T \cong 0.43$ = telescope throughput

$\eta_s = 0.18$ = Seeing Monitor throughput per channel

The optical component throughputs at 6328 Å are

1 dove prism	-	0.82 each
4 lenses	-	0.96 each
5 mirrors	-	0.90 each
1 beamsplitter	-	0.45 per channel

hence $\eta_s = (0.82)(0.96)^4(0.90)^5(0.45) = 0.18$.

The value for $\Sigma = \int_{\sigma} S(\lambda) d\lambda$ was obtained by numerical integration of the photopic eye response curve (Fig. 9) $\Sigma = 1069 \text{ Å}$. The value for $S = \int S(\lambda) d\lambda$ was obtained from numerical integration of the manufacturer's spectral response curve for the extended S20 photocathode (Fig. 10).

$$S = 3.73 \times 10^5 \text{ mA} \cdot \text{Å}/W = 2.33 \times 10^{21} \frac{\text{p.e./sec} \cdot \text{Å}}{W}.$$

Using the above values for the quantities in eq. (10) we obtain

$$\bar{I} = \frac{5.22 \times 10^8}{2.512^m} \text{ p.e./sec} \quad (11)$$

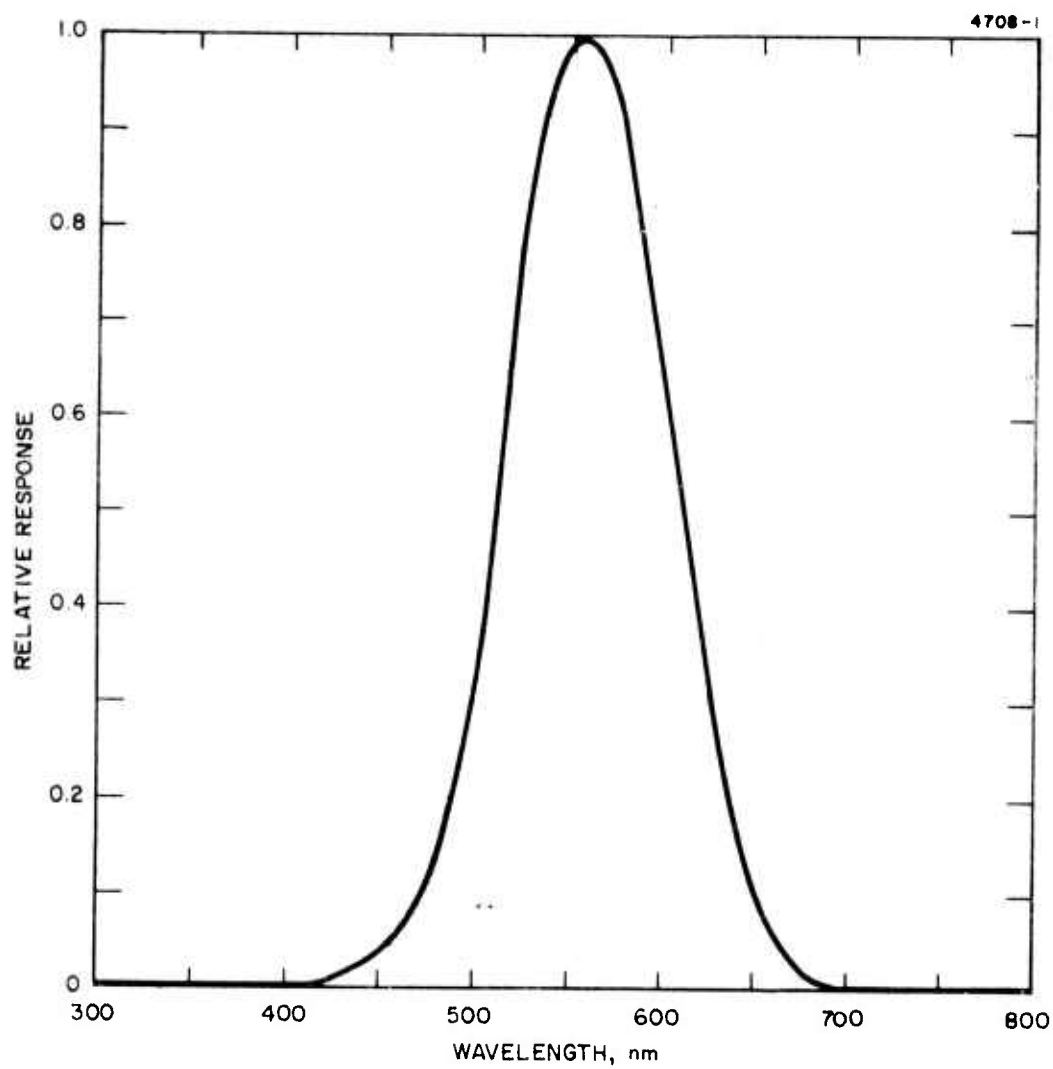


Figure 9. Relative response for photopic vision.

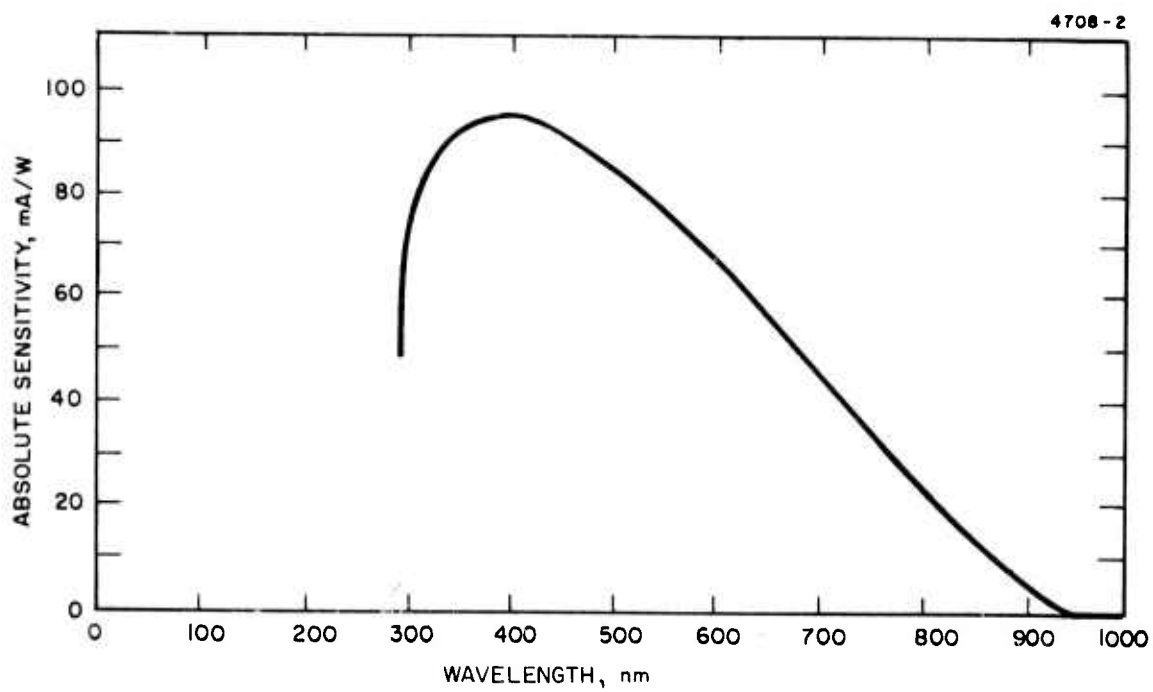


Figure 10. Spectral response of EMI extended red S20 photocathode (96" 8R).

The noise equivalent photoelectrons per second is the above expression multiplied by $F = 0.30$, the form factor converting quantum efficiency to noise equivalent quantum efficiency (see Appendix E). Hence

$$\bar{I} = \frac{1.57 \times 10^8}{2.512^m} \text{ p.e./sec.} \quad (12)$$

Therefore eq. (4) gives

$$\frac{\sigma(\theta^s)}{\theta^s} = \frac{1.585^m}{1.82 \times 10^2} \quad (13)$$

Figure 11 plots this relation between standard deviation of seeing angle and stellar magnitude. If we take a standard deviation of 0.1 for the performance limit of the Seeing Monitor we see that the system is expected to perform out to $m_V = 6.5$, a value that is in good agreement with the telescope tests (see Section G).

G. System Tests

1. Laboratory Tests and Calibrations

After final assembly and electronic checkout of the Seeing Monitor the system was set up on an optical table so that it could be optically aligned and a series of calibration measurements were carried out. The $f/15.4$ input cone of the AMOS $B = 30$ telescope was simulated using a collimated He-Ne laser source and an external lens that provided a diffraction limited focused spot at the entrance to the Seeing Monitor in the same plane that the telescope's prime focus occurs. The $f/15.4$ external focusing lens was mounted on a precision xyz stage so that the simulated star image could be translated and defocused by known amounts. Calibrated neutral density filters were also used for simulation of stars of different visual magnitudes.

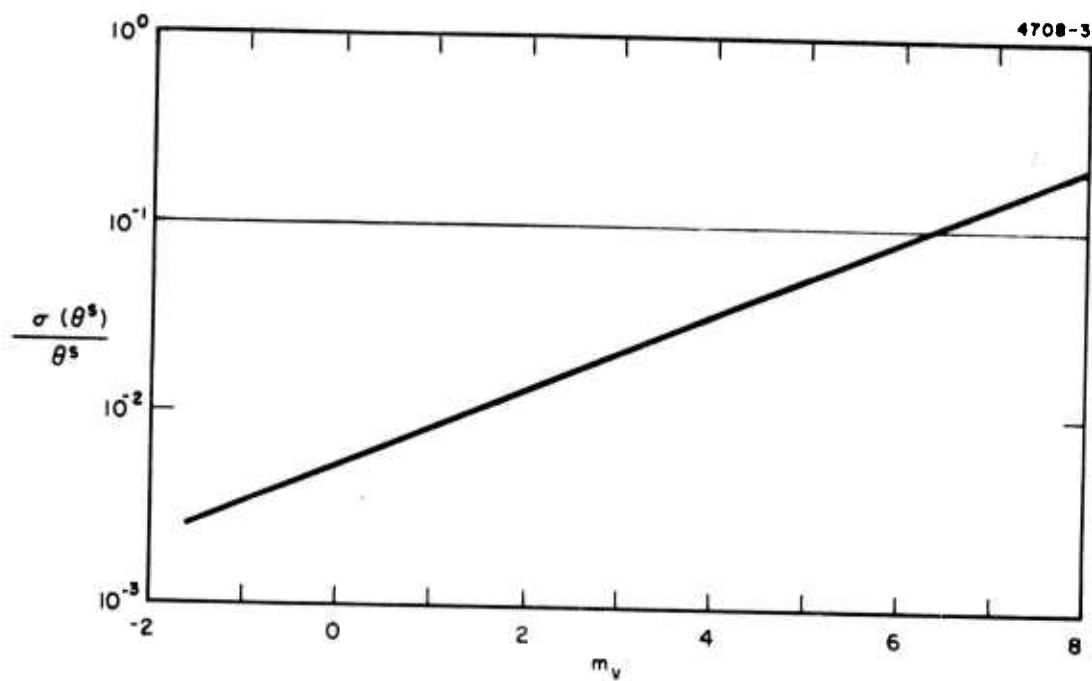


Figure 11. Seeing angle standard deviation versus stellar magnitude

The following tests and measurements were performed:

- Calibration of Seeing Meters and Seeing Lights
- Calibration of Wander Meters and Seeing Lights
- Calibration of Orientation Lights
- Field of View Measurements
- Optical Transmission Measurements

Details of the above measurements have been described in the Seeing Monitor Manual from which appropriate sections have been selected and presented in Appendix D.

2. Final Acceptance Tests at AMOS

During the last two weeks of the program the Seeing Monitor was shipped to AMOS for final acceptance tests. The system was found to perform satisfactorily.

During the first week of the test period and for two days of the second week the Seeing Monitor was aligned and mounted on a specially made side Blanchard plate and preliminary bench tests were performed to assure that the system was operating properly and that it suffered no damage in shipping. The system was then mounted on the B = 30 telescope and the tests continued on the mount.

3. Telescope Test Results

In addition to optical alignment and general checkout on the mount, the following tests were performed while the Seeing Monitor was on the telescope.

- Field of View Tests
- Image Rotation Tests
- Sensitivity Tests

Results of the above tests are described in the following paragraphs. For all the tests described the best focus was obtained by driving the secondary mirror back and forth while viewing the seeing meters. The secondary mirror position that gave the highest seeing meter reading was chosen as the best focus condition.

4. Field of View Tests

For these tests the star image was first centered in the field of view of the Seeing Monitor. Centering of the image was accomplished by pointing the telescope in the direction that gave a zero reading on the wander meters for both channels. Next the telescope was stepped by known angular amounts in the four different directions (North, South, East, and West) until the image was vignetted at the field of view stops located between the reticle wheel and the photomultiplier tubes. Vignetting was signaled by a degradation of the PM chopping patterns viewed on an oscilloscope, as well as by the observation of a marked change in the seeing meter readings. The total angular travel required to vignette the beam for a particular series of linear steps was defined as the field of view. The results of these tests are summarized in Table 4 and compared with the laboratory results that were obtained at HRL.

Table 4. Field-of-View Test Results

Range Setting	Field of View, $\overline{\text{sec}}$	
	Lab Tests	Telescope Tests
1	28	25
2	70	60
3	130	120

It should also be noted that the seeing angle as determined by reading the seeing meters was constant to within $\pm 10\%$ over the entire field of view. (Eighteen points were observed for Range 2 (0.3 to 6 $\overline{\text{sec}}$); the average seeing angle was 1.40 $\overline{\text{sec}}$.)

5. Image Rotation Tests

The purpose of these tests was to monitor the Seeing Monitor operation for different positions of the dove prism image rotator. The primary purpose was to assure that the star image remained in the center of the field of view independent of the image rotator orientation. In addition,

it was of interest to note the seeing angle readings as a function of image orientation and if possible to correlate any image asymmetry observed with the dove prism orientation setting. The experiment was performed under the following conditions:

Star selected - Vega
Visual magnitude - 0.14
Bandpass filter - 900 Å
Wind velocity - 20 mph
Image Rotation Increments - 22.5°

For all three magnification ranges the average position of star image stayed within $\sim \pm 10\%$ of the field of view (as indicated by the wander meters) over the full range of orientation steps from 0 to 360° .

Although there was asymmetry in the seeing angle for the orthogonal components of the image scans (Channels 1 and 2) there was no apparent correlation for this asymmetry for image rotations separated by 180° . The maximum asymmetry observed for Range 2 (0.3 to 6 sec) was $\sim 30\%$ at one angular setting of the dove prism; however the asymmetry for the angular setting corresponding to a rotation of 180° from the above was only $\sim 5\%$.

The gusty wind conditions under which these measurements were made may have been a dominant factor in determining the kind of behavior observed. Additional data must be taken under more quiescent conditions to shed further light on the above behavior.

6. Seeing Monitor Sensitivity Test

The sensitivity of the Seeing Monitor was tested by viewing stars of different magnitudes and noting the readings of the seeing meters. As the input light level to the Seeing Monitor decreases the signal to noise ratio reaches a value where the seeing angle outputs are too noisy to be meaningful. Because of time limitations during the AMOS acceptance tests and because of the inability to record digital seeing angle data it was not possible to perform a statistical analysis of the measured seeing angle data and hence to compare quantitatively the noise limited performance characteristics. Instead the seeing meter readings which give average seeing angle values with integration times of about 0.05 to 0.1 sec were noted for bright

stars and the readings were compared for dimmer stars. It was found that the values obtained were in good agreement (20%) over a range of stellar magnitudes from 0.24 to 6.8. These tests were performed using the mid-range magnification setting, Range 2 (0.3 to 6 $\overline{\text{sec}}$). Optical bandpass filters were not employed in these tests.

The results of these measurements is presented in Table 5.

Table 5. Seeing Monitor Sensitivity Test on B = 30 Telescope

Star Name or Number ^a	Visual Magnitude	Elevation, Degrees	Seeing Meter Reading		Seeing Angle, $\overline{\text{sec}}$	
			Channel 1	Channel 2	Channel 1	Channel 2
α Bootes	0.24	59	42	42	1.35	1.35
α Scorpius	1.22	43	44	44	1.25	1.25
288	2.65	66	42	42	1.35	1.35
1061	3.48	78	42	42	1.35	1.35
1070	4.48	77	42	42	1.35	1.35
2093	5.48	—	42	42	1.35	1.35
2107	6.00	44	40	42	1.50	1.35
2062	6.41	67	38	40	1.65	1.50
2090	6.79	70	38	38	1.65	1.65
^a Catalogue numbers from AMOS Star Catalogue						

It can be seen from the entries in the table that the Seeing Monitor gives ~20% agreement over a range of stellar magnitudes down to the dimmest star observed during the tests ($m_V = 6.8$). The apparent improvement in sensitivity over laboratory results in which performance was seen to degrade for simulated stellar magnitudes of about $m_V = 5$ may have arisen from the reduced temperature of the photomultipliers and associated on-board electronics when the system was operated in the dome.

According to the manufacturer's data on the temperature dependence of the dark current for the extended red S20 photocathode material employed in the photomultiplier tubes there is approximately a factor of 10 reduction in cathode dark current between 20°C and 4°C . (The above temperatures are the approximate laboratory and dome temperatures respectively.) Because we did not carry out dark current measurements on the photomultiplier tubes used in the Seeing Monitor it is not clear to what extent the low signal performance is affected by dark current noise and hence to what extent, if any, the performance might be expected to improve as the temperature is lowered. Nevertheless the Seeing Monitor sensitivity as operated on the $B = 30$ telescope is close to that predicted from the analysis presented in Section F. The apparent discrepancy between bench test sensitivity and telescope test sensitivity remains open to explanation.

7. Observation of Chromatic Aberration for Range 3

During the initial checkout phase of the Seeing Monitor telescope tests a marked asymmetry was observed in the seeing meter readings for the two channels when the magnification setting was on Range 3 (0.5 to 10 sec), an asymmetry that was not present on the two other settings. It was found that the asymmetry disappeared when the spectral bandwidth of the light detected by the Seeing Monitor was reduced and hence the effect is attributed to chromatic aberration in the relay lens used for magnification Range 3.

A series of tests were performed in which the seeing meter readings were compared for white light and for the four different bandpass filters that are used for atmospheric dispersion correction. Four different spectral bandpass filters were delivered with the Seeing Monitor; they have transmission maxima centered around 6000 \AA , peak transmittance between 80 and 85%, and widths of 640, 900, 1200, and 1800 \AA .

The results of the bandpass filter tests for Range 3 are summarized below.

<u>Seeing Meter Reading</u>		<u>Filter</u>
<u>Channel 1</u>	<u>Channel 2</u>	
20	37	None
48	48	640 Å
47	47	900 Å
46	46	1200 Å
34	36	1800 Å

We see from the above data that the three narrowest bandpass filters give essentially the same seeing angle reading. While the asymmetry observed with white light is essentially absent for the 1800 Å filter, there still appears to be a significant amount of chromatic aberration albeit symmetrical. From these results it is recommended that one of the three lowest bandpass filters be employed whenever Range 3 is used. No significant chromatic effects were observed at the other magnification settings.

8. Seeing Monitor Performance Summary

The following summarizes the results of Seeing Monitor tests both in the laboratory and on the AMOS B = 30 telescope.

Sensitivity - Good performance demonstrated at $m_v = 6.7$ (telescope tests).

Practical Seeing Ranges - Range 1 - 0.14 to 2 $\overline{\text{sec}}$

Range 2 - 0.8 to 6 $\overline{\text{sec}}$

Range 3 - 1.8 to 10 $\overline{\text{sec}}$

Field of View - Range 1 - 25 $\overline{\text{sec}}$

Range 2 - 60 $\overline{\text{sec}}$

Range 3 - 120 $\overline{\text{sec}}$

Image position remains fixed in field of view independent of orientation of dove prism

Seeing meters give constant values independent of orientation of dove prism

Seeing meters give constant values independent of position of image in field of view.

III. PRIMS EXPERIMENTAL DESIGN TEST PROGRAM

A. Introduction

Under the previous contact,¹ the feasibility of the PRIMS concept was demonstrated for a modulated argon laser system with long optical pulse lengths and modest optical power. The purpose of the experimental phase of the present program was to evaluate the PRIMS concept as it applied to a high power Q-switched ruby laser system. The general objectives of the program were:

- (1) To test feasibility of frequency translating 30 nsec optical pulses through 150 MHz
- (2) To test a beam recombination frequency translation scheme for orthogonally polarized pulses
- (3) To test the feasibility of heterodyne detection and phase synchronous detection of 30 nsec duration 150 MHz frequency translated pulses
- (4) To fabricate and test 10 fiber optic delay lines with 60 nsec increments
- (5) To evaluate suitable high speed data recording techniques.

To satisfy these objectives an approach was planned which included the following experiments and studies:

1. Approach

A chopped argon experiment was designed to satisfy objective (1): In this design ± 75 MHz frequency translated cw argon beams are combined, chopped via a rotating prism, and detected via glass fiber coupled into a fast photomultiplier.

¹ Final Technical Report, "Space Object Imaging Techniques," June 1974.

A pulsed ruby experiment was designed to satisfy objectives (1), (2) and (4). This experiment included a 150 MHz frequency translator, a glan prism beam dissection-recombination system, and a small aperture before the photomultiplier to simulate the small cross section of a fiber optic element.

A fiber optic experiment was designed to satisfy objective (4): In this experiment a fiber optic bundle containing 10 fibers interconnects the laser output and the photomultiplier input.

Data recording studies were outlined to satisfy objective (5).

The experimental program plan was followed with a few exceptions and is reported in detail below. Deviations from the plan were caused for the most part by late delivery of optical components and optical fibers. In one case a critical component, the acousto-optic modulator proved too costly for this phase of the program because most off the shelf devices could not meet the power handling requirements and the component could not be developed on short notice. Thus an existing acousto-optic Q-switch was substantially modified and used for this program. Late fiber delivery also forced a change in measurement priorities resulting in testing of the fiber optic lines at the end of the program.

A high quantum efficiency photomultiplier originally selected for this program proved to have inadequate frequency response because of its long fall time. Its replacement, a lower quantum efficiency, fast response tube required additional testing and impedance matching to minimize spurious impulse response effects.

The Experimental Measurement Program phases and the information sought in each phase are detailed below.

The chopped argon experiment was designed to test the feasibility of photomixing two 30 nsec optical pulses separated in frequency by 150 MHz and coherently measuring the relative optical phase of these two waves using a coherent 150 MHz reference signal. Another goal was to evaluate propagation of these waves through a short optical

fiber coupled to a photomultiplier. In this experiment the output of a cw laser was frequency translated (by ± 75 MHz) and then chopped to obtain the 30 nsec pulses.

The pulsed ruby experiment differed from the argon experiment in that a high powered short duration pulse was obtained from a laser and amplifier system and frequency translated and untranslated pulses were generated and recombined using a glan prism optical system identical to that proposed for the field experiment option, thereby testing the feasibility and stability of this scheme. Finally the feasibility of heterodyne detection of these frequency translated pulses via a small aperture and measuring their optical phase in a receiver approximating that proposed for the field experiment was established in this experiment. In this part of the experiment a small iris of 0.005 in. diameter placed before the photomultiplier simulated the effective capture cross section of an optical fiber delay line. The power handling capability of various optical components including acousto-optic modulator, glan laser prisms, and a half wave plate were also tested in the course of this experiment.

A set of 10 multimode fiber optic delay lines was assembled having incremental delay changes of 60 nsec and tested for insertion loss and dispersion. Because of the anticipated difficulty of providing uniform laser illumination input to the fibers from a collimated-nonspatially filtered source, and the expected lack of photocathode local uniformity the attenuation data was obtained by changing the fiber input and output positions.

The data recording studies consisted of consultation meetings with electronic signal processing groups at other parts of Hughes Aircraft Company.

B. Chopped Argon Laser Experiment

The purpose of this experiment was to generate a pair of 30 nsec duration 150 MHz frequency translated optical pulses to test

the response of the complete receiver train including PMT and polar phase detectors when illuminated by short optical pulses. A novel acousto-optic scheme shown in Fig. 12 was used to generate a 150 MHz heterodyne optical signal from an ultrasonic frequency translator driven at 75 MHz. The laser beam traversed the modulator and produced a down-shifted optical beam ($f_o - f_a$) which was retrodirected through the modulator and into a telescope. The other diffracted laser beam passing through the modulator was also retro-directed and yielded an upshifted beam at frequency $f_o + f_a$, which also passed collinearly into the telescope. The two beams were then brought to a focus at the position of a small optical fiber connected to photomultiplier 2 via a fixed mirror (M1) and a rotating prism. The length of optical path between the prism and the fiber, and the focal length of the telescope were adjusted so that the optical signal pulse generated by the prism rotating at 400 rps (24,000 rpm) produced a pulse of 20 to 30 nsec duration at the glass fiber feeding photomultiplier 2. The output of this photomultiplier was passed through a 100 MHz high pass filter and then processed in a polar phase detector. The position of another fiber feeding photomultiplier 1 was adjusted vertically so that the optical beam crossed this fiber about 100 nsec early and led to the generation of a trigger pulse for synchronizing the oscilloscope.

Part of the power out of the 75 MHz rf oscillator was amplified and fed into the acousto-optic modulator, the other part was passed into a frequency doubler to generate a 150 MHz reference signal. This signal after amplification was used as a 150 MHz reference in the polar phase detector (see Fig. 13). The polar phase detector outputs exhibited significant rf leakage signals at 150 and 300 MHz and the output lines were filtered with a 100 MHz low pass filter to remove these leakage signals.

The laser pulse after passing through the glass fiber is shown in Fig. 14(a). The pulse width is approximately 25 nsec. With the optical system adjusted to give a maximum video signal, the photomixed

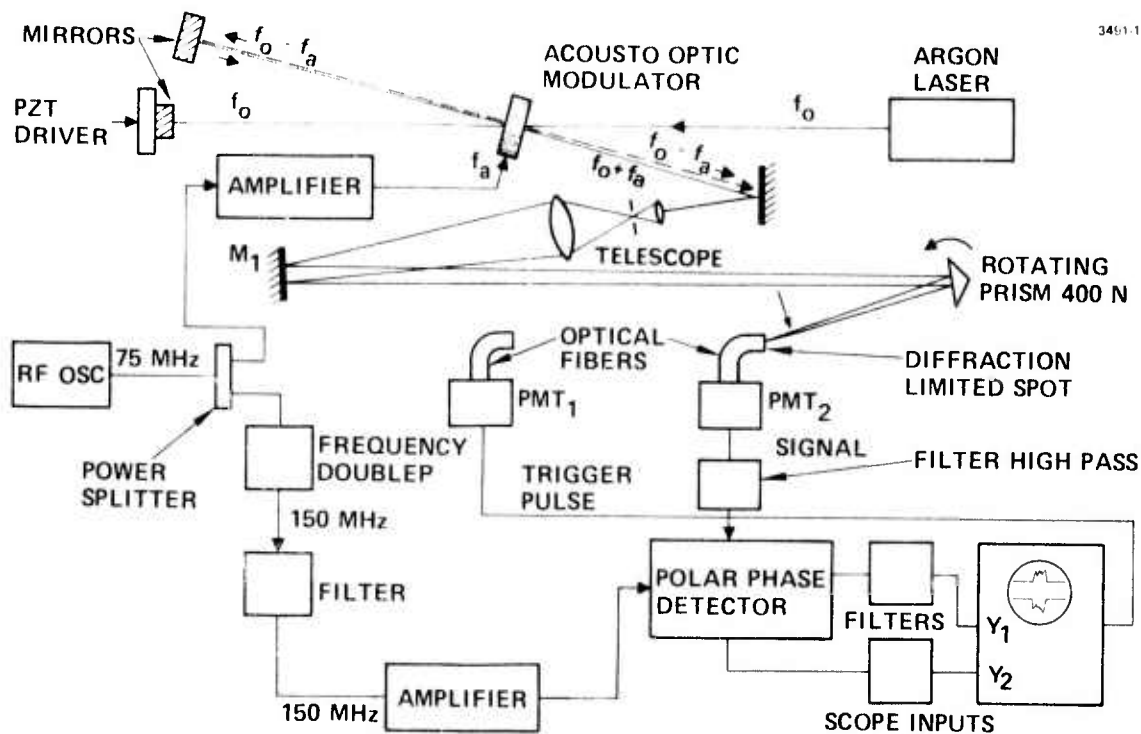


Figure 12. Chopped argon experiment.

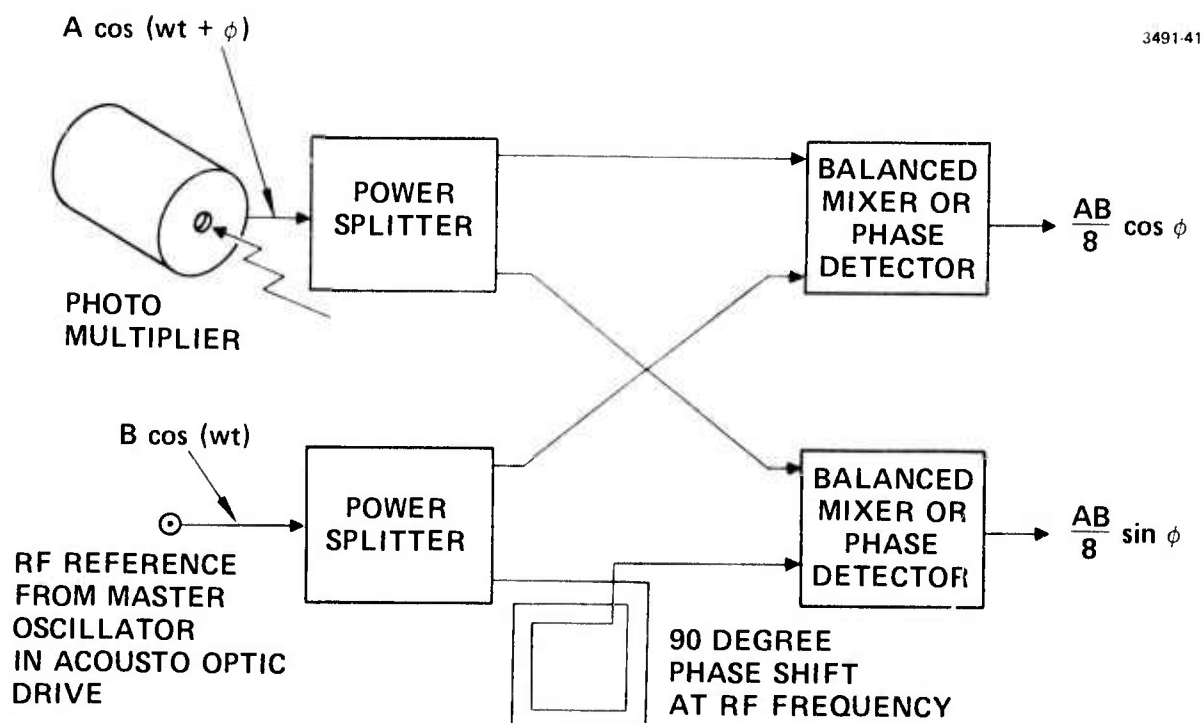
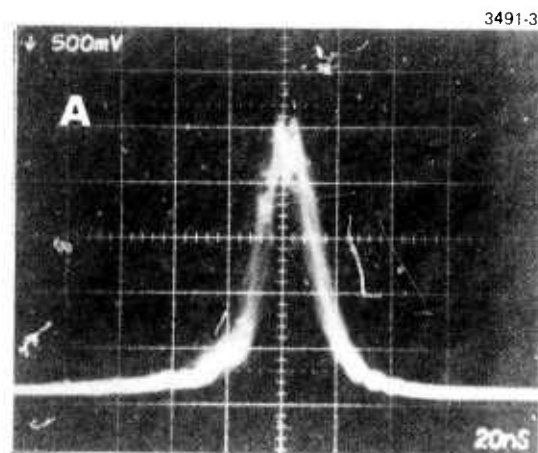


Figure 13. PRIMS phase detector system.

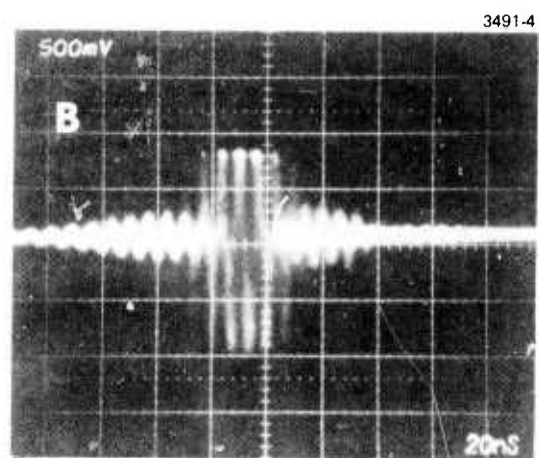
signal is shown in Fig. 14(b) after filtering through the high pass rf filter. Figure 14(c) shows the individual cycles in the rf pulse obtained by taking advantage of the high frequency synchronization capability of the oscilloscope. The rf side lobe effects are attributed to slight residual misalignment of the heterodyne optical beams and diffraction lobe structure in the focused optical beams. Figure 14(d) shows the heterodyne receiver output signal when either of the optical beams is blocked.

The optical heterodyne signal voltage is proportional to the rf power used to drive the acousto-optic frequency translator in this set of experiments. Thus if the rf drive signal is attenuated by x dB the optical signal is attenuated by $2x$ dB. In the experiment when the rf drive was attenuated by 13 dB the heterodyne optical signal-to-noise ratio was 1. Thus the heterodyne optical signal-to-noise ratio was 26 dB. Another 7 dB loss factor at 150 MHz was introduced by the 100 MHz high pass rf filter placed on the output of the photodetector to prevent the video part of the signal from overloading or damaging the low noise wide band amplifier which feeds the phase detector. It is feasible to reduce this 7 dB loss in signal-to-noise ratio by using a better filter and/or some rf amplification before the filter. Thus the signal-to-noise ratio before filtering is estimated at 33 dB. The total optical power reflected from the rotating prism was 2 mW but it was found that only part of this power was transmitted through the optical fiber system (about 50%) so that the optical signal-to-noise ratio is even higher than the measurements indicate. This method of measurement using rf drive attenuation was more convenient than placing attenuators in the path of the optical beams.

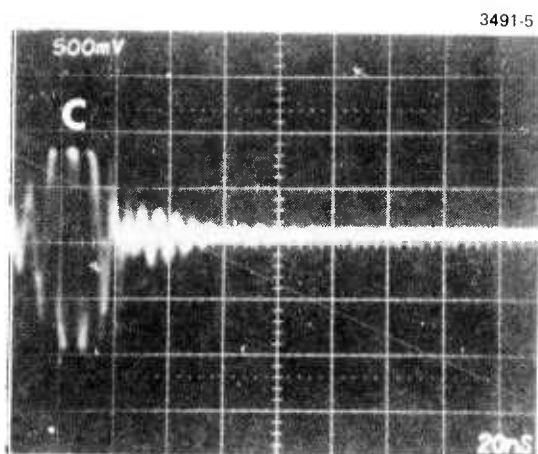
Figure 15 shows the filtered output from the polar phase detector with the relative path length of the two frequency translated optical beams adjusted to demonstrate phase angles of approximately 45, 135, 225 and 315 degrees. The pulsed phase data showed ringing or overshoot phenomena, which is attributed to optical misalignment



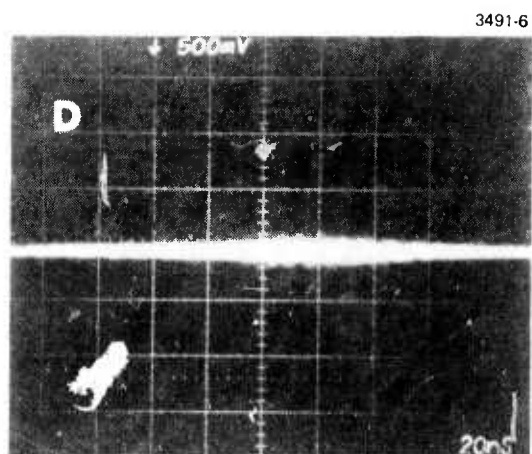
VIDEO PULSE FROM PMT VIA FIBER



RF FILTERED AND AMPLIFIED PULSE

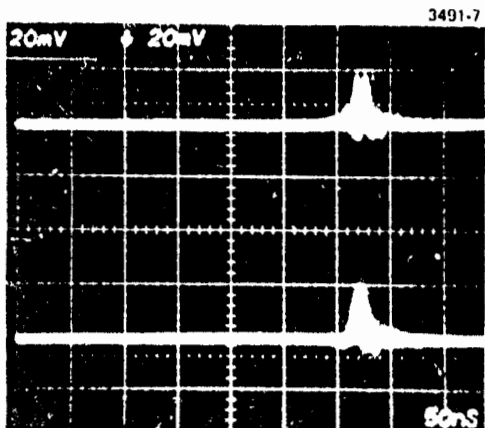


HF SYNC SHOWING INDIVIDUAL CYCLES IN PULSE

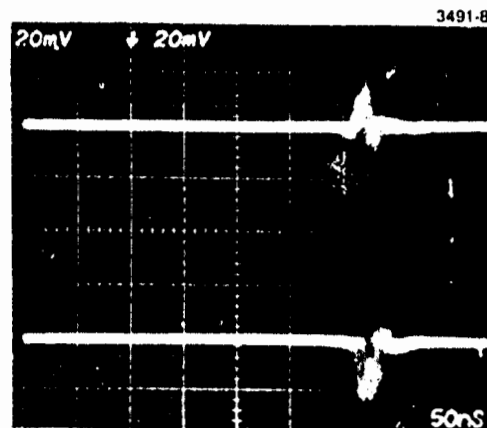


RF PULSE OUTPUT WITH EITHER OPTICAL BEAM CUT OFF

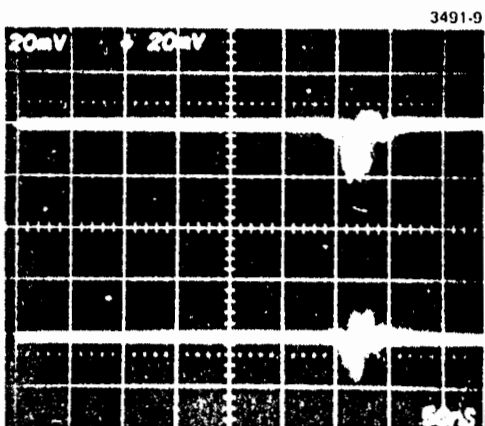
Figure 14. Video and rf signals in chopped argon experiment.



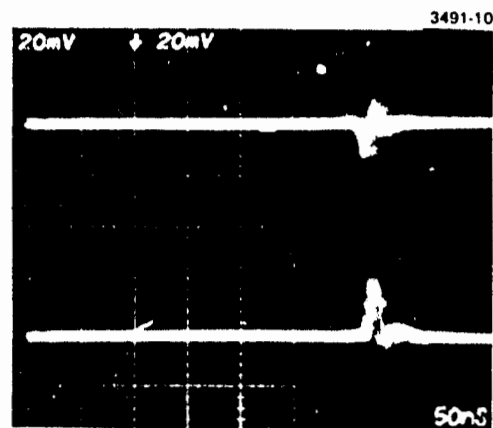
PHASE DETECTOR OUTPUT
 $0 \leq \theta \leq 90^\circ$



$90^\circ \leq \theta \leq 180^\circ$



$180^\circ \leq \theta \leq 270^\circ$



$270^\circ \leq \theta \leq 360^\circ$

Figure 15. Phase detector output signals in chopped argon experiment.

of the beams. Two optical beams can be collinear and parallel enough to produce heterodyne photomixing, but still be slightly angularly misaligned. Thus the rotating pair of slightly misaligned beams produce a pair of pulses at the photodetector which generate an rf heterodyne output signal whose phase varies during the pulse. In the experiment with 2 mm optical beam diameter, a , the heterodyne criterion is $\theta \leq \lambda/8a \approx 3 \times 10^{-5}$ rad. Therefore, the optical beams can efficiently photomix when misaligned by as much as 30 μ rad, and if the composite beam is scanned one expects to find a variation in optical phase from one edge to the other. The phase error across the beam corresponds to 45° in the best case and can easily be a factor of 2 larger.

The experiment has demonstrated that one can phase detect the heterodyne output from 2 photomixed optical beams as short as 30 nsec. It was performed under conditions leading to signal-to-noise ratios of the order of 30 dB. The observation of phase variation across the pulse has been satisfactorily explained, but it raises another interesting question concerning the extended nature of the satellite or space object; i. e., if the space object has structure in depth corresponding to 20 m, then the returning signal will be stretched in time by an amount $T = 66$ nsec. It is possible that local surface conditions will yield different phase shifts for different time zones in the target return signal. Measuring the average values of the return pulses at the output of the polar phase detectors may give rise to ambiguous results. Some preliminary thinking about this problem has led to a valuable alternative approach to signal processing. This approach requires that the phase detector output pulses be sampled in time instead of being integrated. The target returns should be quantized into time zones (or depth zones). Recalling now that the specular returns from the target glints will not be spread out in time (if there are a small number of glints), one sees that time sampling of the target returns may lead to some automatic reduction of the redundancy expected from multiple glints. Implementing this approach requires

a high bit rate, fast analog-to-digital data processing and storage system. Also a reduced dynamic range will occur because of the reduction of pulse integration time introduced by the sampling process.

C. Pulsed Ruby Laser Experiment

The most critical experiment in the PRIMS test program was the pulsed ruby experiment whose purpose was to simulate in the laboratory both the transmitter and the receiver portions of the PRIMS field experiment. The essential difference between the laboratory and the field experiments was that the laboratory experiments made use of a single pulse (low repetition rate) laser of modest total power whereas the field experiment will use a high repetition rate (20 ppm) high total power laser, the power density of both lasers, however, being nearly equal. The detailed objectives of the experiment were as follows:

1. To test power handling capability of glan laser prisms and wave plate
2. To determine effectiveness of the beam splitting recombination scheme
3. To measure parameters of single glint pulse optical heterodyne signals
4. To develop alignment techniques
5. To verify high frequency characteristics of photomultiplier receivers
6. To test feasibility of synchronizing a pulsed acoustic modulator with a dye Q-switched laser system (time jitter).

To obtain these objectives the apparatus shown in Fig. 16 was constructed and assembled. Figure 17 is a block diagram of the apparatus showing all of the electronic and optical components. The single mode dye Q-switched ruby laser output signal is passed through a ruby amplifier rod and then through a pair of auxiliary glan prism attenuators which can be axially rotated to control the available power in an

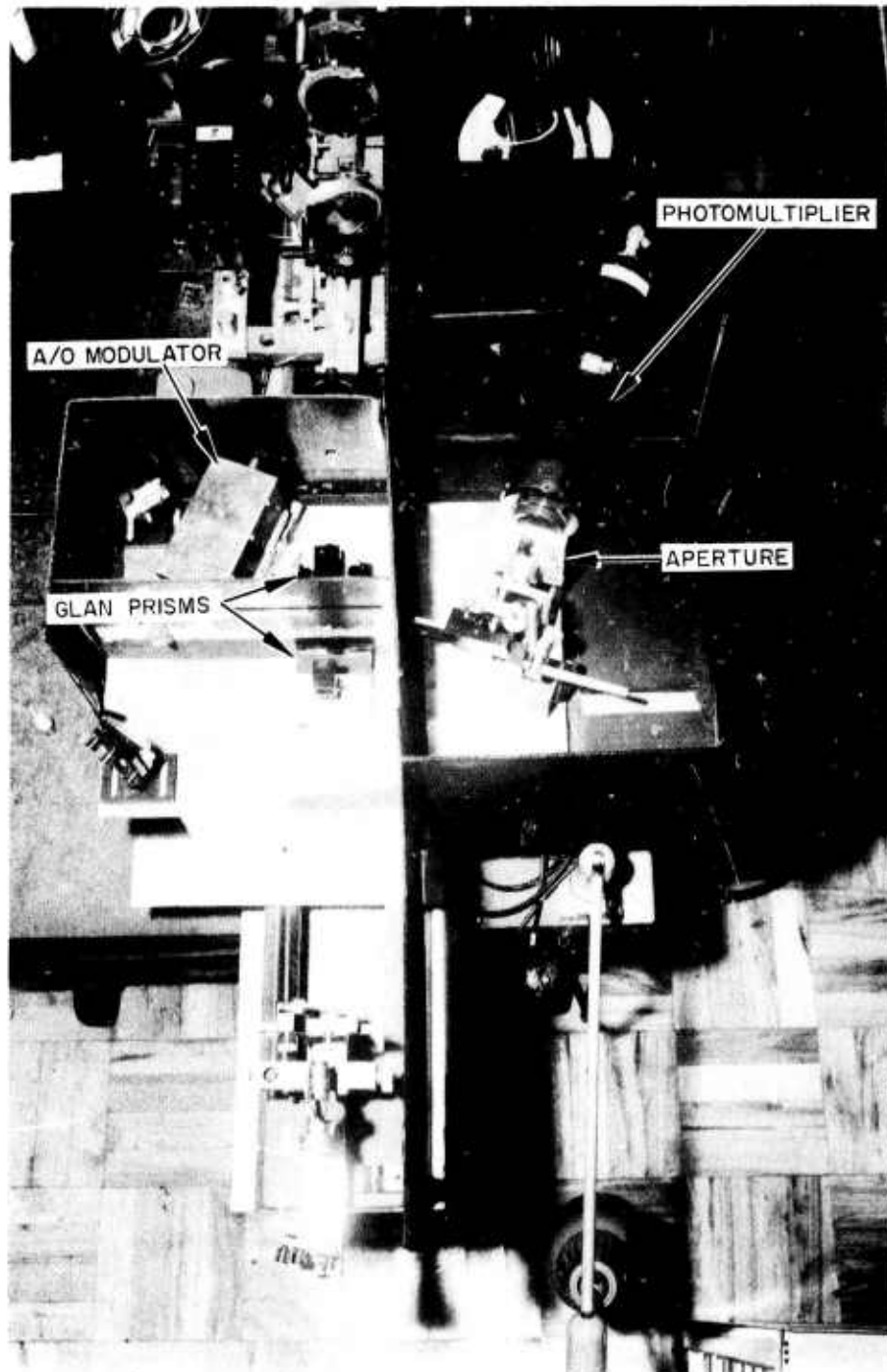


Figure 16. Pulsed ruby experiment apparatus.

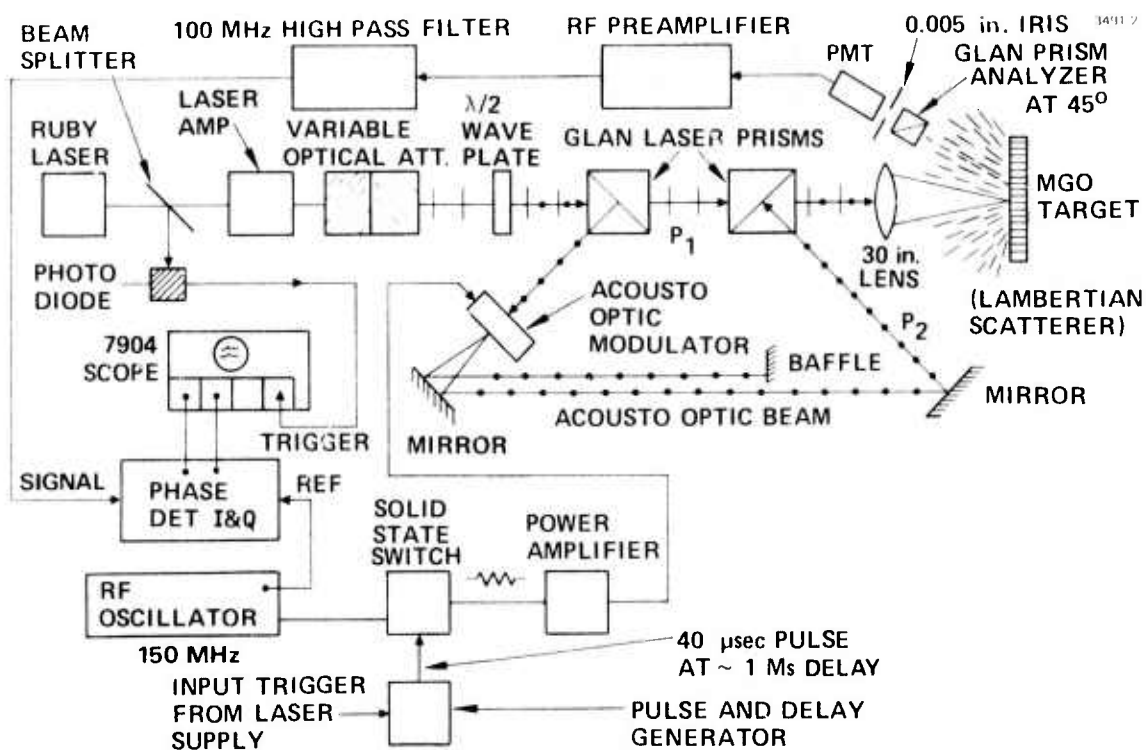


Figure 17. Block diagram of pulsed ruby experiment.

experiment. Not shown in this diagram is an elaborate helium neon laser system for alignment of the laser crystal and the input and output mirrors before the ruby laser system is activated. The optical axis of the half-wave plate between the variable attenuator and the first glan laser prism can be rotated causing the laser polarization to rotate through an angle of twice the wave plate rotation. The first glan laser prism then resolves the rotated polarization wave into two orthogonal polarizations, one of which passes through the acousto-optic modulator, and the other through the second glan laser prism undeviated. The acousto-optic modulator produces two beams, an angularly deviated frequency translated beam, and a beam having the same frequency as the incident beam that is not deflected. After these beams are reflected from mirror (1), a baffle blocks the non-frequency translated beam. The frequency translated beam reflects from mirror (2) and enters the second glan laser prism at the same angle that the untranslated beam left the first glan prism. The two oppositely polarized frequency translated optical beams then recombine in the second glan laser prism, pass through a 30 in. focal length lens and are brought to a focus at the magnesium oxide target. At the target, the superimposed beams are scattered through a large angle to attenuate the high optical power. Part of the scattered power from each polarization enters the glan prism analyzer, oriented at 45° , so that it passes a component of each polarization (and frequency). The light transmitted through the analyzer is further attenuated by a 0.005 in. pinhole placed before the photomultiplier detector to simulate the entrance aperture of a 0.005 in. multimode fiber optical delay line. The output of the photomultiplier is passed through an rf pre-amplifier and a 100 MHz high pass filter to eliminate the video portion of the signal and is then passed into a phase detector. The rf phase reference signal to the phase detector is derived from a 150 MHz oscillator. The phase detector output signals (designated I and Q for inphase and quadrature) are displayed on a high speed oscilloscope which

is triggered by the output of a high speed photodiode which samples the laser oscillator output. Most of the power output from the rf oscillator is passed through a solid state microwave switch, an rf power amplifier and then into the acousto-optic modulator. The switch pulse width and time delay are controlled by a pulse and delay generator triggered from the laser power supply.

D. Acousto-optic Modulator Development

Early in the development program, bids were sought for development of an acousto-optic modulator capable of handling peak powers of the order of 100 W/cm^2 with a 2 cm beam cross section. The price quotations were high and the delivery time too long to be useful in this concept evaluation phase. For laboratory use a 50 MHz acousto-optic Q-switch was modified for operation at 150 MHz. The fundamental resonant frequency of the device was below 50 MHz causing inefficiency at 150 MHz. Special impedance matching circuitry was developed to improve performance at this frequency. The modulator showed about 4% modulation with about 16 W of rf drive which proved adequate for most of our concept evaluation experiments. The modulation medium was fused quartz, antireflection coated for a wavelength other than 6943 \AA . This caused some spurious reflections which fortuitously did not seriously interfere with the experiment.

E. Synchronization of Acoustic Pulse with Laser Pulse

In the field version of this experiment a high efficiency acousto-optic frequency translator will be required to frequency shift the orthogonally polarized laser beam. Studies of available modulators (custom) indicate that a 150 MHz modulator will require an rf drive level of 100 W in order to yield 50% diffraction efficiency with a 2 cm optical beam. The modulators cannot be operated at 100% duty cycle at this power level, but they can be operated in a repetitively pulsed mode in synchronism with the Q-switched laser pulse.

We have succeeded in accomplishing this synchronization with both a nonrepetitive (single shot) and a repetitive laser. First the laser flash lamp trigger pulse was used to trigger a pulse generator with variable time delay and pulsewidth. A sync pulse from the pulse generator was used to trigger an oscilloscope which displayed both the pulse generator output and the output of a photodiode which received part of the laser energy. By adjusting the time delay of the pulse generator output and the pulsewidth it was found possible to bracket the short laser pulse with the longer electrical pulse. The time delay required was of the order of 2 msec and the pulse jitter was of the order of 0.2 msec so the pulse length chosen was 200 μ sec. This 200 μ sec dc pulse was then used to drive an rf switch which modulated a 1 mW 150 MHz rf signal. The pulse modulated rf signal was then amplified and fed to the acousto-optic modulator. To test the accuracy, the synchronization was tested by visually observing the diffracted pulse as well as the undiffracted energy. If the pulse synchronization or timing is incorrect the ultrasonic wave and the laser pulse will not exist simultaneously in the acousto-optic modulator and no diffracted pulse will be observed.

F. Beam Alignment Techniques

The development of techniques for collinear alignment of the frequency translated and untranslated polarizations was critical for this experiment and for the proposed field experiment. Both beams must be aligned within an angle θ equal to $\lambda/8a$, where λ is the optical wavelength and a is the detector aperture in order for heterodyne photodetection to occur with degradation less than 10%. Sophisticated alignment techniques were developed during this program and they are reported in Appendix F.

G. Optical Power Handling Capabilities

One question of concern in this program was the ability of the optical components to withstand optical powers of the order of $100 \times 10^6 \text{ W/cm}^2$. Using a single mode dye Q-switched ruby laser and laser amplifier pulses of $150 \times 10^{-3} \text{ J}$ (FWHM), durations of $14 \times 10^{-9} \text{ sec}$ (FWHM) were generated with 2.5 mm beam diameter. The pulse power density is given by

$$P = \frac{E(\text{J}) \times T(\text{sec})}{A(\text{cm}^2)} = 202 \times 10^6 \text{ W/cm}^2$$

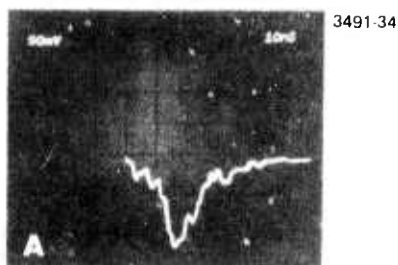
No observable deterioration of the glan prisms or the half wave plate was observed after subjecting these components to thousands of pulses.

Other optical components in the dual polarization dual frequency generator, such as the ultrasonic modulator and the mirrors, are not subject to the full laser power and were accordingly, not tested.

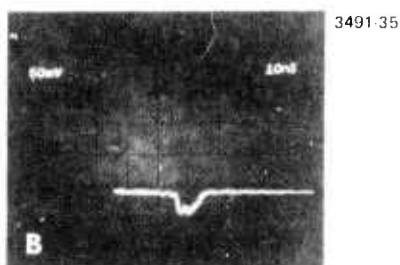
H. Experimental Results

After considerable experimental effort had been expended on developing the components and techniques needed for the experiment measurement program, data relevant to the objectives of the overall program were obtained. The first series of data is shown in Fig. 18. Using the single shot laser to excite the 30 in. lens and MGO target system and, in turn, the 0.005 in. iris and RCA-C31024A photomultiplier receiver system, various heterodyning component signals were recorded sequentially. The first series of results is concerned with medium power photomixing of pulses of about 30 nsec duration. Figure 18(a) shows the direct nonfrequency translated beam ($P_1 f_1$) at the PMT. Slight temporal structure is evident in this pulse which could not be attributed to photomixing because of the single frequency nature of the laser and the lack of an available local oscillator. Later

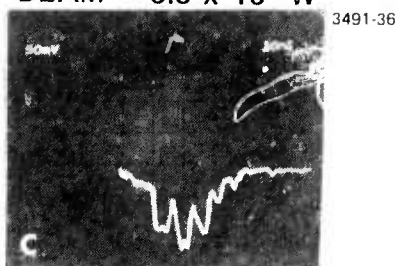
VIDEO SIGNALS



DIRECT BEAM $\approx 1.5 \times 10^{-7}W$

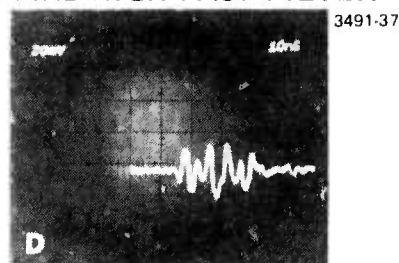


ACOUSTO OPTIC
BEAM $\approx 0.5 \times 10^{-7}W$

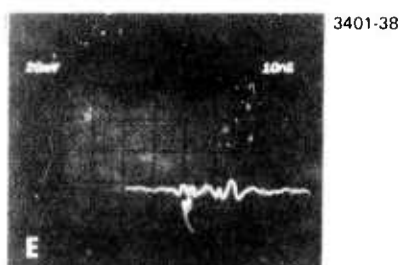


BOTH BEAMS

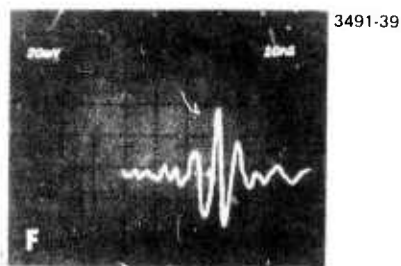
RF SIGNALS 100 MHz HIGH PASS FILTER



DIRECT BEAM



ACOUSTO OPTIC BEAM

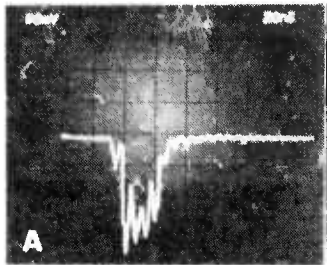


BOTH BEAMS

Figure 18. Medium power photomixing of 30 nsec pulses.

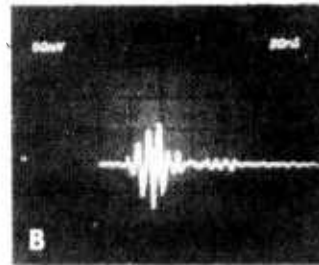
experiments have shown that this effect could be partially attributed to multipath optical propagation and quantum noise. The number of carriers generated at the photocathode is estimated at 285, the receiver bandwidth is 0.400 MHz and the full width half-maximum duration of the pulse was 12×10^{-9} sec. Figure 18(b) shows the acousto-optically translated beam with a peak power of 0.5×10^{-7} W and one observes that the pulse width is distorted (much smaller) because of the smaller number of quanta. In some experiments this pulse has appeared in the form of several spikes. Figure 18(c) shows the effect of allowing both beams to photomix at the photomultiplier. The low frequency modulation (150 MHz) is clearly in evidence. In Figs. 18(d) to 18(f) the same signals were passed through a 100 MHz high pass filter to eliminate the video (dc) part of the signal. The filtered photomixing signal (Fig. 18(f)) is clearly greater than either of the other signals, but the presence of any output without a dual frequency input is objectionable. This spurious output was attributed to structure in the incident optical pulses or ringing of the photomultiplier tube. Photomultiplier response tests made later in the program explain this phenomenon. It is important to note that each photo was taken with one shot of the laser and because of the small numbers of quanta involved each optical pulse is slightly different. However, the test of whether a short duration optical pulse could be acousto-optically frequency translated, polarization rotated, and collinearly combined with the untranslated beam and heterodyne photodetected was proven beyond a reasonable doubt.

The next series of experiments was concerned with photomixing and coherent phase detection of the photomixed filtered heterodyne output signals. Because this experiment was performed at a later time, complete data including video output, rf filtered output, and phase detector output signals were taken. Figure 19(a) and (b) shows the video and rf signals with essentially the same characteristics shown earlier. The time scale is compressed here and in Fig. 19(b) one can observe a low amplitude secondary pulse probably due to signals



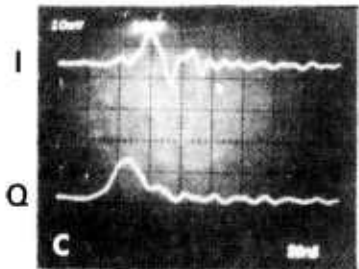
3491-30

Photo mixing at 150 MHz offset.
 $P_1 \approx 0.5 \times 10^{-7} \text{W}$ $P_2 \approx 1.5 \times 10^{-7} \text{W}$



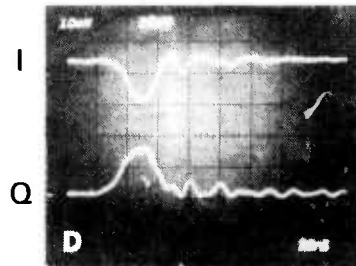
3491-31

Photo mixing signal after amplification and filtering



3491-32

Phase detector outputs for pulses
 1 and 2



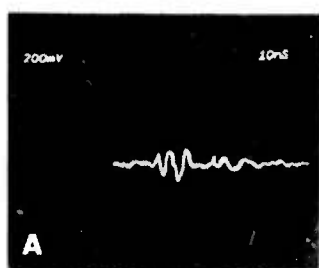
3491-33

Phase detector outputs for pulses
 3 and 4

Figure 19. Photomixing and in phase and quadrature phase detection.

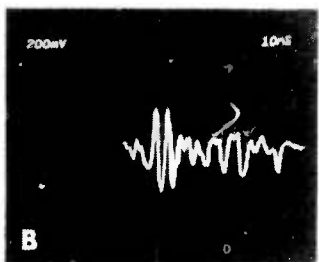
which have bounced around the room. To control the optical power reaching the PMT, n.d. filters were placed in front but scattered light could enter from the side thus allowing a secondary pulse to be recorded by the system. Figures 19(c) and 19(d) show the output of the phase detector circuit in phase and quadrature signals. The oscilloscope was capable of displaying only 1 channel at a time (single beam) so that the I and Q data are from separate shots. The phases are obviously different in Fig. 19(c) and (d) presumably due to vibration of the mirrors used in recombining the frequency translated beam with the direct beam. This phase variation due to vibration will not be a problem in the experiment, because all of the data is generated by a single transmitted pulse pair of arbitrary phase. On receive only the relative phase change between the 100 channels is measured. The presence of vibration in fact was helpful because it demonstrated that the phase detector was working. Many of these phase data traces were taken and all exhibited this random behavior corroborating our conclusions. The data in these figures was taken after using a low pass filter to remove the 150 MHz and the second harmonic (300 MHz) generated in the phase detector. Since there was some possibility of the low pass filter (≈ 75 MHz) distorting the phase detector time response, another set of data was taken without the low pass output filter. The results are shown in Fig. 20. The rf output signals due to the acousto-optic beam, the direct beam and both beams together are shown in Figs. 20(a) through 20(c). While the direct beam shows significant rf output, its spectrum is generally higher in frequency than the photomixing signal. Some consideration was given to the possibility of using a band-pass filter centered at 150 MHz to improve the S/N of the heterodyne output signal, but the nonrepetitive nature of the laser precluded short term (tuning) adjustment of such a filter without large expenditure of time. The unfiltered phase detector outputs for the three cases are shown in Figs. 20(d) through 20(f). Again, the stronger direct beam shows the largest spurious output levels. The

RF OUTPUT



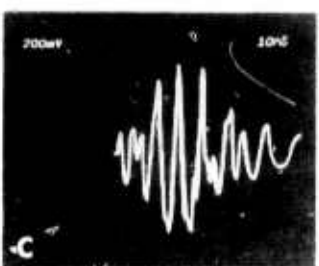
3491-24

ACOUSTO-OPTIC BEAM $\approx 4 \times 10^{-8} \text{W}$



3491-25

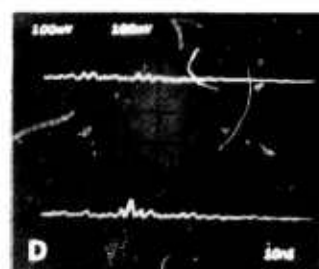
DIRECT BEAM $\approx 1.2 \times 10^{-7} \text{W}$



3491-26

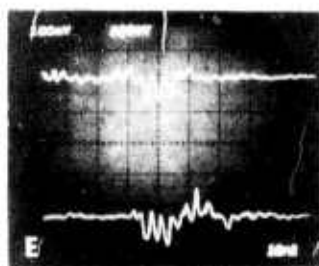
BOTH BEAMS

PHASE DETECTOR OUTPUT UNFILTERED



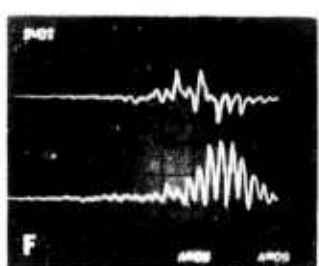
3491-27

ACOUSTO OPTIC BEAM



3491-28

DIRECT BEAM



3491-29

BOTH BEAMS

Figure 20. Unfiltered phase detector output and error signals due to pulse spectrum.

pulse envelope here is of interest rather than the modulation within the envelope which is filterable. The conclusion drawn here is that the phase detector output filter did not significantly distort the time shape of the pulses when the envelope responses of both cases are compared. The need for band-pass filtering of the heterodyne output signals is clearly indicated as a way of reducing the spurious phase detector output because the synchronous phase detector can yield output signals at harmonics of the reference signal which can appear in the noise spectrum of the heterodyne signal. Such filters are best tested with a repetitive laser system which will be available for the field experiment.

The next set of measurements made in this series were the preliminary low level measurements. Here the power was reduced by a factor of 5 on the direct beam and a factor of 10 on the acousto-optic beam. This was accomplished by rotating one of the glan prisms in the laser attenuator and the $\lambda/2$ waveplate shown in the system diagram. The first series (Figs. 21(a) through 21(c)) shows the photomultiplier video output for the direct beam, the acousto-optic beam and both beams together. At these signal levels quantum noise effects are very evident as is rf pickup. In the absence of the laser signal the rf leakage signals at the photomultiplier output appear to be equivalent to an optical noise power of 10^{-9} W. This prevented further testing at lower optical power levels. This noise level is traceable to the rf power amplifier which drives the acousto-optic modulator and it disappears when the rf oscillator is turned off. Figures 21(d) through 21(f) show the three cases after rf amplification and 100 MHz high pass filtering. The leakage signal is shown in Fig. 21(g). The rf leakage signal is more evident because of the amplification and filtering but the heterodyne output signal is significantly different than that from either beam alone. The filtered phase detector output signals are displayed in Figs. 21(h) and 21(i). These results are comparable to those taken earlier at higher power levels. The rf leakage did not affect the results since it contributes only to the dc level of the phase detector output.

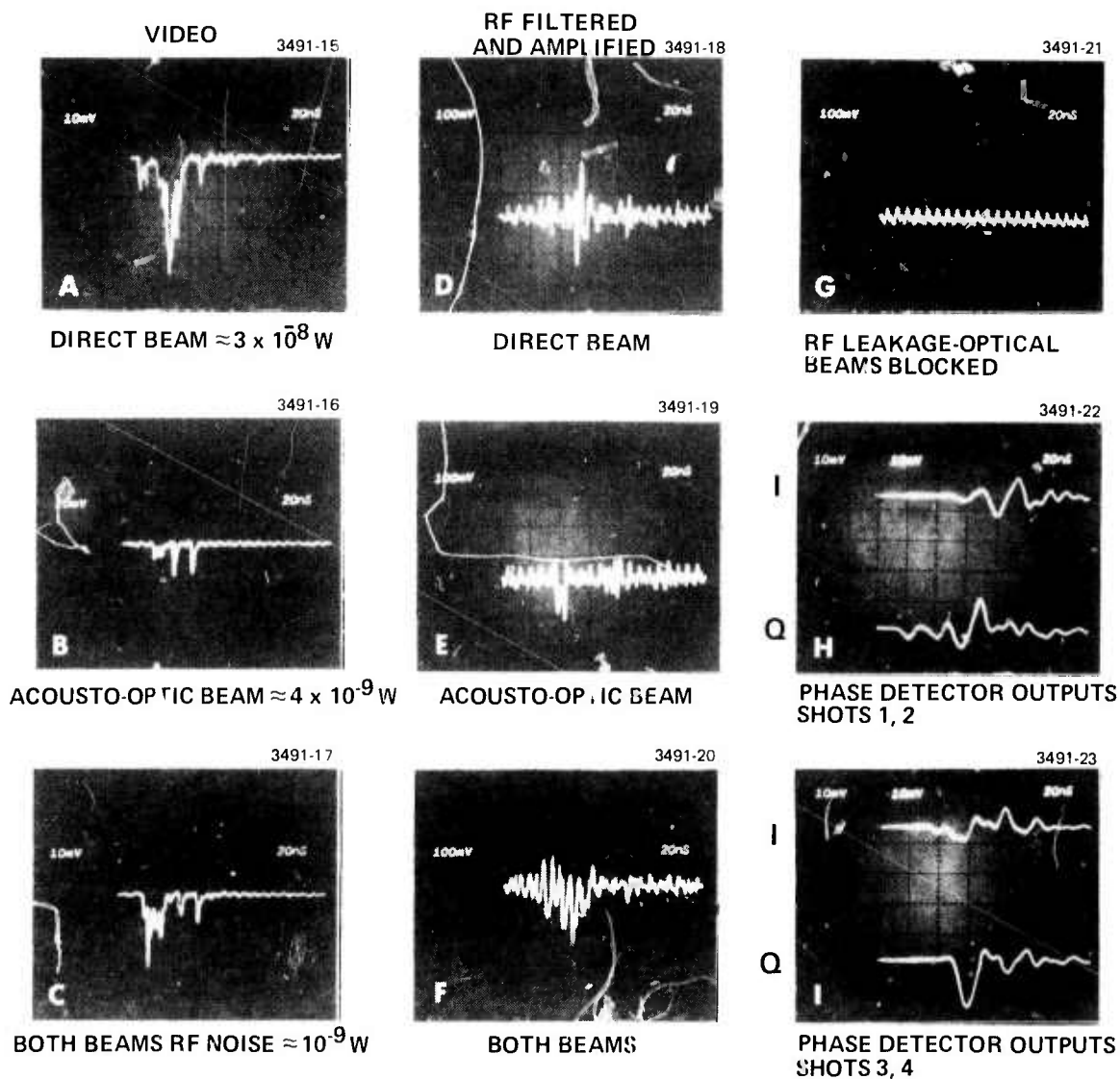


Figure 21. Preliminary low level measurements.

I. Comparative Testing of RCA C31024A Photomultiplier

Some of the results obtained during the PRIM5 simulation experiment indicated the existence of spurious signals at the photomultiplier output. The principal concern was whether or not the tube could oscillate due to improper electrical circuitry or whether optical phenomena gave rise to these effects. The finding of this set of tests was that both effects can occur and that care and feeding of the tube is critical but straightforward. The details of these tests are given in Appendix G.

The conclusions drawn from this series of photomultiplier time response tests are as follows:

- (1) Best overall fidelity of response was obtained from the RCA C31024A PMT biased with an AT2219 fast rise network
- (2) Multipath propagation effects in the laboratory gave rise to some of the anomalies observed earlier
- (3) Tube response depends critically on output impedance match and satisfactory impedance matches have been made to a wide band amplifier which acts as an isolator from the phase detector in addition to increasing the signal level.
- (4) A wider bandwidth amplifier used earlier in the program has proven to be poorly impedance matched to the PMT and has been eliminated from use.
- (5) Attenuation of the optical signal by a factor of 3 from the 21 dB signal to noise ratio shown in Figure A introduces apparent ringing which is attributed to quantum noise effects and not photodetector anomalies.
- (6) The photomultiplier performance should be adequate for the proposed experiment option.

J. Fiber Optic Delay Line Development

1. Pulse Tests

The method for multiplexing the optical signals in the PRIMS field experiment is based on 10 sets of fiber optic delay lines with a delay differential of 60 nsec between each of the 10 members of one set. To test the feasibility of this concept we purchased 10 multimode glass fibers with delays of 60, 120 ----- 600 nsec ± 1 nsec from Corning Glass. The fibers were delivered on a cylindrical form and an apparatus for combining the common inputs and outputs was fabricated and shown in Fig. 22. Since these fibers are somewhat fragile, they are partially unreeling and assembled, as shown in Fig. 23 instead of being respooled on individual forms. This approach offered the minimum risk of breakage.

After preliminary measurements of delay time and attenuation had been made it was decided that cladding mode propagation affected the signal transmission and cladding mode suppressors made of black velvet impregnated with glycerin were used in the system with significant improvement. One of these suppressors is shown unassembled on the left (in Fig. 23) which is the signal input. The fibers pass through foam rubber clamps on either side of the mode suppressor and then are gathered into a small diameter ferrule to align the fibers to a parallelism less than 1° . The mode suppressor operates on the principle that an index matching fluid permits energy launched into the cladding to leak off and the black velvet acts as an absorber to prevent cross coupling between fibers. Ultimately it was necessary to use mode suppression devices at the input and the output ends of the delay lines in order to obtain reasonably uniform transmission characteristics for the fibers.

Initial pulse testing of the optical fibers was performed with a multimode repetitive laser. The repetitive nature of the laser permitted the position and angle of the expanded recollimated optical

M10577

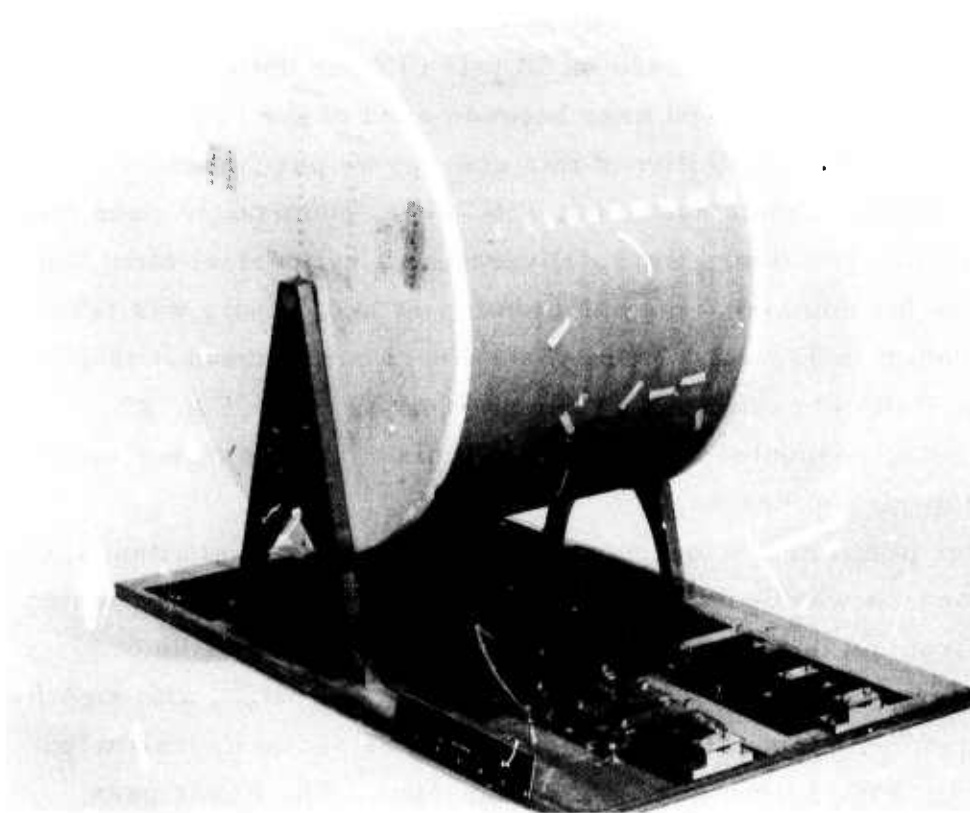


Figure 22. Ten element fiber optic delay line system with mode suppression on input and output.

M10578

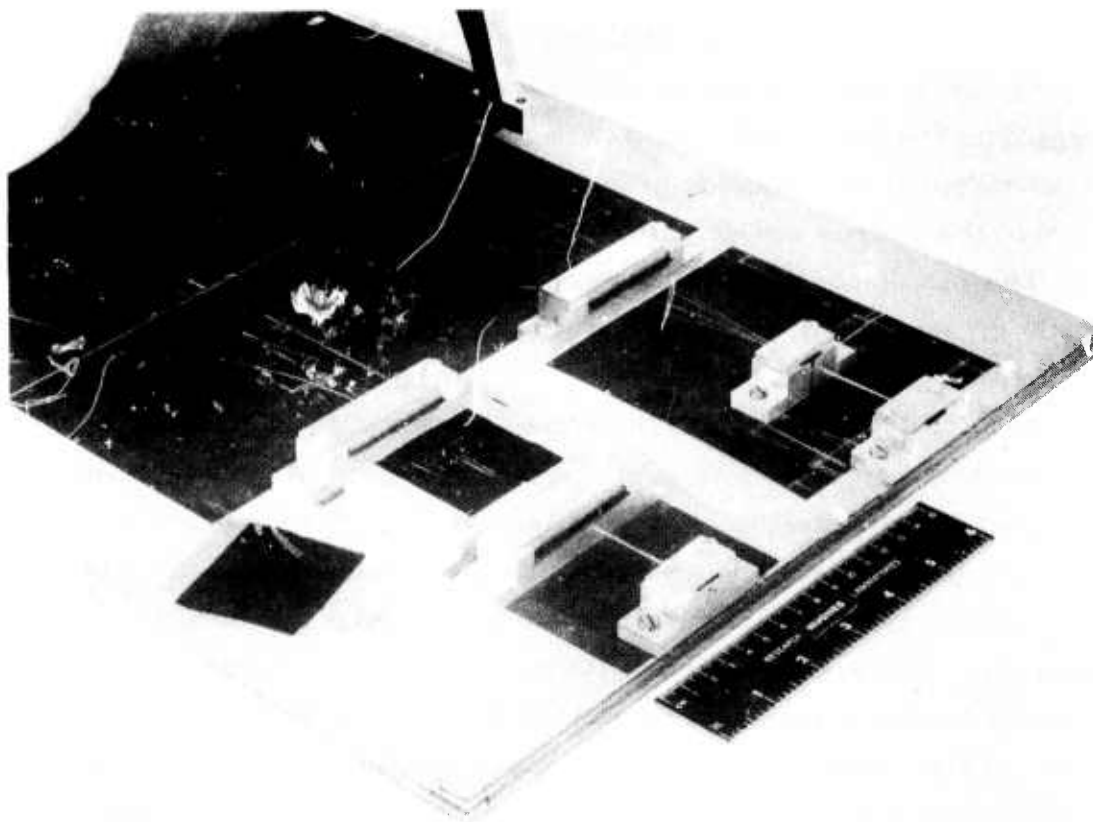


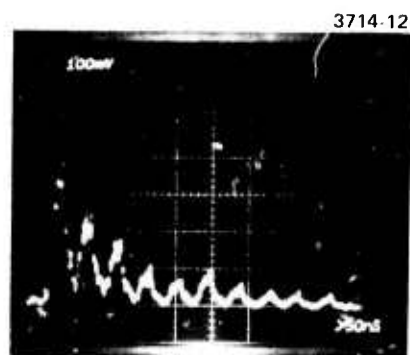
Figure 23. Details of cladding mode suppressor.

beam to be adjusted while visually observing the delayed pulses. The multimode nature of the laser simulated the multiple frequency nature of the expected target return and thus permitted an evaluation of fiber delay line dispersion. Because of an expected lack of optical field uniformity at the fiber input and a lack of photocathode uniformity at the fiber output it was planned to move the input and output bundles relative to the source and detector and average the data.

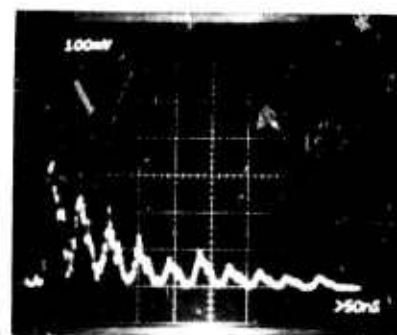
The results of this process are shown in Fig. 24. Figure 24(a) and 24(b) display two different laser pulses with the apparatus in the same position. Similar data at other arbitrary positions appear in Figs. 24(c), (d), (e), and (f). The shorter delay signals were stronger than those with longer delays, and the pulses were all resolvable indicating tolerable dispersion error. When data taken in this manner was plotted with pulse amplitude as a function of time delay on semilogarithmic paper, the slope of the data points did not correspond to a straight line. In fact two straight lines, one for the shorter delays and one for the longer delays, corresponded to a best fit as shown in Fig. 25. This result indicated that the energy launched into the cladding modes had higher attenuation than the core attenuation. This caused anomalously high transmission for the shorter delays. A tabulation of several sets of data extrapolated for the maximum delay time, 600 nsec, is shown below.

<u>Initial Slope</u>	<u>Final Slope</u>
12.8 dB total	3.62 dB total
8.58 dB total	4.38 dB total
11.2 dB total	4.9 dB total
11.0 dB total	4.58 dB total

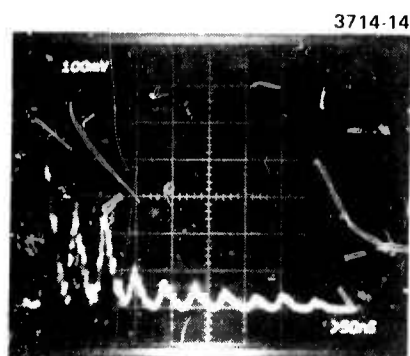
The average of all the data was 10.24 dB for the initial slope and 4.28 dB for the final slope corresponding to 93 dB/km for the initial slope and 39 dB/km for the final slope over a path length of 0.11 km.



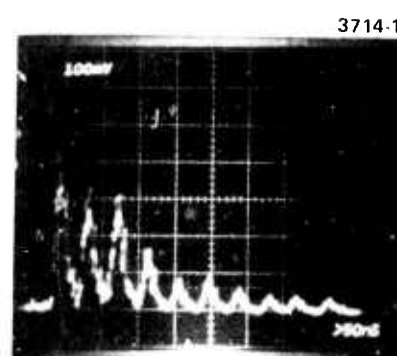
(a) POSITION 1
SHOT 1



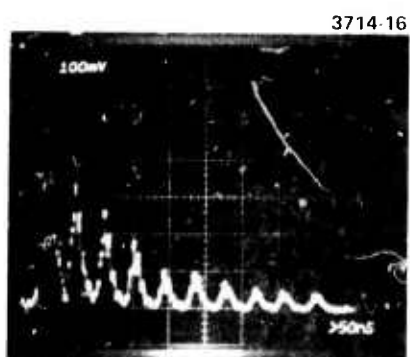
(b) POSITION 1
SHOT 2



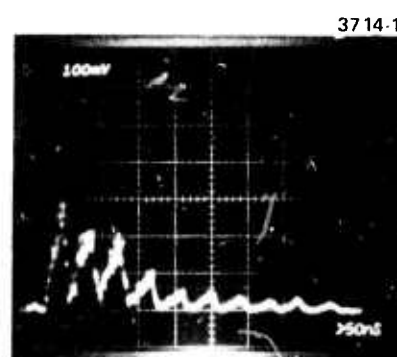
(c) POSITION 2
SHOT 1



(d) POSITION 2
SHOT 2



(e) POSITION 3
SHOT 1



(f) POSITION 3
SHOT 2

Figure 24. Anomalous pulse attenuation due to cladding mode propagation.

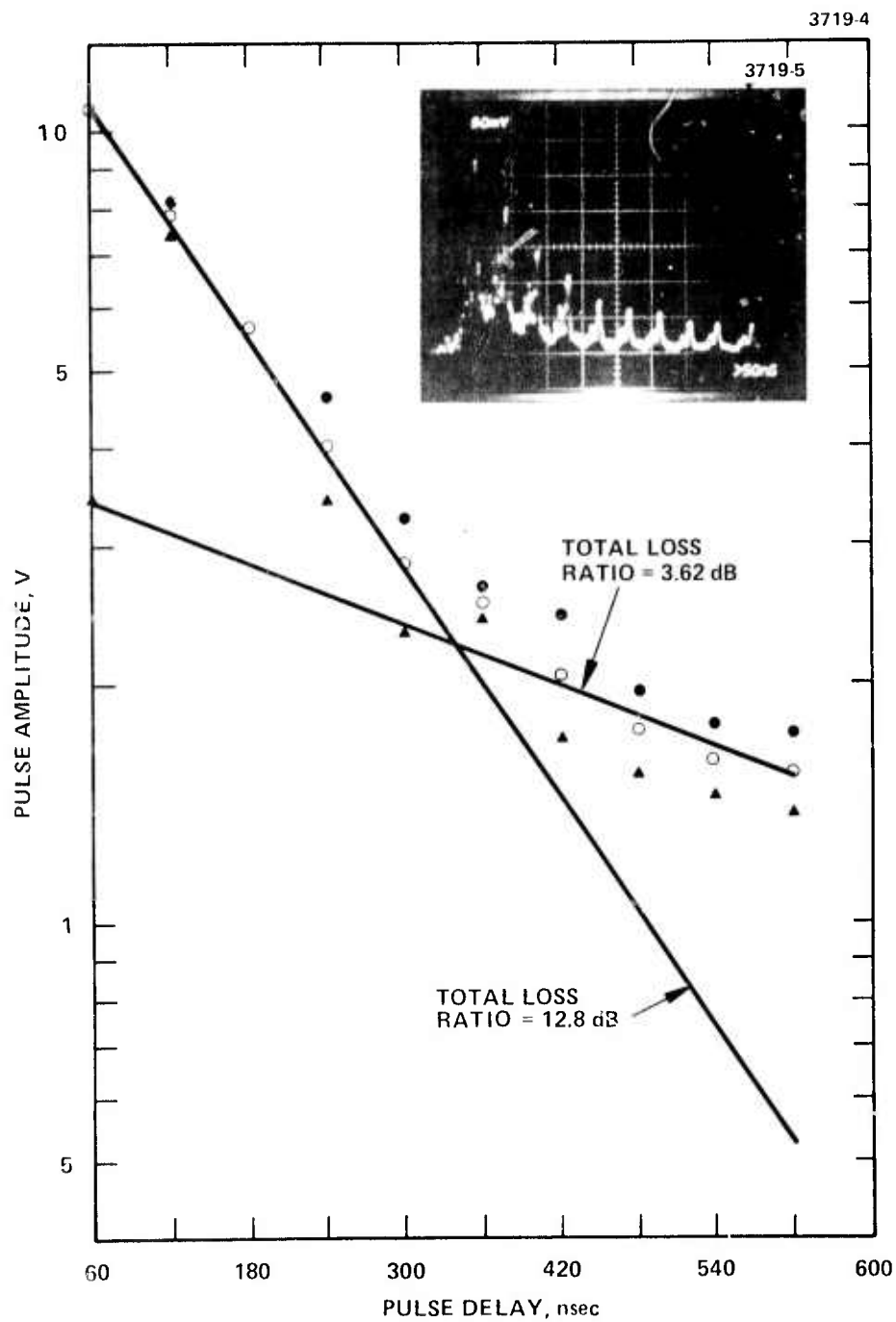


Figure 25. Pulse amplitude versus delay time without cladding mode suppression.

Since these losses were a factor of 4 larger than expected, a set of cladding mode suppressors was fabricated and one was installed on the input end of the delay line. Partial improvement was noted and a second mode suppressor was installed on the output end. The overall time response obtained with mode suppression on both fiber optic delay line input and output is illustrated in Fig. 26. Figures 26(a) and 26(b) are taken with input and output geometry fixed. Either thermal expansion or thermal mode change in the laser can cause the illumination to vary from shot to shot. Figures 26(c), (d), (e), and (f) were taken with a different input and output position and the gain was increased in Fig. 26(e) and (f) to show fine structure. Overall attenuation data averaged for multiple shots at each position yielded total attenuation of 4.7 dB, 2.25 dB, and 3.2 dB (see Fig. 27) with an average value of 3.4 dB or 31 dB/km. By studying the pulse amplitudes at each delay position we found that with the exclusion of delay No. 9 the ratio of maximum to minimum signal amplitude was a factor of 2 (3 dB). The total attenuation of the fiber measured by Corning was 4.6 dB over 700 m length (~6.6 dB/km) and it should therefore be 0.7 dB for the longest delay (0.11 km). This did not compare favorably with our average loss of 3.2 dB and a series of cw measurements was started with the goal of evaluating the fiber core propagation loss. The experiments are described in Appendix H. The results of these experiments tend to substantiate the theory that excitation of cladding mode propagation at the shorter delays adversely influences the attenuation measurements and that the mode stripping devices have not been made long enough to completely eliminate these effects. In the experiment option the optical fibers are to have the cladding stripped from the input ends to provide the highest density of packing. Thus the cladding modes would not be excited by the target signals and the need for mode strippers may cease to exist. Our successful efforts at cladding removal are reported in Appendix I.

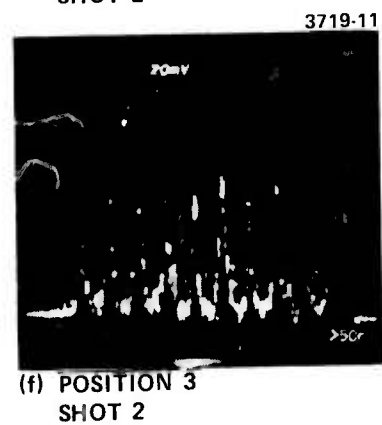
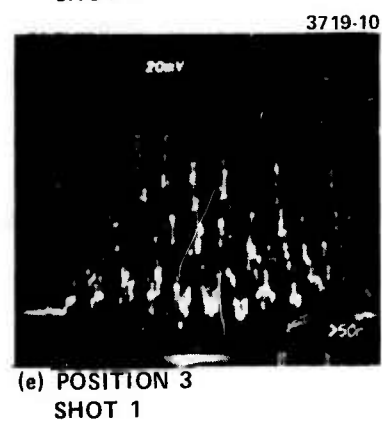
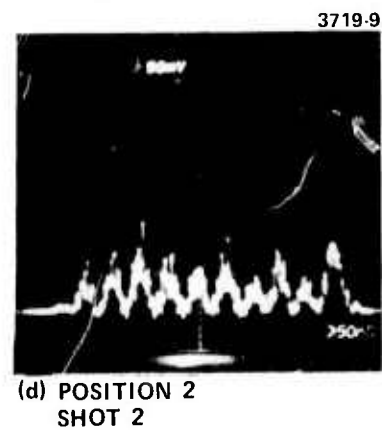
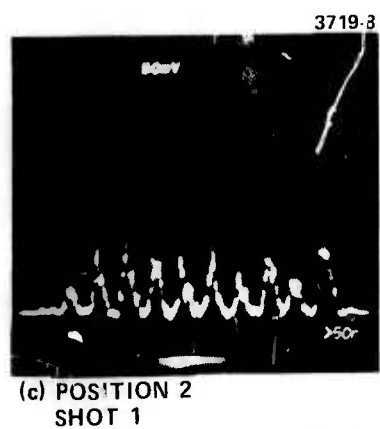
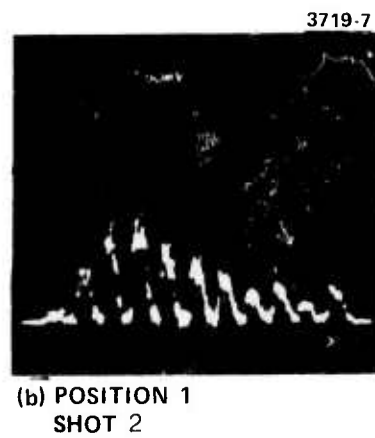
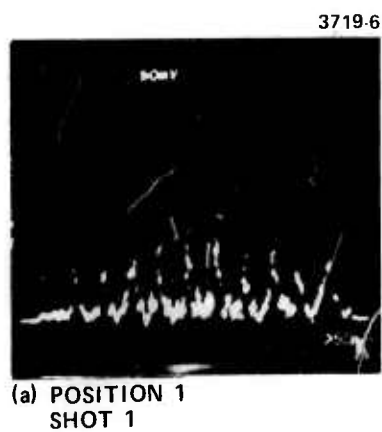


Figure 26. Fiber optic response to multimode laser pulse.

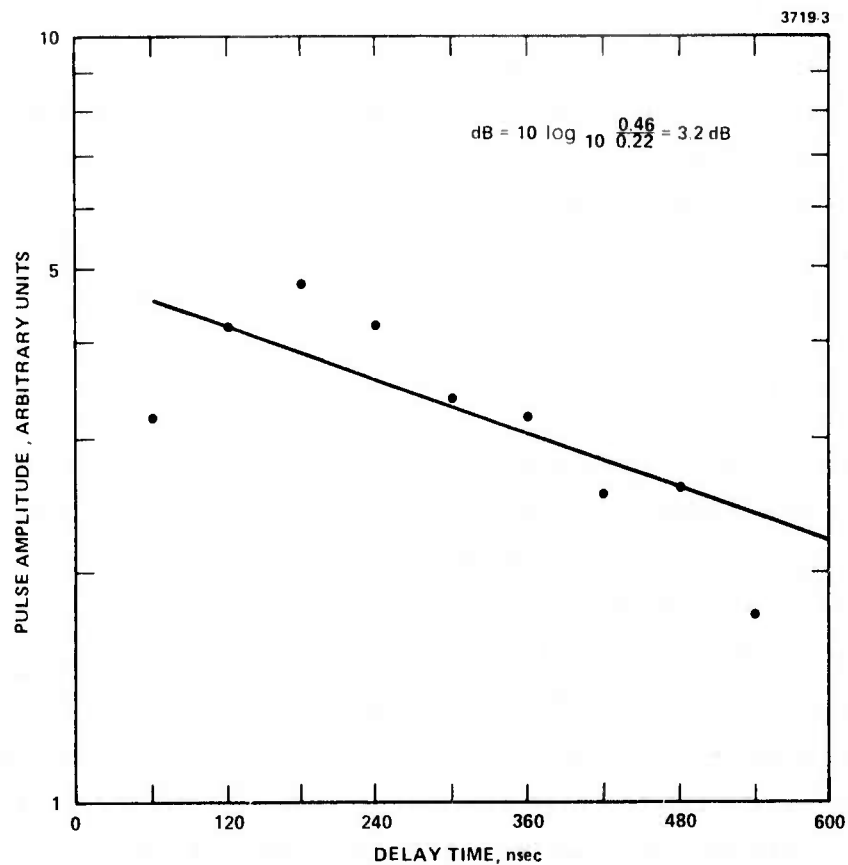


Figure 27. Pulse amplitude versus delay time with partial cladding mode suppression.

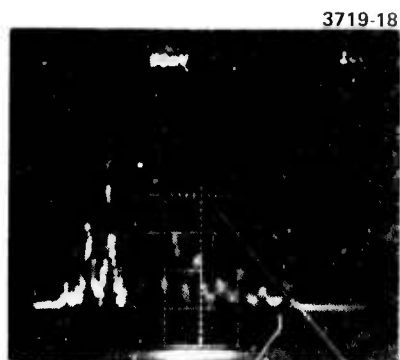
The fiber optic delay times were checked by taking a series of photographs of the entire trace with a selected portion intensified and then displaying on an expanded scale the intensified pulses. Figures 28 and 29 show the intensified and expanded portions, and the pulse peaks are separated by 60 nsec within 2 nsec. This pulse delay accuracy is sufficient for this application because the data sampling intervals will be of the order of 15 nsec or 4 per pulse so the main concern here is cumulative error which is quite tolerable.

K. Signal Processing Study

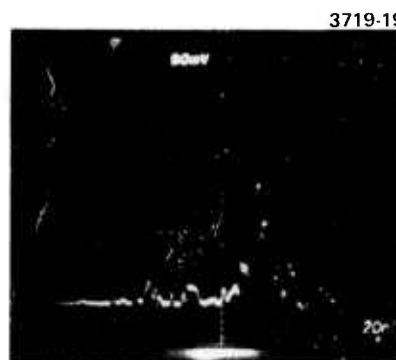
The time delay multiplex PRIMS system will consist of 10 fiber optic delay lines feeding each of 10 photomultiplier tubes followed by 10 phase detectors yielding I and Q information on the relative phases of the optical and reference signals. Specifically this yields 20 output pulses from each phase detector, with 10 from the I channel and 10 from the Q channel. From these 20 I and Q channels 200 30 nsec pulses will be produced in 1200 nsec. This corresponds to 166×10^6 pulses per second, a rate far too high to be recorded with off the shelf technology. Consultation with several groups at Hughes has led to the concept of using 20 fast analog to digital encoders to sample each of the channels every 15 nsec. The data is then stored in random access memory units which can be interfaced with a tape recorder to sequentially dump the data. The data processing requirements are listed in Table 6.

Several circuit approaches exist for the solution of this problem, but they differ mainly in the type of components used for the sampling function and the memory. The maximum available quantization for this task is 6 bits (5 bits + sign) but computer simulation studies indicate that 4 bit quantization may be adequate.

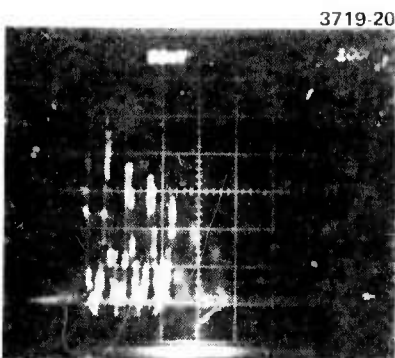
Figure 30 proposed PRIMS digital data recording system. The area enclosed by a dashed block represents the complete processing system for one photomultiplier output channel (i. f. input No. 1). The



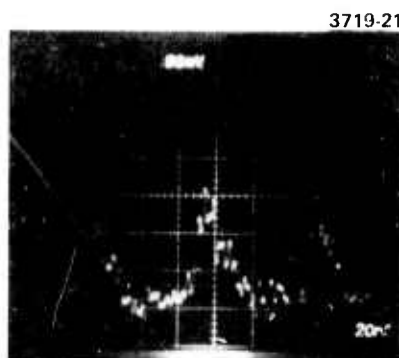
(a) PULSE 1 AND 2
INTENSIFIED



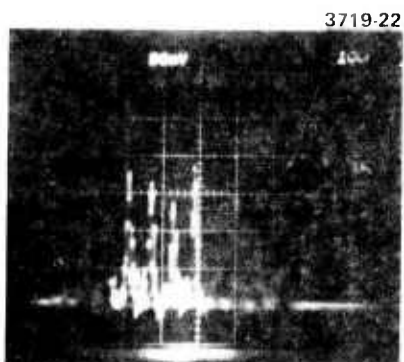
(b) PULSE 1 AND 2
DISPLAYED



(c) PULSE 2, 3, AND 4
INTENSIFIED



(d) PULSE 2, 3, AND 4
DISPLAYED



(e) PULSE 4, 5, AND 6
INTENSIFIED



(f) PULSE 4, 5, AND 6
DISPLAYED

Figure 28. Interpulse delay data.

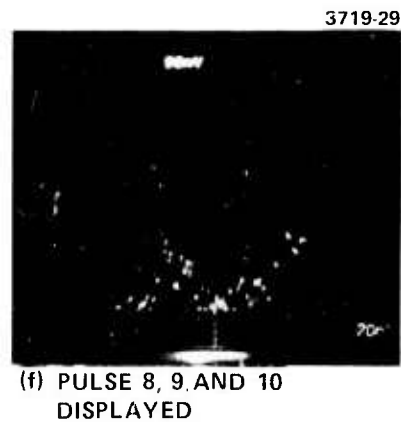
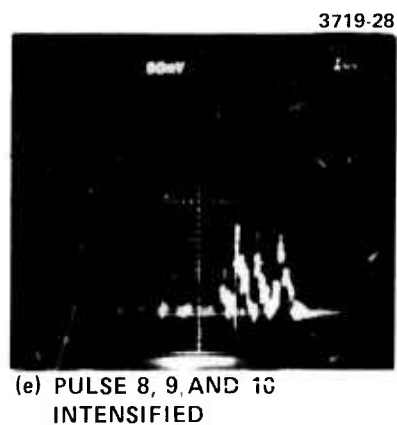
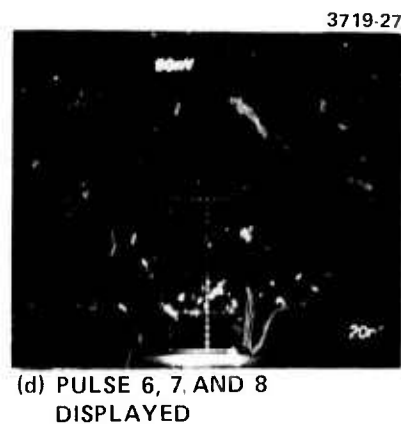
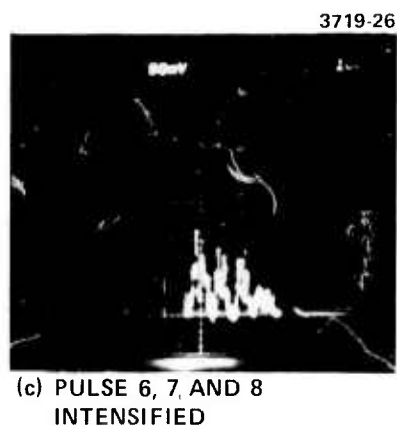
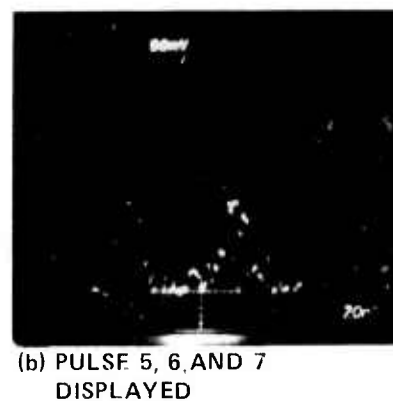
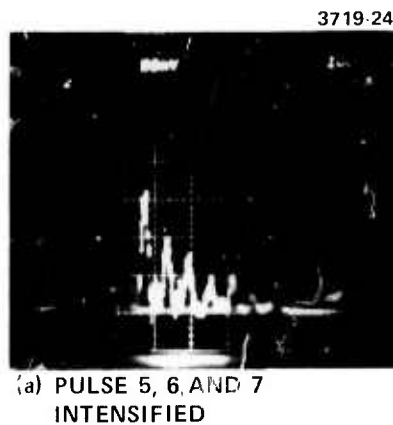


Figure 29. Interpulse delay data.

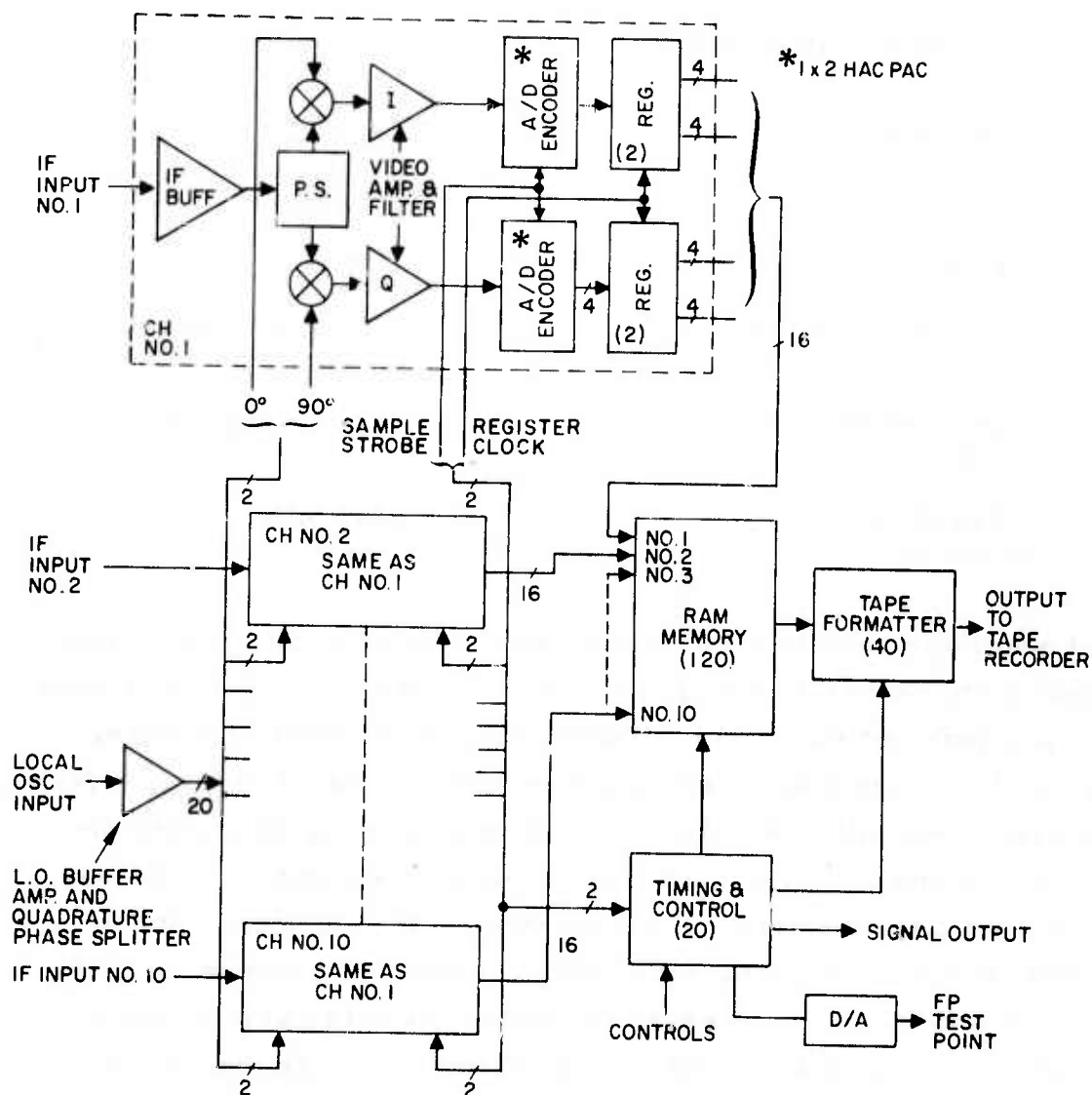


Figure 30. PRIMS digital data recorder.

Table 6. Data Recording - PRIMS 100 Element System

Number of Input Channels	20
Number of Pulses Per Channel	10
Inter Pulse Delay	120 nsec (1200 nsec total duration)
Sampling Interval	15 nsec
Basic Requirement	80 words 15 nsec sample rate
Quantization 4, 5 or 6 Bits	(3 bits + sign, etc.)
RAM Memory	6400 bits

local oscillator input is the coherent radio frequency reference signal channel common to all of the phase detection circuitry. In this system the i. f. inputs and the local oscillator occur at the same frequency. The i. f. input signal is buffered, power split and mixed with the reference signal and with a 90° phase shifted reference signal to yield the I and Q components. The I and Q components are sampled in the fast analog-to-digital counters and passed through the registers, which provide the time sequencing information, prior to storage in the RAM units. A timing and control system strobes the data and provides the sequential readout process via the tape formation. The digital circuitry developers feel that the best approach is the inclusion of rf processing and sampling in a single package to avoid interfacing problems and pickup effects.

L. Summary and Conclusions

The results presented in the earlier sections of this report on the PRIMS experimental design lead to the conclusion that all of the elements of a PRIMS optoelectronic system have been laboratory tested and that a complete system is feasible.

Feasibility of the PRIMS transmitter scheme was demonstrated using single, short duration (20 to 30 nsec) optical pulses that were:

- a. Split into two orthogonal polarizations.
- b. One polarization frequency shifted by 150 MHz via a pulsed acousto-optic modulator.
- c. Recombined to a single beam.

Feasibility of the PRIMS receiver scheme was demonstrated for short duration optical pulses by:

- a. Heterodyne detection and phase synchronous detection of the PRIMS transmitter pulses.
- b. Demonstration of time division multiplexing using a ten element fiber optic delay line.

IV. AMOS LASER MODIFICATIONS

One of the requirements for the success of PRIMS is that the laser illuminator be temporally coherent. This is required because of coherence length considerations (i. e., the coherence length must be twice the target depth to be resolved). The primary goal of this task is to modify the AMOS ruby laser which operates in many longitudinal modes (many frequencies) so that it can be made to operate Q-switched in a single longitudinal mode without appreciable degradation of total energy output.

A. Experimental Approach

The experimental approach taken toward achieving this goal was to employ a bleachable dye Q-switch alone or in combination with the Pockels cell that is presently employed for Q-switching the AMOS laser and a resonant reflector or intracavity tilted etalon to serve as longitudinal mode selecting elements.

B. Experimental Tools

The experimental tools that were used to monitor the longitudinal mode characteristics of the laser are a fast photodetector and oscilloscope (for monitoring frequency components up to 1 GHz) combined with a Fabry-Perot interferometer (for monitoring, frequency components greater than 1 GHz). The detector used is a biplanar photodiode, the oscilloscope, a Tektronix 519. Two different Fabry-Perot interferometers were used in the experiments, one of them having a free spectral range of 10 GHz and the other, 48 GHz. Using these tools the desired single longitudinal mode laser performance would be characterized by a temporally smooth pulse (i. e., no modulation) as viewed on the oscilloscope trace and a Fabry-Perot interferogram showing a single frequency component.

C. Experimental Setup

The AMOS ruby laser along with the additional Hughes modifications and monitoring apparatus are shown in Fig. 31. The ruby oscillator resonant cavity is formed by mirror M1 and the sapphire etalon output reflector. The elements in Fig. 31 that are represented in dashed line format are those

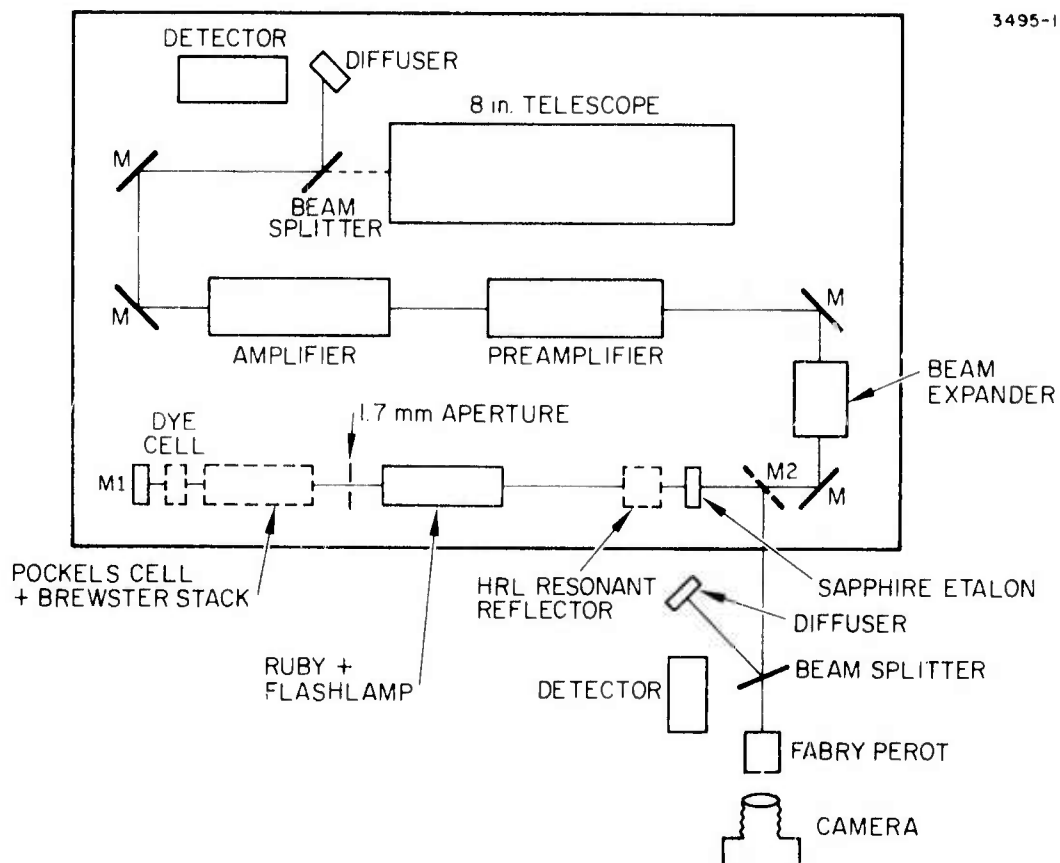


Figure 31. AMOS ruby laser experimental setup.

that were taken in and out of the optical cavity to vary the operating conditions during the course of the experiments. Light from the oscillator was coupled to the monitoring apparatus by means of mirror M2, and subsequently divided between the fast detector and Fabry-Perot interferometer.

D. Experimental Results

Prior to any attempt at modifying the AMOS laser several measurements were made in which the longitudinal mode performance of the oscillator was monitored. Sample results of these measurements are shown in Fig. 32 in which we see oscilloscope traces and Fabry-Perot interferograms for a sequence of laser shots. These data represent the shot-to-shot reproducibility of the unmodified laser's spectral/temporal behavior and one can readily see that the longitudinal mode content changes rather drastically from shot-to-shot even though the laser was not disturbed during the series of measurements and the operating conditions were kept constant.

After the initial oscillator characterization measurements were carried out, a systematic series of experiments was performed in which the following parameters were varied while monitoring performance:

- Q-switch dye* concentration.
- Operation with and without Pockels cell.
- Operation with and without Hughes resonant reflector**.
- Alignment of resonant reflector with sapphire etalon.
- Alignment of one of the faces of the ruby rod (7 min wedge) with different elements in the cavity.
- Temperature of cooling water used to cool ruby rod.
- Pump lamp voltage.
- Length of oscillator cavity.

*Dyes used were cryptocyanine in methanol and 3,3'-diethyl-6,6',-dinitrothiadicyanocyanine iodide (D-I) in methanol. D-I is a dye synthesized at HRL and found to have excellent resistance to photodegradation.

**This is a resonant reflector designed at HRL consisting of two quartz etalons of different thicknesses designed to enhance longitudinal modes that are separated by $\sim 2 \text{ cm}^{-1}$.

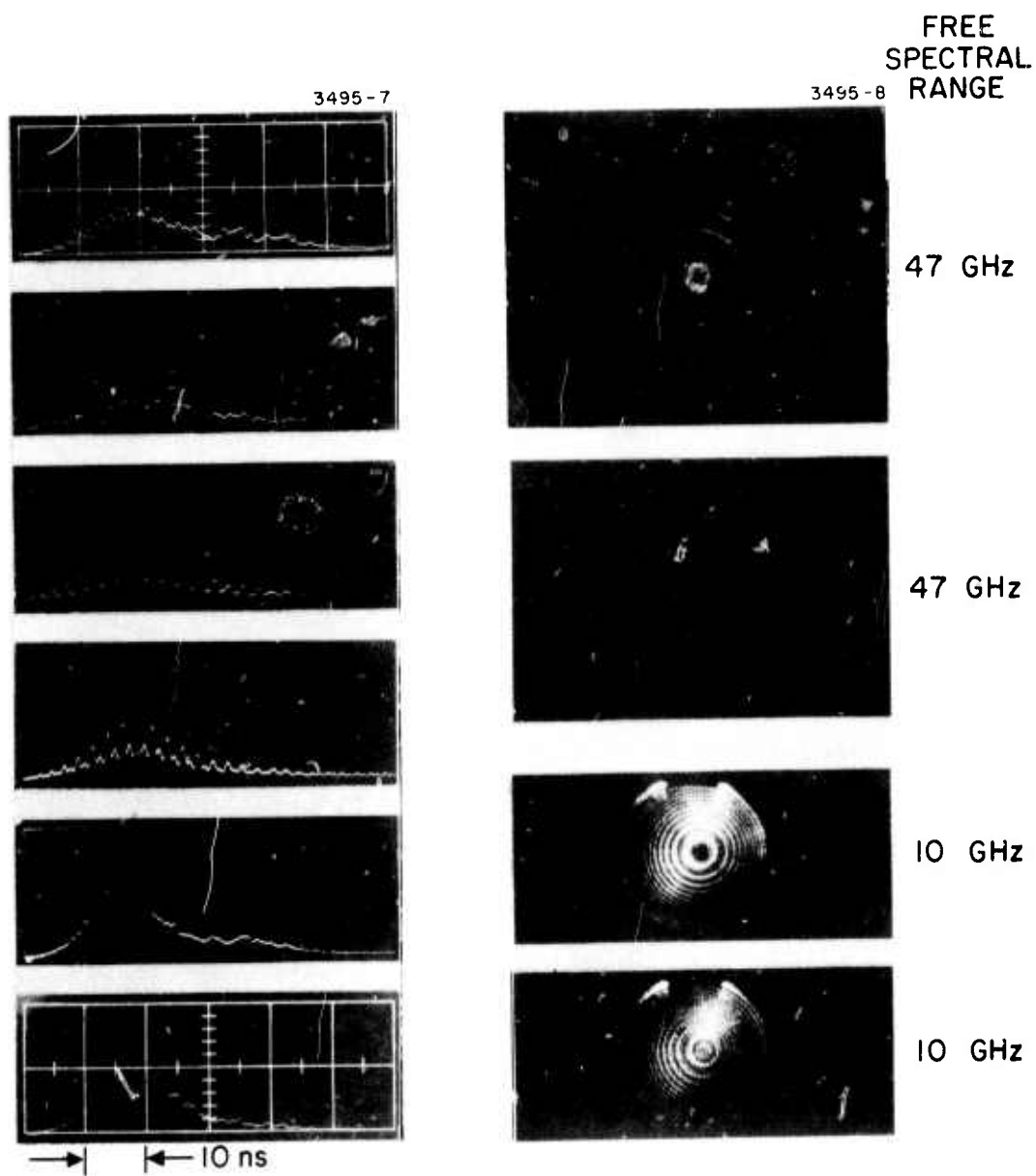


Figure 32. AMOS oscillator performance prior to modifications.

Because of time limitations at AMOS it was not possible to vary the operational parameters exhaustively, but it was possible to zero in on satisfactory single longitudinal mode operation over a range of operating conditions. Figure 33 shows oscillograms and Fabry-Perot interferograms of the modified oscillator performance. Here we see smooth temporal profiles for the laser pulses and a single frequency component in the interferograms, the combination of which indicates single longitudinal mode performance and temporal coherence over the entire pulse.

Figure 34 shows the result of repetitive pulsing of the oscillator at 20 ppm. Samples of the output pulses were taken for two different runs, one of 2.5 min and another of 5 min. Good pulse reproducibility is evident in the oscilloscope pictures of Fig. 34. It was important to check repetitive pulse performance of the oscillator because there was some uncertainty prior to these experiments whether or not there might be a thermal problem with the Q-switch dye under multiple pulse operation that would require circulation of the dye solution. There appears to be no such problem since the static dye solution functions satisfactorily under multiple Q-switch operation.

Finally, the performance of the whole system was monitored on a single shot basis. Figure 35 shows the temporal profile of a sequence of pulses through the amplifiers when the oscillator was operated in the unmodified configuration. Again as in Fig. 32, multilongitudinal mode operation is evident as indicated by the irregular pulse temporal profile. Performance for the modified system is shown in Fig. 36. Here for comparison we show an oscilloscope photograph for the oscillator pulse alone compared to traces of three different amplified pulses. The significant feature for comparison is the presence of a shoulder on the trailing edge of the amplified pulses. It is believed that this shoulder results from a reflection of the amplified pulse somewhere in the system, causing a portion of the pulse to double pass the amplifiers and result in a broadening along the trailing edge. From the approximate separation between the pulse peak and the shoulder (~ 12 nsec) one obtains a one way optical path for the reflected pulse of about 6 ft which is close to the distance from the end of the second amplifier output face to the oscillator output reflector. If in fact the shoulder on the amplified pulse does result from a reflection external to the

3495-5

3495-6

FREE SPECTRAL
RANGE, 10 GHz

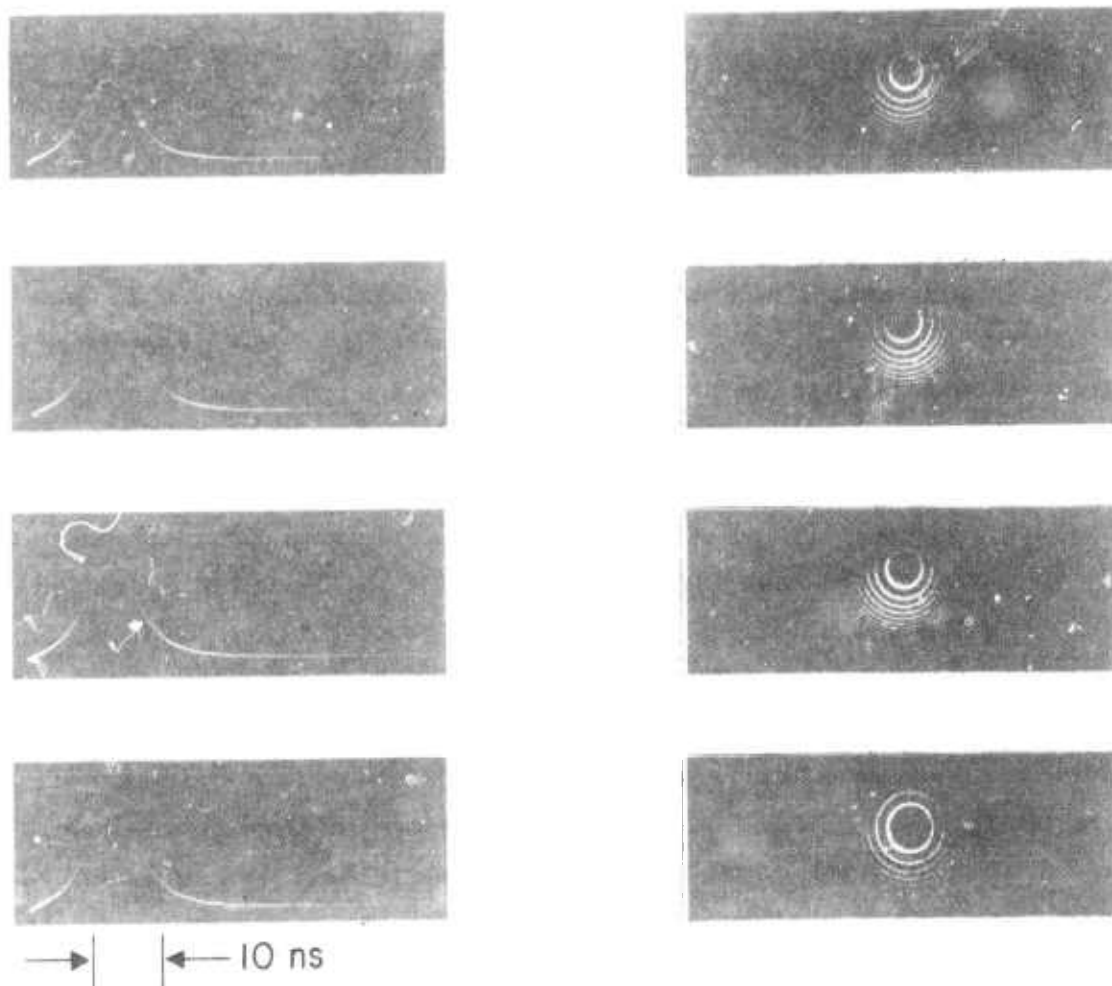


Figure 33. Modified oscillator performance.

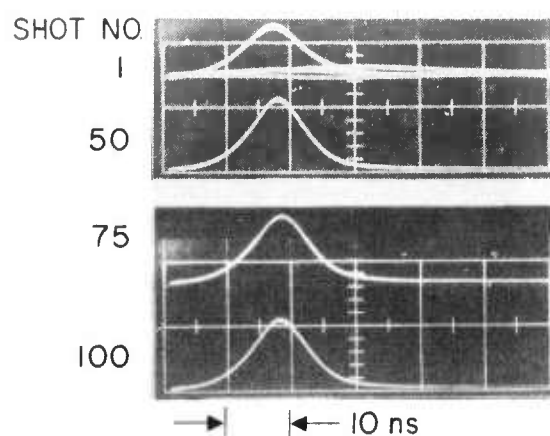
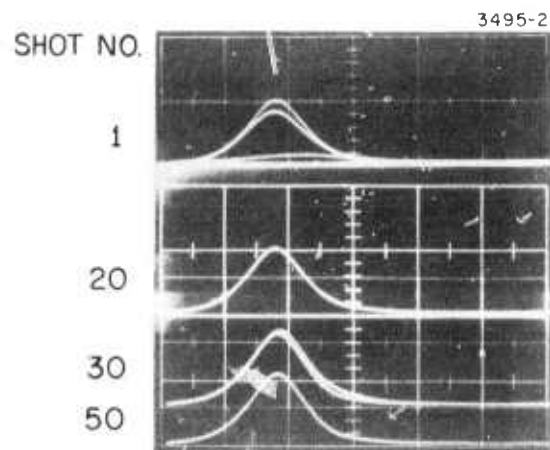


Figure 34. Oscillator performance at 20 ppm.

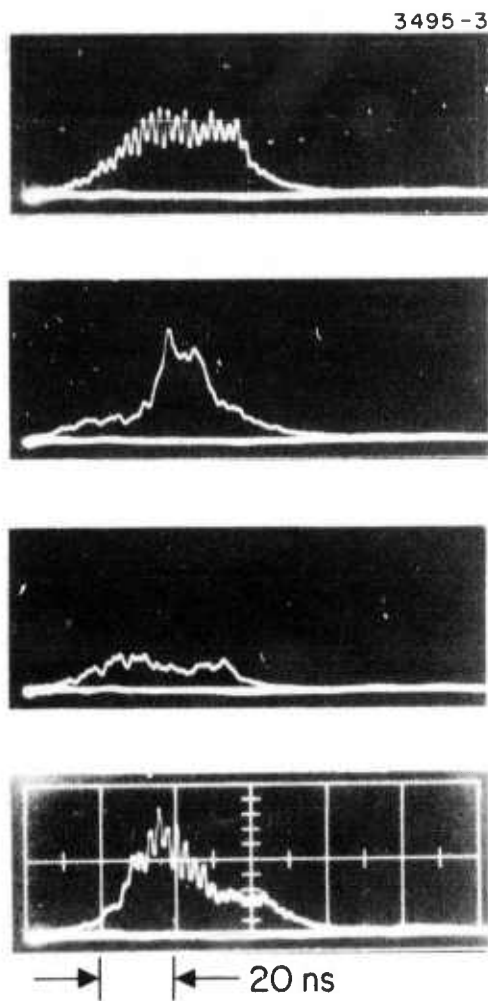
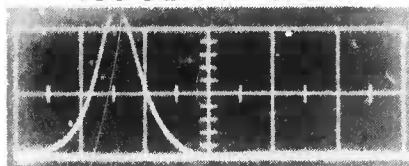


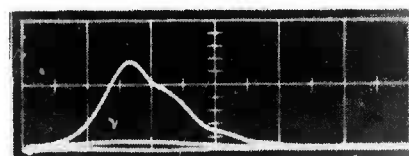
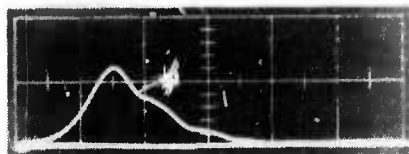
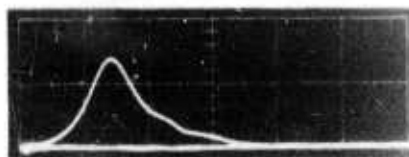
Figure 35. Multimode pulses through amplifiers.

3495-4

OSCILLATOR ONLY



OSCILLATOR
PLUS AMPLIFIERS



→ | | ← 20 ns

Figure 36. Single mode
pulses through
amplifiers.

oscillator as suspected, it will in no way change the suitability of the system for PRIMS with respect to single frequency performance.

Total energy output from the system was measured for both single and multilongitudinal mode operation and was found to be comparable for both cases under the same operating conditions (4-5J). Although this is somewhat less than the Q-switched output energy reported for the AMOS laser (7-10 J) it is satisfactory for the purpose of a PRIMS demonstration experiment.

E. Operating Parameters in Need of Optimization

Although single longitudinal mode operation was successfully demonstrated for the AMOS ruby laser system, there are several operating parameters that should be optimized so that the system may operate under more relaxed conditions. Among the more important of these parameters are:

- Operating temperature
- Alignment stability
- Ruby rod parallelism and optical flatness
- Lamp pump pulse shape.

The operating temperature is important because the spectral width of the ruby fluorescence line is strongly temperature dependent being narrower at low temperatures. Hence, the lower the operating temperature the easier to obtain single frequency operation. It has been our experience that the difference between 0°C and 5°C operating temperature means a difference between 99% reliability and about 70% to 80% reliability, everything else being equal. Because of condensation problems on the ruby rod faces at AMOS it was not possible to operate the laser at temperatures lower than 38°F (~3°C) and even then only on dry days. Operating at higher temperatures means that other parameters (i.e., mechanical stability, alignment) must be more stringently maintained in order to optimize intracavity frequency selection.*

*Greater gain bandwidth means greater tendency for multifrequency operation and more mode selection is required to obtain a single longitudinal mode. One way this is accomplished is by interferometrically aligning all the optical surfaces in the cavity the reflections from which enhance the frequency selectivity.

Hughes has successfully operated a single longitudinal and transverse mode ruby laser oscillator quite reproducibly without using any reflective mode selecting elements except the cavity mirrors themselves. This was accomplished by the proper choice of dye Q-switch, high optical quality ruby, low operating temperature (0°C), and optical pumping scheme (see below). It should be a fairly straightforward matter to modify the AMOS laser for operation at 0°C . This could be accomplished by blowing dry nitrogen over the ends of the ruby rods (or enclosing the laser and amplifier heads in boxes with dry gas flowing through) and by mixing an appropriate amount of antifreeze (ethylene glycol) with the cooling water.

Another operating parameter that should be optimized is the shape of the electrical flash lamp pump pulse. There is a tendency for the AMOS oscillator to give more than one pulse when dye Q-switched unless the flash-lamp pump voltage is very carefully controlled. It is believed that this behavior is caused by the shape of the electrical pulse (a fast rising pulse with a long tail about 2 msec in duration) that pumps the oscillator flashlamp. The optical pumping that occurs during the long tail tends to cause after pulsing for dye Q-switch operation. The ideal shape for such a pump pulse is a square wave with variable duration. The length and height of the square wave pump pulse is adjusted so that the laser switches on just when the pump pulse is turning off. This is not only a more efficient way of operating such a system but also it eliminates the after pulsing problem.

The recommended pump pulse modification for the AMOS system (applicable to the amplifier lamps as well) involves modifying the capacitive discharge storage bank with the appropriate inductances to form a transmission line whose impedance matches that of the flashlamp.

V. PRIM COMPUTER SIMULATION

A. Introduction

The PRIM computer simulation studies were undertaken with a two-fold objective: to determine the characteristics of the PRIM concept relative to pertinent system parameters, and to model the AMOS visible PRIM experiment to aid in its design. Both of these objectives have been accomplished. Images resulting from the simulation studies are exhibited in Figs. 38 through 45 and represent grey-scale displays of PRIM reconstructed images. From these displays it can be concluded that the parameter ranges required to achieve image quality sufficient to extract information near the diffraction limited resolution of the PRIM system are as follows:

- Five or more overlays for speckle averaging
- Signal-to-noise ratio of 3 or greater
- Glint amplitude of 125 or greater
- Glint amplitude differential of 2 to 1 ratio or greater in multiglint situations
- Digitizing to 2 bits or more.

The figures exhibited in this section are composite grey-scale displays which depict the variation of image quality as a function of a specified system parameter. As such, they represent a sequence of progressive image reconstructions as the parameter in question is varied through its range. Therefore, the effect of any particular parameter on image quality, as well as the transition region for producing good image quality can be readily determined.

B. Computer Simulation Scheme

The simulation study was carried out using a DEC/PDP-10 digital computer. A block diagram of the simulation scheme is shown in Fig. 37. The sequence utilized in the simulation is as follows:

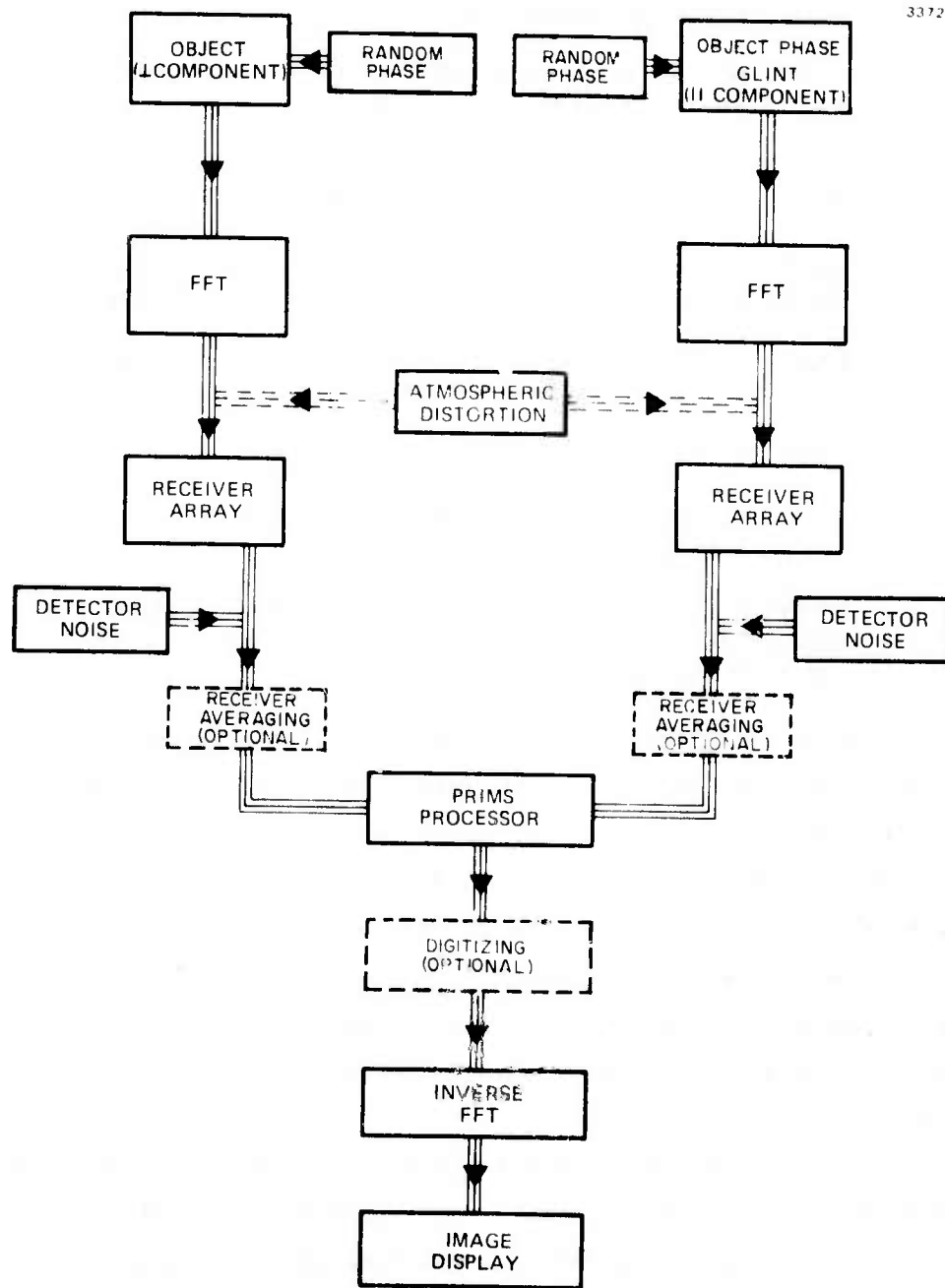


Figure 37. PRIM computer simulation block diagram

- Randomize the phase of the coherent field scattered from the object for the cross-polarized (perpendicular) component
- Fast Fourier transform (FFT) the randomized object scattered field
- Add Gaussian receiver noise to the received Fourier transform of the object scattered field
- Repeat the above steps for the polarized (parallel) component with a glint distribution superimposed
- PRIM process these signal components received through a specified aperture configuration
- Digitize the processed signal (optional)
- Inverse Fourier transform the PRIM processed signal to reconstruct the image
- Display the reconstructed image on a suitable format such as grey level CRT or computer print-out with overprint grey scales.

A detailed description of the simulation scheme is discussed below. The domain of available computational space is given by the mesh-size of the matrix used in the simulation. For these computations 128×128 mesh-points were used. Within each matrix the maximum extent utilized for object or aperture configurations was restricted to one-half the linear dimension of the available matrix space, i. e., the central 64×64 mesh-points. This restriction was necessary in order to avoid "edge effects" because of the periodic property of discrete Fourier transforms.

The turbulence phase screen used in the simulation studies was generated by a fast Fourier transform technique which yielded a two-dimensional distribution of gaussian random numbers having correlation properties consistent with those associated with Kolmogorov turbulence. Because the atmospheric turbulence effect exactly cancel in the PRIM system, the turbulence generating subroutine was not invoked in the PRIMS simulation studies in order to conserve computation time.

To simulate the speckle effect caused by the coherent illuminator in a PRIM system, a random phase was assigned to each element of the object matrix. The value of the assigned random phase ranged uniformly from 0 to 2π , and was selected from a uniformly distributed random number generator. Therefore, the surface roughness of the object corresponds to at least one-half wavelength in depth, and its correlation length corresponds to one mesh point $\Delta x'$ (defined below). Different random phase distributions were used for the copolarized and cross-polarized components of the scattered field, corresponding to the object scattered fields with and without glints, respectively. In addition, each exposure of the PRIM recording process utilized a different random distribution. In simulating the copolarized component of the object scattered field, a specified distribution of glints, at given amplitudes and spatial dispositions, was superimposed on the object.

The Fourier transform of the object scattered field was obtained by means of a fast Fourier transform (FFT) routine, after which additive Gaussian noise was incorporated into each component of the transformed signals. The noise spectrum simulated the photomultiplier noise of the receivers used in the detection stage. After both components of the object scattered field were similarly transformed, PRIM processing was accomplished by performing a conjugate product of these two components. The finite dimension of the receiver aperture was then simulated by rendering the mesh points outside the aperture equal to zero. Therefore, only the signals within the aperture were sampled. Various aperture sizes can be chosen in the simulation to correspond to different physical situations, with the object mesh size $\Delta x'$ and aperture mesh size Δx related by

$$\Delta x' \Delta x = \frac{\lambda R}{N} \quad , \quad (14)$$

where

λ is the illumination wavelength

R is the range

N is the number of mesh points in a linear dimension used in the simulation.

This relation arises as a consequence of the transformation from continuous to discrete Fourier transform. It can be recast into the usual diffraction limited resolution relation by setting $N\Delta x = mD$, where D is the aperture size and m is an integer. Equation (14) then becomes

$$m\Delta x' = \frac{\lambda}{D} R, \quad (15)$$

where $m\Delta x'$ is the linear resolution cell size in the object plane.

Two options are available in the simulation scheme. One of these applies when the size of each detector element encompasses more than one mesh-point in the computational matrix employed. In this case, an $n \times n$ block of mesh-points is assigned to each detector. This is shown by the receiver averaging block in Fig. 37. The other option digitizes the PRIM processed signal at each receiver element into N -bits before the inverse transformation is performed to reconstruct the image. Both the real and imaginary parts of the complex PRIM processed signal are digitized separately into N -bits.

Finally, after the above steps have been completed, an inverse FFT was performed on the PRIM processed signal and a reconstructed image thereby obtained. The reconstructed image can be displayed either as a grey scale overprint on the computer print-out, or it can be displayed in a 16-level grey scale format on a display scope. For reference, each grey scale image contains a 16-level intensity scale superimposed at the bottom. No post-processing was applied to these images; restoration and enhancement techniques were ignored in these simulation studies.

C. PRIMS Reconstructed Images

A total of 8 figures are included in this section to display the PRIM reconstructed images. Each display exhibits the evolution of the reconstructed image as a function of a specified parameter over a range of values selected to represent possible operation conditions. The list below briefly describes the parameter study exhibited in each figure.

- Fig. 38 Pictorial Summary of PRIM
- Fig. 39 PRIM Speckle Averaging
- Fig. 40 PRIM Signal-to-Noise Ratio
- Fig. 41 PRIM Glint Amplitude
- Fig. 42 PRIM Glint Distribution
- Fig. 43 PRIM Digitized Receiver Signal
- Fig. 44 PRIM Receiver Averaging
- Fig. 45 Auto-Correlation Function of Object

The above set of figures are discussed in detail below in order to highlight the major features of each display.

POLARIZATION REFERENCE IMAGING

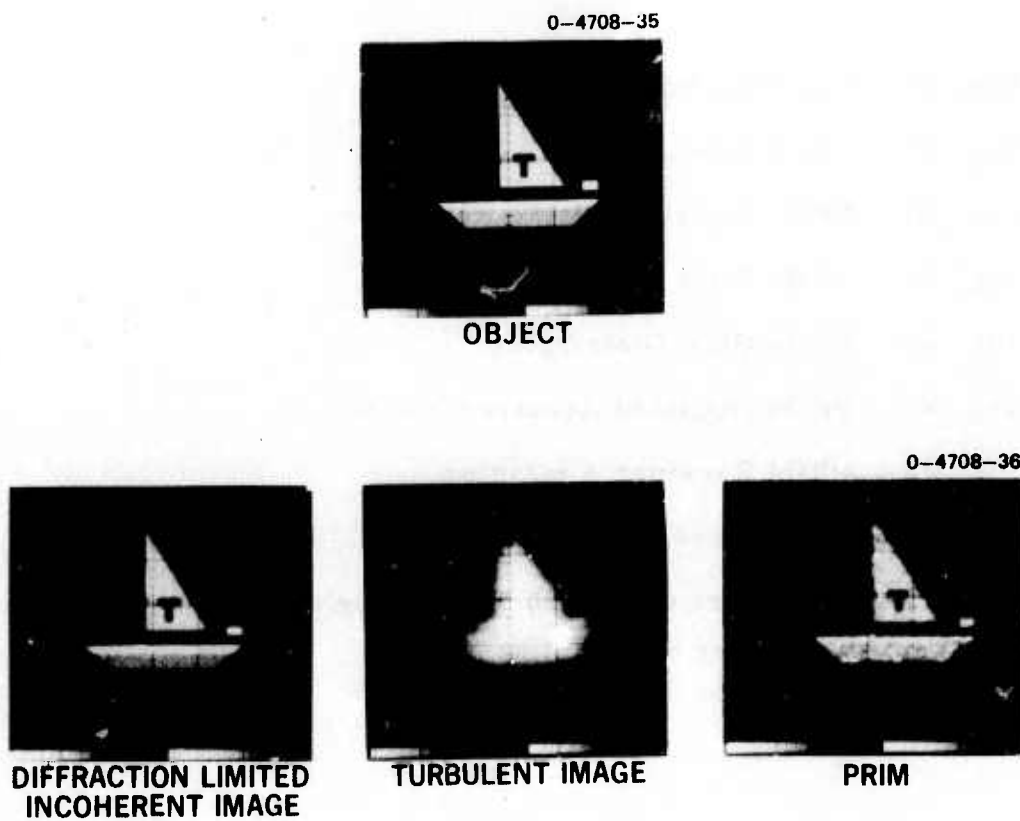


Figure 38. Pictorial summary of PRIM system performance capability.

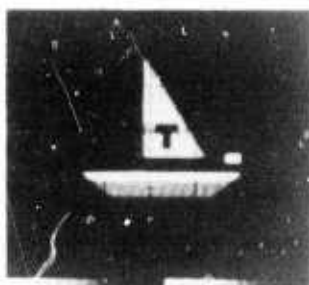
Figure 38. A pictorial summary of the PRIM system is shown here, consisting of the object, a diffraction limited incoherent image, a turbulent image corresponding to turbulence with 10 cm phase coherence length, and the PRIM processed image. The object consists of a grey level geometric sailboat centered in a 128×128 mesh-point grid. Only the center 64×64 mesh-points were utilized for the sailboat, with the outer boundary assigned the lowest grey scale level to simulate a dark space background. A dynamic range of 25 in amplitude (625 in intensity) was selected here. The dynamic range was divided into 25 linear discrete levels, and grey scale assignments were made to each mesh-point of the object. For the aperture sizes used in the simulations, the diffraction limited resolution cell on the object consists of either a 2×2 mesh-point square (for a 64×64 mesh-points matrix aperture) or a 3×3 square (for a 43×43 aperture), as can be deduced from eq. (15). The diffraction limited incoherent image represents the best possible image quality obtainable with the aperture under ideal conditions, i.e., infinite signal-to-noise, no turbulence, etc. It is shown as a comparison to the PRIM figures for image quality assessment. The turbulent image represents the image quality achievable in turbulence with 10 cm phase coherence length, if no restorations were used to remove the effects of distortion. Finally, the PRIM reconstructed image represents the restored image using PRIM processing. It possesses the same image quality as a diffraction limited coherent image under the same conditions in the absence of turbulence.

SPECKLE AVERAGE

0-4708-32

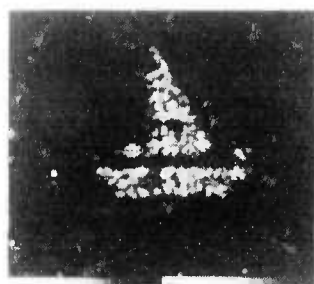


TURBULENT IMAGE



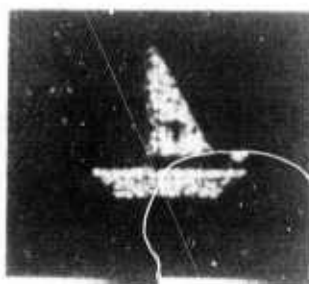
DIFFRACTION LIMITED
INCOHERENT IMAGE

PRIM
S/N RATIO: 300
GLINT AMPLITUDE: 500
NUMBER OF LEVELS: 16
64 x 64 APERTURE

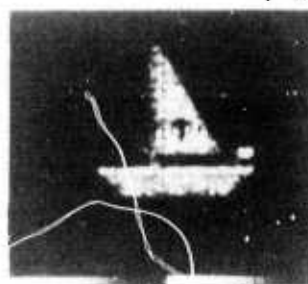


NUMBER OF
OVERLAYS:

1

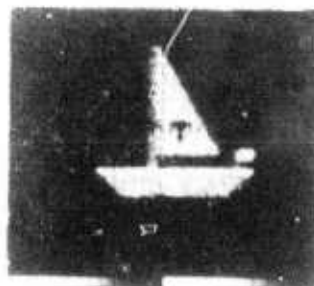


3



5

0-4708-33



10



20

0-4708-34

Figure 39. PRIM system performance as a function of speckle averaging.

Figure 39. The PRIM processed images are displayed as a function of the number of overlays to determine the effect of speckle averaging. It is seen that the major features of the object can be interpreted with five overlays and that the speckle becomes insignificant at about 10 overlays. There is only a slight improvement in picture quality when the overlays are increased to 20 or more. We conclude that 10 overlays are sufficient to negate almost all speckle effects. The general behavior of the PRIM image quality is similar to that of a diffraction limited coherent image. High values of signal-to-noise ratio and glint amplitude were chosen here so as to isolate the effect of speckle averaging. Under these conditions, the PRIM processed images are indistinguishable from the diffraction limited coherent images and 5 overlays are sufficient for a PRIM demonstration experiment.

SIGNAL TO NOISE

0-4708-28



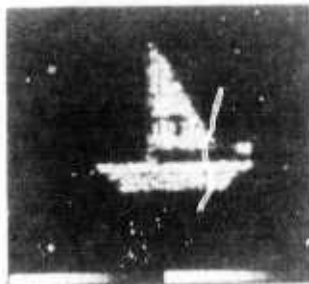
TURBULENT IMAGE



DIFFRACTION LIMITED
INCOHERENT IMAGE

PRIM
GLINT AMPLITUDE: 500
NUMBER OF OVERLAYS: 5
NUMBER OF LEVELS: 16
64 x 64 APERTURE

0-4708-29



S/N RATIO: 1



2



3

0-4708-30



10

0-4708-31



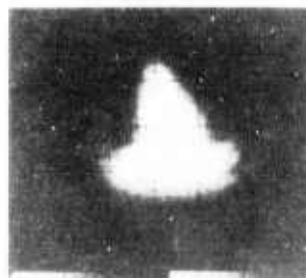
1

Figure 40. PRIM system performance as a function of signal-to-noise ratio.

Figure 40. The PRIM processed images are displayed as a function of the signal-to-noise ratio of the system, which is defined as the ratio of the average signal power in the aperture plane to the RMS noise power of the detector. The S/N ratio indicated in the display is that ratio used for each overlay. The images were computed using five overlays in order to conserve computation time and should be compared to the five overlay images in Fig. 39 to assess the effect of noise on image quality. It is seen that for S/N ratio of 3 or greater the image quality is quite excellent. The noise, which appears primarily as a random background level, no longer is significantly visible for S/N ratios of 3 or more. To amplify this point, the picture at the lower right corner is a duplicate of the S/N = 1 picture with the intensity level of the CRT display turned up in order to exhibit the background noise level. Of course, at this display intensity level, the object intensities saturate the film.

GLINT AMPLITUDE

0-4708-25



TURBULENT IMAGE



DIFFRACTION LIMITED
INCOHERENT IMAGE

PRIM

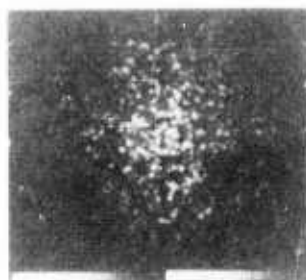
S/N RATIO: 300

NUMBER OF OVERLAYS: 5

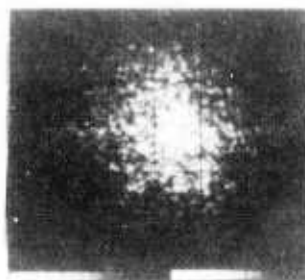
NUMBER OF LEVELS: 16

64 x 64 APERTURE

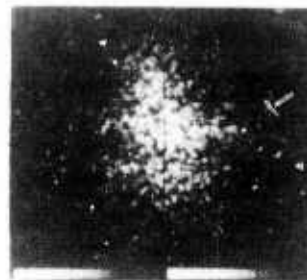
0-4708-26



GLINT AMPLITUDE: 1



10



50

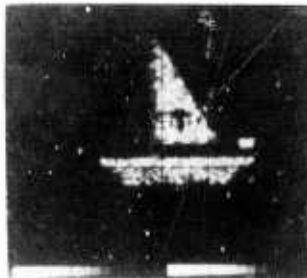
0-4708-27



100



125



200

Figure 41. PRIM system performance as a function of glint amplitude

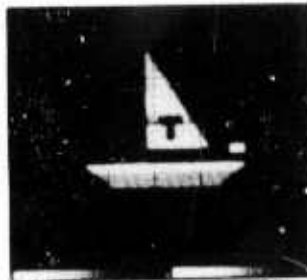
Figure 41. Here, the PRIM processed images are displayed as a function of glint amplitude. A single glint of specified amplitude above the local reflectivity was used to compute the evolution of the PRIMS images. It is seen that as the glint amplitude increased, the image appears to evolve from the background noise pattern; the image is brought out by the convolution of the glint with the perpendicular component of the reflected signal. Glint amplitudes of 125 or above produce good quality images.

MULTIGLINT PRIMS

0-4708-22



TURBULENT IMAGE



DIFFRACTION LIMITED
INCOHERENT IMAGE

PRIM

S/N RATIO: 300

NUMBER OF OVERLAYS: 5

NUMBER OF LEVELS: 16

64 x 64 APERTURE

0-4708-23

2 GLINTS



GLINT RATIO 1 : 1



1 : 1/5



1 : 1/10

0-4708-24

3 GLINTS



GLINT RATIO 1 : 1 : 1



1 : 1/2 : 1/5



1 : 1/5 : 1/10

Figure 42. PRIM system performance as a function of glint distribution.

Figure 42. The PRIM processed images with multiglint distributions are shown for a 2-glint and 3-glint distribution. Each distribution encompassed a range of relative glint ratios, as indicated on the display. Multiglint distributions produce multiple images, one image corresponding to each glint. However, as can be seen, a glint amplitude differential of 2 to 1 or more is all that is required to achieve discrimination between the multiple images. The image produced by the lower amplitude glint is barely visible relative to the higher amplitude glint when their ratio differs by more than a factor of 2.

DIGITIZED PRIMS

0-4708-19



TURBULENT IMAGE



DIFFRACTION LIMITED
INCOHERENT IMAGE

64 x 64 APERTURE MATRIX

NUMBER OF OVERLAYS: 5

GLINT AMPLITUDE: 500

S N RATIO: 300

0-4708-20

LINEAR



1 BIT



2 BIT



3 BIT

0-4708-21

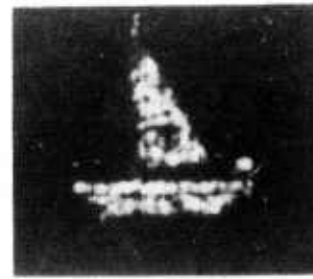
LOGARITHMIC



1 BIT



2 BIT



3 BIT

Figure 43. PRIM system performance as a function of receiver signal digitization.

Figure 43. The PRIM processed images for which the received signals were digitized prior to the inverse FFT operation is shown here for 1-, 2-, and 3-bit digitization (sign included). Both linear and logarithmic digitizing schemes were employed. The results show image quality that is relatively insensitive to the number of bits used in the digitizing or to the method of digitizing. As can be seen, even 1 bit digitizing preserves good image quality. Part of the reason for this is that both the real and imaginary parts of the received (complex) signal are digitized separately. Thus, this is equivalent to digitizing a real signal with an additional bit. In addition, because of the random distribution imposed on the object (i.e., resultant speckled images) only a low digitizing level is required to preserve good image quality.*

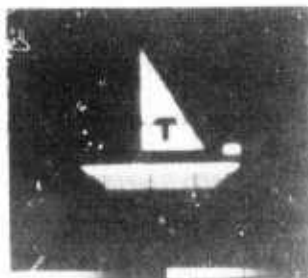
*David Ketchum, private communications.

RECEIVER AVERAGING

0-4708-16



TURBULENT IMAGE



DIFFRACTION LIMITED
INCOHERENT IMAGE

PRIM

S/N RATIO: 300

GLINT AMPLITUDE: 500

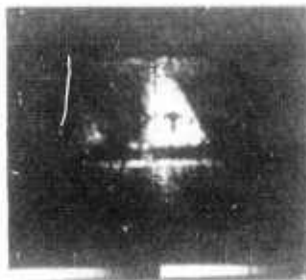
NUMBER OF OVERLAYS: 5

NUMBER OF LEVELS: 16

64 x 64 APERTURE



2 x 2



3 x 3



4 x 4

0-4708-17

43 x 43 APERTURE



2 x 2



3 x 3



4 x 4

0-4708-18

Figure 44. PRIM system performance as a function of receiver averaging.

Figure 44. The effect of receiver size on the reconstructed image is simulated here. In the previous and following figures every mesh-point was sampled in the 64×64 aperture. When the physical size of the sampling receiver encompasses more than one mesh-point, the signals (mesh-points) within each receiver must be averaged in value. This figure shows the effect of receiver size for receivers that encompass from 2×2 to 4×4 mesh-points each. The effect of receiver averaging is that the field-of-view of the system is decreased for larger receiver sizes (because the system field-of-view is determined by the individual receiver size), while the system resolution (determined by the system aperture size) is maintained because the aperture dimensions have not been changed. This is clearly illustrated here; two aperture sizes were chosen to demonstrate both the field-of-view variation and system resolution variation.

AUTO-CORRELATION

0-4708-13



TURBULENT IMAGE



DIFFRACTION LIMITED
INCOHERENT IMAGE

64 x 64 APERTURE MATRIX

NUMBER OF OVERLAYS: 5

GLINT AMPLITUDE: 500

S N RATIO: 300

NO GLINT

0-4708-14



NUMBER OF LEVELS: 48



96



200

1 GLINT

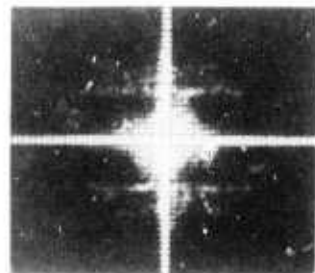
0-4708-15



NUMBER OF LEVELS: 96



200



1000

Figure 45. Auto-correlation function of object, with and without glint.

Figure 45. Finally, as a comparison to other schemes of reconstruction, the auto-correlation function of the object is displayed here for both a no-glint and a 1-glint case. In the display the total range of the image signal was divided into N linear discrete levels. Only the lowest 16 levels were shown as grey-scale shades; the $(N-16)$ upper levels were compressed into the highest intensity level.

D. Conclusions

From the computer simulation of the PRIM processed images, it is evident that image qualities approaching the diffraction limited coherent image can be achieved if certain broad conditions are satisfied. These conditions include:

- Five or more overlays for speckle averaging
- Signal-to-noise ratio of greater than 3 for each overlay.
- Glint amplitude of greater than 125.

In addition, it was determined that multiglint distributions on the object are quite tolerable if there exists a difference of a factor of 2 in amplitude between the dominant glint and the rest of the distribution. Under this situation, the multiple images that result from multiple glint distributions are well discriminated in intensity. The image corresponding to the highest amplitude glint dominates the remaining (multiple) images, even in the absence of post-processing.

The effect of using larger-sized receivers (antennas) in a given full aperture is the reduction in the system field of view. The overall system resolution, determined by the aperture size, remains constant. Finally, digitizing can be carried out with a relatively low number of bits (2 or 3) without sacrificing image quality.

VI. PUBLICATIONS AND PRESENTATIONS

The following presentations and publications have arisen from work carried out on the present contract.

Presentations

D. Y. Tseng, "Polarization Reference Imaging Systems, Part II," CLEA 1975.*

M. E. Pedinoff "Fiber Optic Delay Lines for Use in Time-Delay Multiplexing of Optical Images," Presented at the 19th Annual Technical Symposium Society of Photo Optical Instrumentation Engineers Aug. 18-22 1975, San Diego, California, to be published in the proceedings.

Publications

D. Y. Tseng, "Polarization Reference Imaging Systems, Part II," to be published in Applied Optics, CLEA Issue, June 1976.*

*Part I of a companion paper by W. P. Brown, T. O'Meara was presented at same conference, and will be published in same issue.

APPENDIX A

SEEING MONITOR INDICATORS, OUTPUTS, AND CONTROLS

1. SEEING MONITOR METER INDICATORS

a. Seeing Lights

The eight lights located under the seeing meters show the binary output of the eight bit seeing counter. Once every millisecond the accumulated count is transferred to eight latches which in turn provide storage and an input to the eight light drivers.

b. Seeing Meter

The output from the seeing counter is also used to drive the inputs of a D to A converter. The D to A converter in turn drives the seeing meter and provides a non-integrated analog voltage which appears on a BNC connector at the rear of the cabinet. Because of mechanical integration the needle of the seeing meter tends to average the fluctuations in the seeing angle.

c. Wander Meter

The wander circuit is a closed loop servo system in which a voltage is generated that is proportional to the position of the incoming light in the field of view. An integrator fed by the synchronous wander detector supplies the voltage for the wander meter and the start pulse comparator.

d. Wander Lights

The wander lights located above each wander meter display a digital count that represents the position of the incoming light in the field of view. These lights actually show the count from an eight-bit counter that starts counting when the start pulse is generated and stops counting when the reference pulse arrives. The wander lights are updated every millisecond.

e. Brightness Meter

One meter is used to show "brightness" or photomultiplier tube voltage for both channels. A switch is provided on the front panel which selects one of two voltage dividers. The voltage dividers are connected

to the photomultiplier's high voltage supply, thus the brightness meter is a direct reading of the voltage supplied to the photomultiplier.

2. SWITCHES AND CONTROLS

a. Sensitivity Switch

The sensitivity switch, located in the right-hand corner of the front panel, activates a gain changing relay in the post-amp (on-board electronics). A gain of 1.1 (in normal position) or 4.5 (in the high position) can be selected. It has been found that under conditions of normal use the sensitivity switch should be left in the "high" position.

b. Motor Switch

This switch allows the reticle wheel motor to be turned off while the system remains on. When the Seeing Monitor is not in use and thermal equilibrium of the electronics is desired, the motor should be shut off.

c. Range Switch

The selection of the three possible magnifications is made with the range switch. When a selection is made and the proper positioning of the lens turret is completed, the "arc seconds" lamp will light. A 2-bit digital encoder shows the lens turret position by use of two LEDs (located next to wander reset).

d. Image Orientation Control

The image orientation control knob is fastened directly to a 60 Hz synchro-transmitter. A synchro-receiver located next to the dove-prism is used to rotate the dove-prism carriage. A 2-to-1 reduction from synchro-receiver to dove-prism carriage compensates for the double rotation of the beam for every revolution of the prism. A six-bit shaft encoder provides digital angular information in binary form which can be viewed on the orientation lights.

c. Wander Reset

Occasionally when a new magnification is selected or the incoming light is interrupted, the wander integrator output voltage can drift beyond the capturing capability of the wander servo system. The reset button on the front panel, shunts the voltage across the integrator capacitor which allows the wander servo to recapture a true wander voltage.

3. ELECTRICAL OUTPUTS (BNC Connectors)

a. Wander

The signal that appears at the wander output BNC comes from the wander integrator through a 4700 ohm resistor. The wander integrator has a time constant of approximately 5 milliseconds and an output voltage capability of ± 12 volts.

b. Seeing* (front panel)

The seeing BNC connector provides serial digital data from the eight-bit seeing counter at a one millisecond rate. The output voltage is approximately 10 volts. Output polarity is selectable with an internal switch, located in slot "I" of the Seeing Monitor.

c. Seeing (back panel)

The seeing BNC on the back panel provides an analog voltage that is proportional to the accumulated count of the eight-bit seeing counters. The final count is then fed into a D to A converter to provide a new analog voltage for the seeing meters and the seeing BNC. The output capability of the D to A converter is approximately 12 Vdc.

d. Start Pulse

The start pulse is generated in the wander section using the voltage from the wander integrator and the voltage from a linear ramp to feed a comparator. When the ramp voltage becomes greater than the voltage from the wander integrator, the voltage comparator triggers the start pulse one-shot. The start pulse is one microsecond wide and about 3.8 volts in amplitude. The start pulse starts the seeing counters as well as the wander counters.

e. Stop Pulse BNC

A stop pulse, used to stop the seeing angle counters is generated each time the amplitude of the MTF curve reaches half of its initialized value. The one-half MTF value is detected by a comparator which, in turn, triggers a one-shot multivibrator with a 1 microsecond pulse width. The output of the stop-pulse one-shot is buffered with a 27 K ohm resistor which makes the stop pulse amplitude appear to be only 0.2 volts when viewing with a scope.

f. MTF

The connector marked MTF (with no line under the letters) provides one positive going analog MTF curve per millisecond. The first portion of each MTF curve is initialized by a pulse whose amplitude is proportional to the instantaneous brightness seen by the photomultiplier during the first dark-light sector of the reticle wheel. The initialization pulse actually presets the capacitors in the 2.2 kHz MTF filter to the brightness level.

g. MTF

This BNC connector is identified with a slash under the letters, "MTF". The slash denotes an inverted MTF curve of the same amplitude.

h. Brightness

The brightness connector provides a voltage from the output of the brightness integrator. The brightness information is obtained by integrating over several sectors of the reticle wheel. The maximum voltage to expect from the BNC brightness under bright light conditions is around 3.5 V.

i. Motor Control

The voltage that controls the reticle wheel motor appears at the motor control BNC on the front panel. Speed errors will appear as variations in the control voltage until a motor speed lock is achieved.

j. Motor Speed

This BNC connector provides a bipolar voltage that is proportional to the instantaneous error in motor speed. An eight-bit counter, clocked by the crystal controlled master oscillator is gated on between reference slots on the reticle wheel. The accumulated count is then transferred to a D to A converter which generates the instantaneous bipolar error voltage.

k. PM

The amplified and filtered signal from the photomultiplier tubes can be monitored at the PM BNC on the front panel.

l. REF*

The REF BNC connector located in the lower right-hand corner of the control panel, provides serial digital wander data for channels 1 and 2, and range and orientation data along with synchronizing pulses for deserializing all the data that leaves the Seeing Monitor. The output voltage is approximately 10 volts, with polarity selectable with a toggle switch located on the card in slot "J" of the Seeing Monitor.

m. Auxiliary BNC

The BNC connectors located to the far left of the control panel (numbered 1 and 2) are not connected and can be used to bring out desired signals not already provided.

APPENDIX B

SEEING MONITOR - DIGITAL OPERATION

1. Control Electronics

The Seeing Monitor puts out three serial digital data streams. Each is to be recorded on one digital channel of a tape recorder. These three streams give digitized values for seeing angle for both channels, wander for both channels, and magnification range and image orientation (the setting of the Dove prism).

Figure B-1 illustrates the three data streams. Each stream consists of a standard 8-data-bit asynchronous burst once per millisecond. The bit time is 62.5 μ sec, or equivalently the bit rate is 16.0 kHz. The burst consists of a start bit (always logical zero), eight data bits, and a parity bit. The data bits are ordered with least-significant-bit (LSB) first. The parity bit is logical one if an even number of data bits are logical one. Otherwise it is logical zero. The burst occupies 625 μ sec and the dead space between bursts (i.e., the stop bit time) is 375 μ sec. The signal is logical one during the stop bit time. The seeing angle is encoded as an eight-bit binary number. This number is displayed on the eight panel lights under the seeing meter; the lights are on for logical one and off for logical zero.

The output levels are standard voltages used for recording digital information: zero volts for logical one and + 10 V for logical zero. Since some recorders use -10 V for logical zero, a switch is provided on the two logic section cards and the reference logic card to select this option. (The digital recorder may have its definition of logical one and logical zero reversed from that given above; this definition is arbitrary and a recorder having either definition will operate properly with the Seeing Monitor.)

Each burst on data stream one gives seeing angle for channel one. Each burst on data stream two gives seeing angle for channel two. Data stream three samples three pieces of information in successive milliseconds and then inserts a synchronization burst. This pattern of four samples (indicated in Fig. B-1) is repeated indefinitely. Following the synchronization burst are, in order, channel one wander, channel two wander, and range orientation.

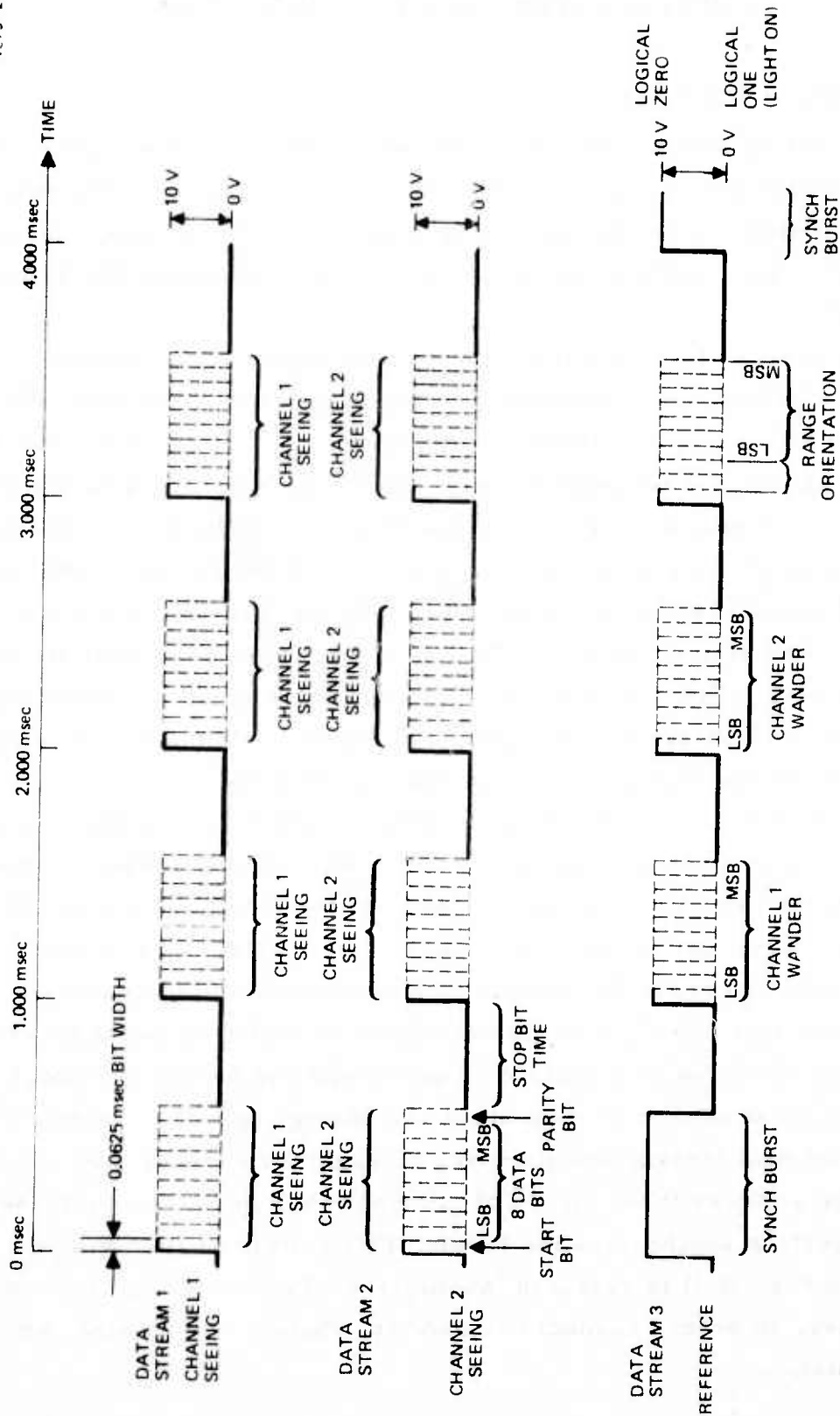


Figure B-1. Digital data stream outputs.

The wander is an eight-bit binary number which is linearly related to the position of the image in the field of view. This binary number is also indicated in the lights above the wander meter: the light is on for logical one and the LSB is on the left.

2. Data Receiver

The data receiver converts each of the three data streams to parallel data which can be read in real time by most computers. The data receiver also displays the data on panel lights. The data receiver may be operated on-line by running the three data stream outputs from the control electronics directly to the data receiver, or it may be operated off-line by recording the data streams digitally and then playing them back into the data receiver. The data receiver may be connected to the three data streams in parallel with the tape recorder to monitor the data as it is being recorded.

The lights on the data receiver duplicate corresponding ones on the control electronics with the following two exceptions. Seeing and wander cannot both be displayed at once; a switch selects seeing or wander to be displayed on the seeing/wander lights. Also, the last values for seeing or wander may be frozen at any time by switching the run-freeze switch to freeze.

After the power switch is turned on, the start button must be depressed to start the data receiver. This button may be depressed at any time to restart the data receiver. (This should be done if one of the four lights mentioned below stays off.) During proper operation, the lights clock, data rcvd. ch. 1, data rcvd. ch. 2, and data rcvd. ch. 3 will all glow half-bright. If a data rcvd. light is dark, data is not coming in on its corresponding input. The parity error light flickers briefly whenever a parity error is detected on any of the three data streams. The framing/overrun error light flickers if the data burst on any data stream is more than 650 μ sec wide (possibly indicating a tape-speed error).

The "clock" is a 256 kHz oscillator that provides timing for the deserializers. The clock's waveform appears on one terminal of the clock light. The deserializer clock rate trim is used to adjust the frequency to 256 ± 4 kHz.

3. Data Receiver Output to Computer

The data receiver has twelve data lines, BUS_1 thru BUS_{12} , and one interrupt line, INTR, that must be connected to the computer if computer interpretation of results is desired. Figure B-2 illustrates the information on these lines. The lines are all TTL compatible outputs (logical one is 3.5 V and logical zero is 0 V). To read this data, the computer must be able to accept twelve bits of digital input and must either have an interrupt capability or must be able to read the INTR line as a thirteenth digital input and act accordingly. Most computers and minicomputers have one of the above capabilities. A useful technique is to use a minicomputer to read this data and reformat it onto a standard computer tape which can be read later by a large computer for processing; this way the processing need not be done in real time.

Of each 1-msec period, 180 μ sec are used for data transfer to the computer. The 180 μ sec consist of three consecutive 60- μ sec periods: the interrupt line goes to logical one for 10 μ sec to signal the beginning of each period.

During the first 60- μ sec period, the 8 bits of data from stream 1 are placed on BUS_1 thru BUS_8 (BUS_1 is the least significant bit). BUS_9 and BUS_{10} are logical one unless a parity error or framing/overflow error, respectively, occurs on data stream one. BUS_{11} and BUS_{12} are logical one to indicate that stream one is being output.

During the second 60- μ sec period the above is done for stream two. BUS_{11} is logical zero and BUS_{12} is logical one to indicate stream two.

During the third 60- μ sec period, the same is done for stream three; BUS_{11} is logical one and BUS_{12} is logical zero to indicate stream three.

The 60- μ sec interval was chosen to allow the computer adequate time to read the data (a typical time for handling an interrupt is 12 μ sec), yet allow 820 μ sec of each millisecond for background processing.

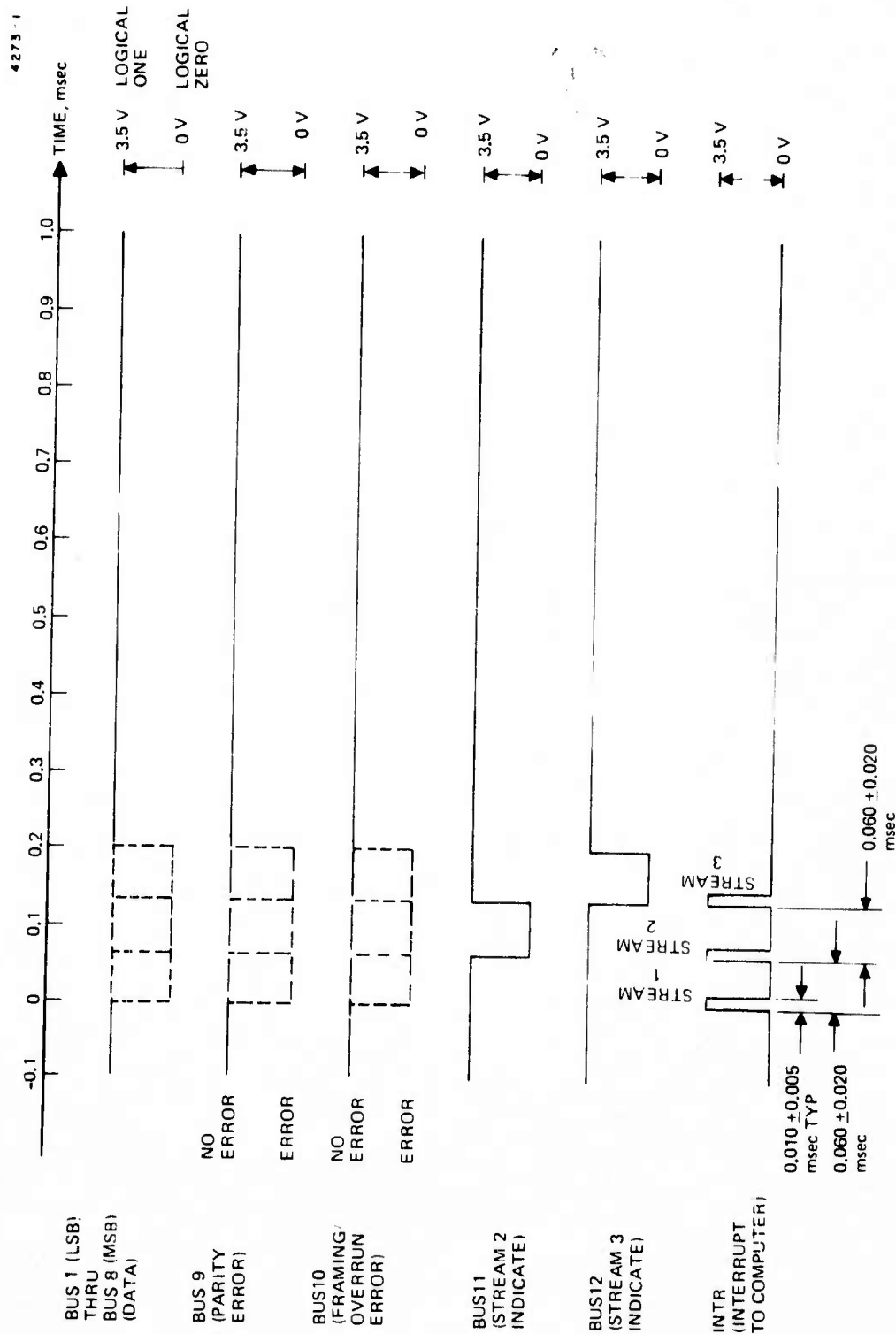


Figure B-2. Parallel digital format in data receiver from serial input.

APPENDIX C

SEEING MONITOR SIGNAL-TO-NOISE CALCULATIONS

I. DEMODULATOR OUTPUTS

The image delivered to the chopping wheel is $I(x, y)$. The effect of the chopping wheel (for the x channel detector) is to multiply the image by the transmission function $W(\alpha t - x/R)$, where

$$W(\theta) = S(\phi_0 e^{\theta/\theta_0}) \quad ; \quad 0 \leq \theta \leq \pi/6$$

$$W(\theta) \equiv W([\theta]) \quad ; \quad \theta > \pi/6$$

$$[\theta] \equiv [\theta]_{\text{mod } \pi/6}$$

$$S(\phi) = \begin{cases} 0 & ; \quad \sin \phi > 0 \\ 1 & ; \quad \sin \phi < 0 \end{cases}$$

α is the angular frequency of chopping wheel rotation, ϕ_0 and θ_0 are constants describing the chopping pattern spacing and its range of change, and R is the distance from the wheel center to the image. The use of $W(\alpha t - x/R)$ implies the approximation that the image size is much smaller than R . [We assume that the star image itself changes very slowly compared to all time scales intrinsic to the monitor, so that $I(x, y)$ does not depend on the time t .] The chopped image is then

$$I^T(x, y, t) = W(\alpha t - x/R) I(x, y) \quad .$$

The input to the demodulator is the integral of this:

$$\begin{aligned} I^T(t) &= \int dx dy I^T(x, y, t) \\ &= \int dx dy I(x, y) S\{\phi(x, t)\} \end{aligned}$$

where

$$\phi(x, t) \equiv \phi_0 \exp \left\{ \frac{\alpha t - x/R}{\theta_0} \right\}$$

We can expand S in a Fourier series:

$$S(\phi) = \frac{1}{2} - \frac{2}{\pi} \sum_{n_{\text{odd}}} \frac{1}{n} \sin(n\phi)$$

The dc modulator splits the input, multiplies by $\sin \phi(0, t)$ and $\cos \phi(0, t)$, and low-pass filters with a time constant τ_F . The bandwidth of the demodulator filters is 3.0 kHz and the characteristic time constant is $\tau_F = (\pi \times 3.0 \text{ kHz})^{-1} = 0.1 \text{ msec}$. Its outputs are thus

$$\begin{aligned} D \begin{pmatrix} I \\ Q \end{pmatrix} (t) &= \int_{-\infty}^t dt' e^{-(t-t')/\tau_F} d \begin{pmatrix} I \\ Q \end{pmatrix} (t') I^T(t') \\ d \begin{pmatrix} I \\ Q \end{pmatrix} (t) &= \begin{pmatrix} \sin \\ \cos \end{pmatrix} \phi(0, t) \end{aligned}$$

If

$$\tau_F \ll \left| \frac{\frac{\partial \phi}{\partial t}}{\frac{\partial^2 \phi}{\partial t^2}} \right| = \frac{\theta_0}{\alpha}^*$$

and

$$\text{image size} \ll \left| \frac{\frac{\partial \phi}{\partial x}}{\frac{\partial^2 \phi}{\partial x^2}} \right| \approx R\theta_0$$

then we are justified in using the first two terms in the Taylor expansion of $\phi(x, t')$ about $\phi(0, t)$:

$$\phi(x, t') \approx \phi(t) \left[1 + \frac{1}{\theta_0} \left\{ \alpha(t - t') - \frac{x}{R} \right\} \right]$$

where $\phi(t) \equiv \phi(0, t)$ in the integrand above. Then

*This is a reasonably good approximation, since $\tau_f = 0.1$ msec and $\theta_0/x = 0.22$ msec

$$\begin{aligned}
D_{(Q)}^{(I)}(t) &\cong \int_{-\infty}^t dt' e^{-(t-t')/\tau} F \left\{ \frac{\sin}{\cos} \right\} \left\{ \phi(t) \left[1 + \frac{\alpha(t-t')}{\theta_0} \right] \right\} \\
&\times \int dx dy I(x, y) \\
&\times \left\{ \frac{1}{2} - \frac{2}{\pi} \sum_{n_{\text{odd}}} \frac{1}{n} \sin \left[n\phi(t) \left(1 + \frac{\alpha(t-t') - x/R}{\theta_0} \right) \right] \right\} \\
&= \int_{-\infty}^t e^{-(t-t')/\tau} F \left\{ \frac{\sin}{\cos} \right\} \left\{ \phi(t) \left[1 + \frac{\alpha(t-t')}{\theta_0} \right] \right\} \\
&\times \int dx dy I(x, y) \\
&\times \left\{ \frac{1}{2} - \frac{2}{\pi} \sum_{n_{\text{odd}}} \frac{1}{n} \sin \left[n\phi(t) \left(1 + \frac{\alpha(t-t')}{\theta_0} \right) \right] \right. \\
&\times \cos \left[n\phi(t) \frac{x}{R\theta_0} \right] \\
&+ \frac{2}{\pi} \sum_{n_{\text{odd}}} \frac{1}{n} \cos \left[n\phi(t) \left(1 + \frac{\alpha(t-t')}{\theta_0} \right) \right] \\
&\times \left. \sin \left[n\phi(t) \frac{x}{R\theta_0} \right] \right\}
\end{aligned}$$

$$\begin{aligned}
D_I(t) &\cong \int_{-\infty}^t dt' \int dx dy I(x, y) \\
&\times \left[\frac{1}{2} e^{-(t-t')/\tau_F} \sin \left\{ \phi(t) \left(1 + \frac{\alpha(t-t')}{\theta_0} \right) \right\} \right. \\
&- \frac{1}{\pi} \sum_{n_{\text{odd}}} \frac{1}{n} e^{-(t-t')/\tau_F} \left\{ \cos \left[(n-1) \phi(t) \left(1 + \frac{\alpha(t-t')}{\theta_0} \right) \right] \right. \\
&- \left. \left. \cos \left[(n+1) \phi(t) \left(1 + \frac{\alpha(t-t')}{\theta_0} \right) \right] \right\} \right. \\
&\times \left\{ \cos \left(n \phi(t) \frac{x}{R \theta_0} \right) \right\} , \\
&+ \frac{1}{\pi} \sum_{n_{\text{odd}}} \frac{1}{n} e^{-(t-t')/\tau_F} \left\{ -\sin \left[(n-1) \phi(t) \left(1 + \frac{\alpha(t-t')}{\theta_0} \right) \right] \right. \\
&+ \left. \left. \sin \left[(n+1) \phi(t) \left(1 + \frac{\alpha(t-t')}{\theta_0} \right) \right] \right\} \right. \\
&\left. \left\{ \sin \left(n \phi(t) \frac{x}{R \theta_0} \right) \right\} \right]
\end{aligned}$$

$$D_O(t) = \int_{-\infty}^t dt' \int dx dy I(x, y)$$

$$\times \left[\frac{1}{2} e^{-(t-t')/\tau_F} \cos \left\{ \phi(t) \left(1 + \frac{\alpha(t-t')}{\theta_0} \right) \right\} \right.$$

$$+ \frac{1}{\pi} \sum_{n \text{ odd}} \frac{1}{n} e^{-(t-t')/\tau_F} \left\{ \sin \left[(n-1) \phi(t) \left(1 + \frac{\alpha(t-t')}{\theta_0} \right) \right] \right.$$

$$\left. + \sin \left[(n+1) \phi(t) \left(1 + \frac{\alpha(t-t')}{\theta_0} \right) \right] \right\}$$

$$\times \left\{ \cos \left(n \phi(t) \frac{x}{R \theta_0} \right) \right\}$$

$$+ \frac{1}{\pi} \sum_{n \text{ odd}} \frac{1}{n} e^{-(t-t')/\tau_F} \left\{ \cos \left[(n-1) \phi(t) \left(1 + \frac{\alpha(t-t')}{\theta_0} \right) \right] \right.$$

$$\left. + \cos \left[(n+1) \phi(t) \left(1 + \frac{\alpha(t-t')}{\theta_0} \right) \right] \right\}$$

$$\times \left\{ \sin \left(n \phi(t) \frac{x}{R \theta_0} \right) \right\} \Bigg]$$

Since

$$\int_{-\infty}^t dt' e^{-(t-t')/\tau_F} \begin{Bmatrix} \sin \\ \cos \end{Bmatrix} (A + Bt')$$

$$= \frac{\frac{1}{\tau_F} \begin{Bmatrix} \sin \\ \cos \end{Bmatrix} (A + Bt) \mp B \begin{Bmatrix} \cos \\ \sin \end{Bmatrix} (A + Bt)}{(1/\tau_F)^2 + B^2}$$

where B is typically

$$(n \mp 1) \phi(t) \frac{\alpha}{\theta_0} \gg \frac{1}{\tau_F} \quad ; \quad n \neq 1$$

the dominant contribution to $D \begin{pmatrix} I \\ Q \end{pmatrix}$ comes only from the $n - 1 = 0$ terms.
Then

$$D_I(t) \cong -\frac{\tau_F}{\pi} \int dx dy I(x, y) \cos \left[\phi(t) \frac{x}{R\theta_0} \right]$$

$$D_Q(t) \cong \frac{\tau_F}{\pi} \int dx dy I(x, y) \sin \left[\phi(t) \frac{x}{R\theta_0} \right]$$

and the MTF output is (correctly) given by

$$\text{MTF} \left(\frac{\phi(t)}{R\theta_0} \right) = \sqrt{D_I^2(t) + D_Q^2(t)}$$

II. S/N RATIO

From the above,

$$D_{\left(\begin{smallmatrix} I \\ Q \end{smallmatrix}\right)}^{(t)} = K \tau_F \int dx dy I(x, y) \begin{Bmatrix} \cos \\ \sin \end{Bmatrix} \left\{ \phi(t) \frac{x}{R\theta_0} \right\}$$

where K is some constant and where we will measure $I(x, y)$ in photons per unit area per unit time.

We compute

$$\sigma_{\left(\begin{smallmatrix} I \\ Q \end{smallmatrix}\right)}^2(t) = \left\langle D_{\left(\begin{smallmatrix} I \\ Q \end{smallmatrix}\right)}^2(t) \right\rangle - \left\langle D_{\left(\begin{smallmatrix} I \\ Q \end{smallmatrix}\right)}(t) \right\rangle^2$$

where the averages $\langle \rangle$ are over photon statistics.

$$\begin{aligned} \sigma_{\left(\begin{smallmatrix} I \\ Q \end{smallmatrix}\right)}^2(t) &= K^2 \tau_F^2 \int dx dy dx' dy' \\ &\left\{ \langle I(x, y) I(x', y') \rangle - \langle I(x, y) \rangle \langle I(x', y') \rangle \right\} \\ &\begin{pmatrix} \cos \\ \sin \end{pmatrix} \frac{\phi(t) x}{R\theta_0} \begin{pmatrix} \cos \\ \sin \end{pmatrix} \frac{\phi(t) x'}{R\theta_0} \end{aligned}$$

We assume that the noise in the image is uncorrelated from point to point:

$$\begin{aligned}
\langle I(x, y) I(x', y') \rangle &= \langle I(x, y) \rangle \langle I(x', y') \rangle \\
&= \left\{ \langle I^2(x, y) \rangle - \langle I(x, y) \rangle^2 \right\} \delta(x - x') \delta(y - y') \\
&\equiv \Sigma^2(x, y) \delta(x - x') \delta(y - y')
\end{aligned}$$

Σ^2 is uniquely determined by locality and Poisson statistics:

$$\Sigma^2(x, y) = \frac{1}{\tau_F} I(x, y)$$

Then

$$\begin{aligned}
\sigma_{\left(\frac{I}{Q}\right)}^2(t) &= \frac{1}{2} K^2 \tau_F^2 \int dx dy \Sigma^2(x, y) \left(1 \pm \cos \frac{2\phi(t) x}{R\theta_0} \right) \\
&= \frac{1}{2} K^2 \tau_F \int dx dy I(x, y) \left(1 \pm \cos \frac{2\phi(t) x}{R\theta_0} \right) \\
&= \frac{K}{2} \left[D_I(t_0) \pm D_I(t_2) \right]
\end{aligned}$$

where

$$\phi(t_0) = 0 \quad \phi(t_2) = 2\phi(t)$$

Assuming that

$$\sigma^2 \left| \frac{\partial \text{MTF}}{\partial D} \right|^2 \gg \frac{1}{2} \sigma^4 \left| \frac{\partial^2 \text{MTF}}{\partial D^2} \right|^2$$

the variance in MTF $[\phi(t)/R\theta_o]$ is

$$\begin{aligned}
 \sigma_M^2 &\cong \sigma_I^2 \left| \frac{\partial \text{MTF}}{\partial D_I} \right|^2 + \sigma_Q^2 \left| \frac{\partial \text{MTF}}{\partial D_Q} \right|^2 \\
 &= \frac{\sigma_I^2 D_I^2 + \sigma_Q^2 D_Q^2}{D_I^2 + D_Q^2} \\
 &= \frac{K}{2} \left\{ D_I(t_o) + D_I(t_2) \frac{D_I^2(t) - D_Q^2(t)}{D_I^2(t) + D_Q^2(t)} \right\} \\
 &\cong \frac{K}{2} D_I(t_o)
 \end{aligned}$$

Since

$$\theta_s = \frac{C}{k_{1/2}}$$

where

$$\text{MTF}(k_{1/2}) = \frac{1}{2} \text{MTF}(0)$$

we have

$$\frac{\sigma(\theta_s)}{\theta_s} = \frac{\sigma(k_{1/2})}{k_{1/2}}$$

Now

$$\sigma(k_{1/2}) = \frac{\sigma_M(k_{1/2})}{\left| \frac{\partial \text{MTF}}{\partial K} \right|_{k=k_{1/2}}}$$

Now if the star image is (a) Gaussian or (b) typical of those experimentally seen,

$$\left| \frac{\partial \text{MTF}}{\partial K} \right|_{k=k_{1/2}} \cong \frac{1}{k_{1/2}} \text{MTF}(0)$$

and we have

$$\begin{aligned} \frac{\sigma(\theta_s)}{\theta_s} &\cong \frac{\sigma(k_{1/2})}{k_{1/2}} \cong \frac{\sigma_M(k_{1/2})}{\text{MTF}(0)} \\ &= \sqrt{K/2} \frac{\sqrt{D_I(t_o)}}{D_I(t_o)} \\ &= \sqrt{\frac{K}{2D_I(t_o)}} \\ &= \frac{1}{\sqrt{2}} \sqrt{\frac{1}{\tau_F \int dx dy I(x, y)}} \equiv \frac{1}{\sqrt{2 \tau_F \bar{I}}} \end{aligned}$$

APPENDIX D SEEING MONITOR CALIBRATION PROCEDURES AND SUPPORT DATA

A. SEEING METER CALIBRATION

The seeing meter calibration is accomplished by measuring the time at which the stop pulse occurs relative to the start of the sector. The stop pulse is generated when the MTF reaches half of its initial value and this time is directly related to the spatial frequency $k = (\lambda^{-1})$ of the reticle wheel sector on which the light is focused at the time the stop pulse occurs. The seeing angle θ^S is found from the relationship

$$\theta^S(\text{sec}) = \frac{0.37k_{\frac{1}{2}}^{-1}}{F \times 4.8 \times 10^{-6}} \quad (1)$$

where F is the effective focal length of the telescope at the magnification setting used. For the three magnification settings the effective focal length of the telescope is $F_t M_i$ (for the $B = 30$ telescope with Barlow lens $F_t = 741$ in) where M is the magnification of the Seeing Monitor for magnification range i .

Magnification Range	M_i	F
0.1 - 2 $\overline{\text{sec}}$	3.67	2720 in
0.3 - 6 $\overline{\text{sec}}$	1.39	1030 in
0.5 - 10 $\overline{\text{sec}}$	0.745	552 in

The magnification values M_i are obtained by placing an object of known size at the position of the telescope focus P_1 (Fig. D-1) at the entrance to the Seeing Monitor just prior to the field lens L_A . A back illuminated grid of known spacing is a convenient object to use for this purpose as is a pair of calipers. An illuminated scale or an aperture of known size can also be used. The image of this object is projected on a screen that is located at the equivalent position of the reticle wheel. The size of the image is then measured on the screen directly or alternatively, a photograph of the object can be taken by placing a film at the image plane and subsequently measuring the size of the image on the film.

Calibration of the seeing meters is accomplished in the following manner. An $f/15.4$ lens mounted on a translatable mount focuses light from a collimated source at P_1 . A dual beam oscilloscope triggered by the 1 kHz reference pulse is set up so that the PM outputs are conveniently displayed (100 $\mu\text{sec}/\text{div}$). The transverse position of the input beam is adjusted so that the leading edges of the chopping patterns occur at the same time (on axis condition) and the sweep delay is adjusted so that the first dark-to-light transition occurs at the extreme left hand edge of the oscilloscope reticle pattern. Next, the stop pulses for each channel are displayed on the oscilloscope and the time of occurrence of each stop pulse is measured relative to the leading edge of its corresponding chopping pattern. The corresponding seeing meter reading is also noted for each channel.

The external focusing lens is moved in the Z-direction a known amount, defocusing the incident light, and stop pulse time and seeing meter reading are again noted, and so on over a convenient range of values. This series of measurements is carried out for all three magnification settings of the lens turret.

It now remains to convert stop pulse time to spatial frequency or spatial wavelength on the reticle wheel and hence to θ^S via equation (1). The angular spacing for the opaque zones of the reticle wheel are given in Table D-1. The full square wave cycle of a given zone (opaque plus clear) is defined from the start of one opaque zone to the start of the next opaque zone. The wavelength k^{-1} of a square wave cycle is given by $r\Delta\theta$ where $\Delta\theta$ is the angular extent of the zone and r is the distance from the center of the reticle wheel to the point where the spot is focused on the chopping pattern ($r = 2.7$ in for on-axis light). Since the angular rate of the wheel is known (1 msec per sector) the particular spatial frequency when the stop pulse occurs can be easily obtained. Figure D-1 gives inverse spatial frequency versus time from the beginning of the sector for $r = 2.7$ in. The line in Fig. D-1 is drawn continuous where in fact it should be more correctly shown as a series of steps having discrete values of k^{-1} . Nevertheless, for the right hand side of the graph it is a good approximation. For greater accuracy Table D-1 should be used.

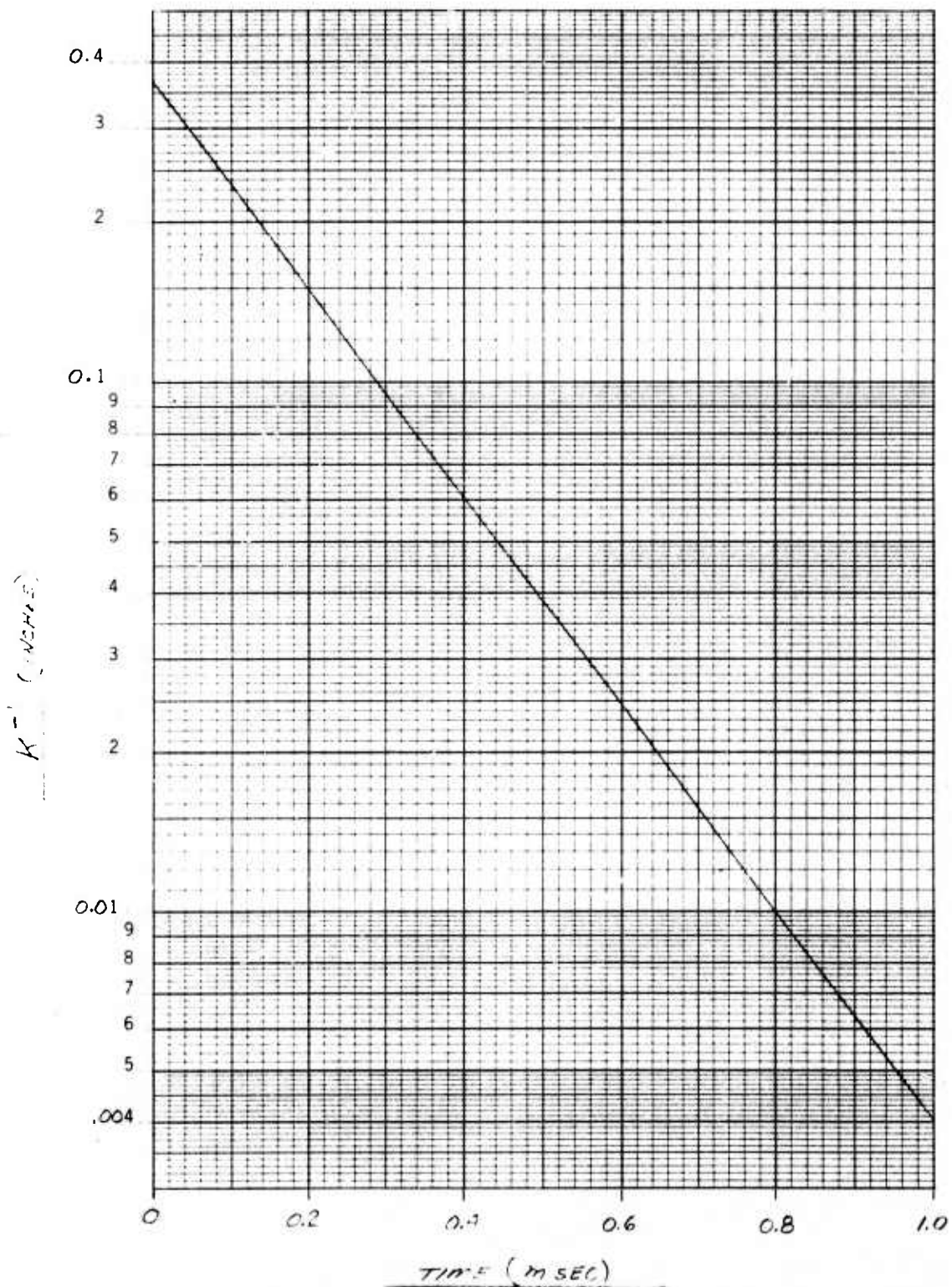


Figure D-1. Chopping pattern spatial wavelength versus time.

TABLE D-1 - RETICLE WHEEL PATTERN, OPAQUE ZONES

Zone Number	Angular Extent, Degrees	Zone Number	Angular Extent, Degrees
1	0.000 - 3.000	39	25.653 - 25.737
2	6.043 - 7.557	40	25.819 - 25.900
3	8.711 - 9.816	41	25.980 - 26.059
4	10.700 - 11.489	42	26.137 - 26.214
5	12.188 - 12.819	43	26.290 - 26.365
6	13.394 - 13.923	44	26.440 - 26.513
7	14.411 - 14.866	45	26.586 - 26.658
8	15.291 - 15.689	46	26.730 - 26.800
9	16.065 - 16.420	47	26.870 - 26.939
10	16.757 - 17.077	48	27.007 - 27.074
11	17.382 - 17.674	49	27.141 - 27.207
12	17.953 - 18.220	50	27.273 - 27.338
13	18.477 - 18.724	51	27.402 - 27.465
14	18.963 - 19.192	52	27.528 - 27.591
15	19.414 - 19.629	53	27.653 - 27.714
16	19.836 - 20.038	54	27.774 - 27.834
17	20.233 - 20.423	55	27.894 - 27.953
18	20.607 - 20.786	56	28.011 - 28.069
19	20.960 - 21.130	57	28.127 - 28.183
20	21.295 - 21.457	58	28.240 - 28.296
21	21.614 - 21.768	59	28.351 - 28.406
22	21.918 - 22.065	60	28.461 - 28.515
23	22.208 - 22.349	61	28.568 - 28.622
24	22.486 - 22.621	62	28.674 - 28.727
25	22.753 - 22.882	63	28.778 - 28.830
26	23.009 - 23.133	64	28.881 - 28.932
27	23.255 - 23.375	65	28.982 - 29.032
28	23.492 - 23.608	66	29.081 - 29.131
29	23.721 - 23.833	67	29.179 - 29.228
30	23.942 - 24.050	68	29.276 - 29.324
31	24.156 - 24.261	69	29.371 - 29.418
32	24.363 - 24.465	70	29.465 - 29.511
33	24.564 - 24.662	71	29.557 - 29.603
34	24.759 - 24.854	72	29.648 - 29.693
35	24.948 - 25.040	73	29.738 - 29.782
36	25.132 - 25.222	74	29.827 - 29.870
37	25.310 - 25.398	75	29.914 - 29.957
38	25.484 - 25.569		

For example, say the stop pulse occurs 850 μsec after the start of the sector. At 30° per 1000 μsec the wheel would have rotated 25.50° by the time the stop pulse was generated. Referring to Table D-1 we see that 25.50° occurs in Zone #38 whose angular extent is 0.169° ($25.653^\circ - 25.484^\circ$). The center of the chopping pattern occurs at a radius of 2.7 in from the center of the wheel and hence the spatial wavelength k^{-1} of Zone #38 is $r\Delta\theta = 2.7 \times 0.169\pi/180 = 0.00796$ in. This value of k^{-1} then yields θ^S via equation (1).

The seeing meter calibration curves are given in Fig. D-2. Here seeing angle θ^S is plotted versus seeing meter reading. For the magnification settings 0.3-6 $\overline{\text{sec}}$ and 0.5-10 $\overline{\text{sec}}$ two different curves are presented. The solid curves are those obtained from the raw data generated by the technique described above (i.e. displacing the focus and measuring stop pulse time and converting stop pulse time to seeing angle via equation (1)). The dashed curves are curves that have been shifted to allow internal agreement for all the magnification settings taking the 0.1-2 $\overline{\text{sec}}$ range as a standard. The rationale for adjusting the calibration curves is discussed in the following paragraphs.

For a given displacement of the external focus carried out in the calibration procedure (i.e. for a given spot size at the entrance of the Seeing Monitor) the instrument should yield the same value for seeing angle independent of magnification range setting. However it was found (see Fig. D-3) that the values obtained for seeing angle are not quite the same under conditions of external focusing for which different magnification ranges are expected to agree. (The reason that the curves disagree for small displacements is believed to be due to lack of diffraction limited performance of L_2 and L_3 which employ larger apertures than any of the other lenses in the Seeing Monitor.) This effect is illustrated in Fig. D-3 which shows θ^S (obtained from stop pulse time measurements) plotted versus the displacement of the external focus for all three magnification settings. Here we see that in the practical operating range for the different settings (shown in the figure) the data points fall within $\pm 10\%$ of each other. The solid lines

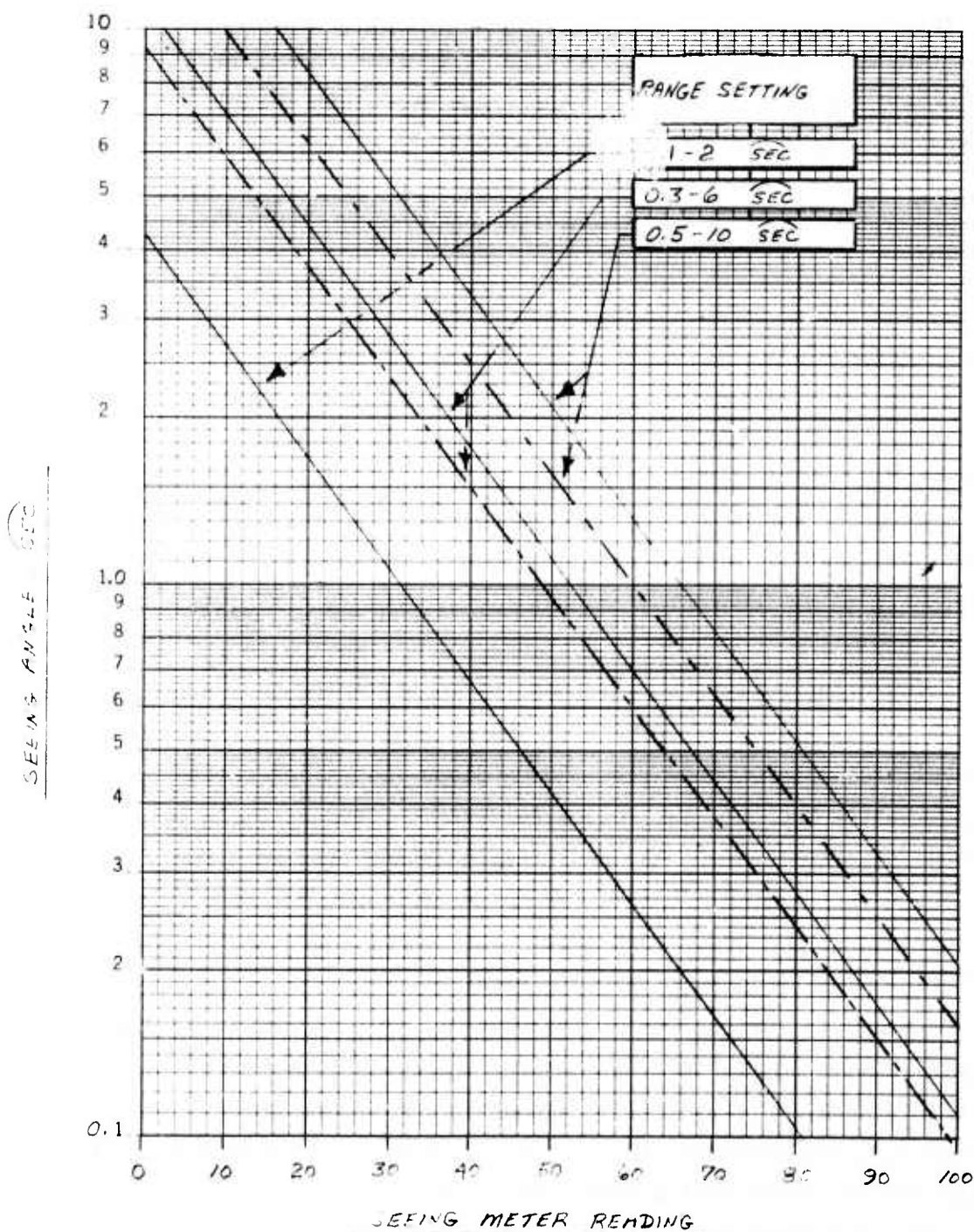


Figure D-2. Seeing meter calibration curves.

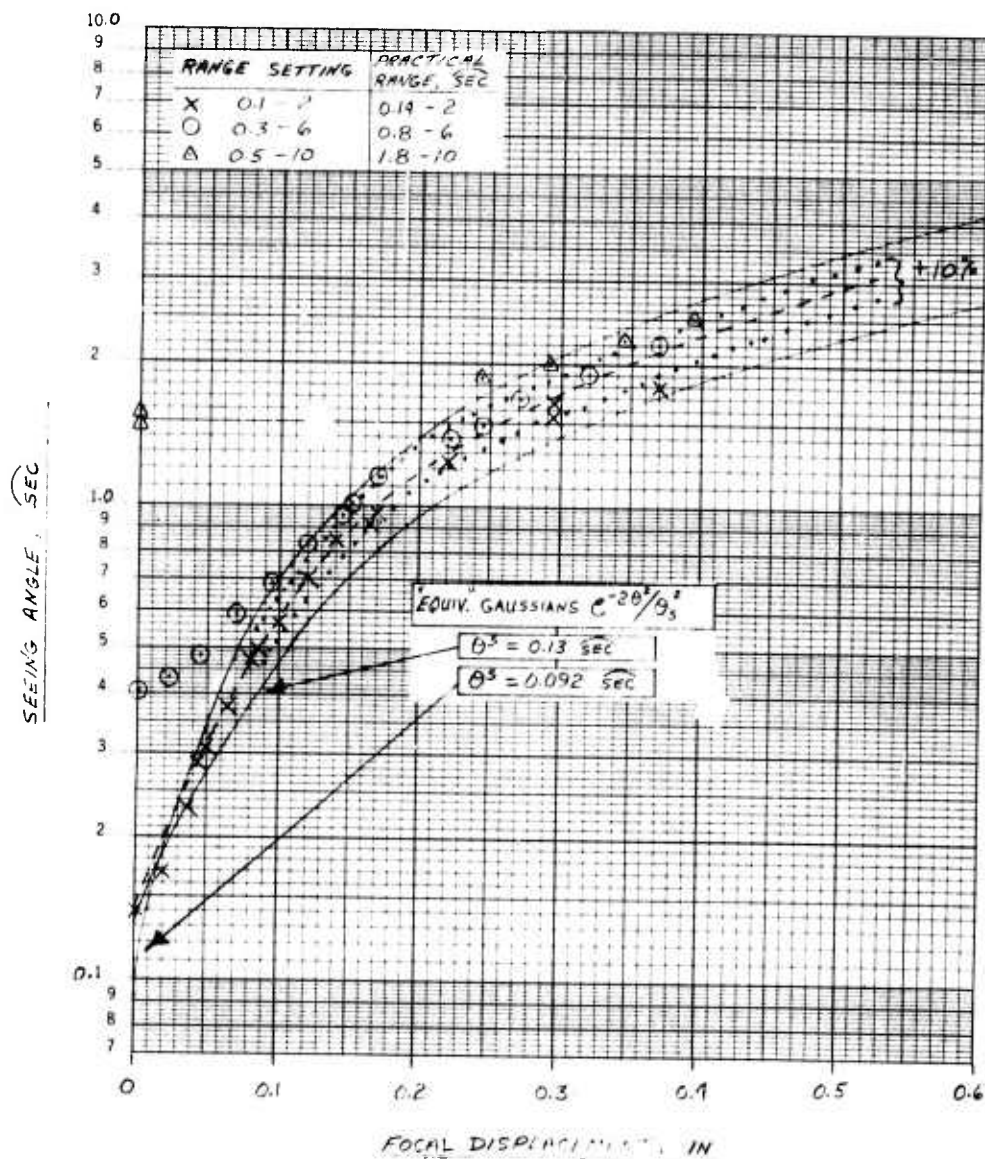


Figure D-3. Seeing angle versus focal displacement.

in Fig. D-3 indicate calculated seeing angle versus displacement for two different gaussian beams of intensity profile $I(\theta) = \exp[-2\theta^2/\theta_s^2]$ for comparison and the dotted curves show $\pm 10\%$ points about the curve drawn through the data points. While the disagreement in the data from the different magnification ranges is not large the data points can be made to fall much more closely to each other by shifting them in the manner described above. This is illustrated in Fig. D-4 in which the triangles and circles have been shifted each set by a constant fraction.

This shift in data points amounts to a reassignment of the magnification values for the settings 0.3-6 $\overline{\text{sec}}$ and 0.5-10 $\overline{\text{sec}}$ and hence to a reassignment of effective focal lengths. It is conceivable that the method used to measure the system magnification as described earlier in this section (i.e. imaging of an extended object) would give different values when used for small objects (essentially on-axis). The reason for the small discrepancy is not evident at this time but is pointed out here for possible future characterization in more detail. Since the size of the spot on the reticle wheel for a given lens turret setting is directly related to the system magnification for that setting the most direct way to obtain a magnification measurement for on-axis operation would be to place a photographic plate at the equivalent position of the reticle wheel and expose the plate using different focused spot sizes at the input to the Seeing Monitor. A comparison of densitometer scans of the images for different lens turret settings then will yield an additional measure of the system magnification values.

A comparison of measured magnification (via the extended object method) and adjusted magnification (via normalization to the 0.1-2 $\overline{\text{sec}}$ setting) are given below.

Magnification Range	Magnification	
	Measured	Adjusted
0.1-2	3.67	3.67
0.3-6	1.39	1.62
0.5-10	0.745	0.98

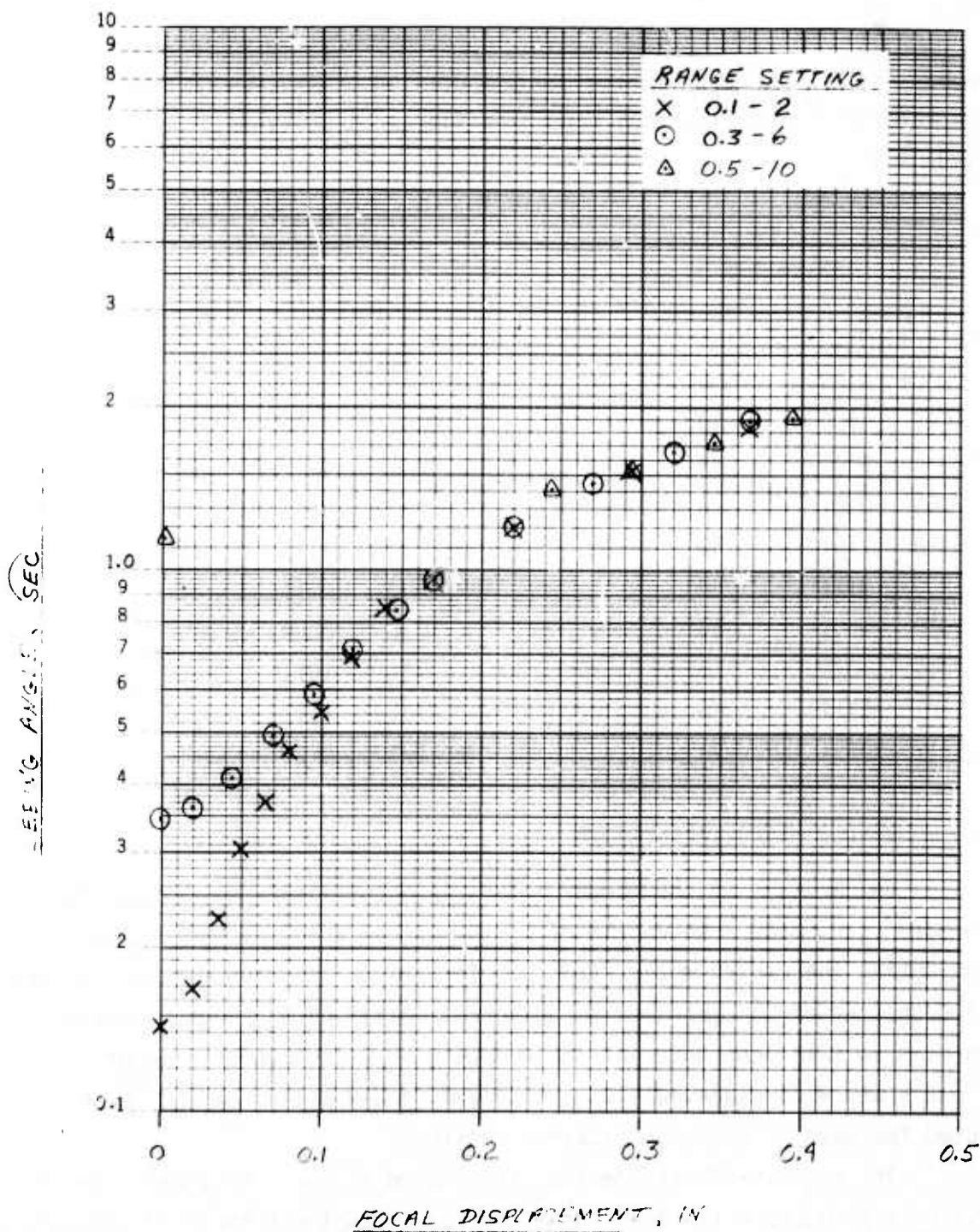


Figure D-4. Seeing angle versus displacement - points adjusted for ranges 0.3 to 6 sec and 0.5 to 10 sec.

B. CALIBRATION OF SEEING LIGHTS

The lights above each seeing meter represent an eight bit binary number that is directly related to the reading on the seeing meters. The relationship between the meter reading and the lights is given in Table D-2.

Table D-2

Channel 1			Channel 2		
Light (On = 1, Off = 0)		Meter	Light (On = 1, Off = 0)		Meter
0000	0000	0	0000	0000	0
0001	1100	10	0001	1100	10
0011	0111	20	0011	0111	20
0101	0001	30	0101	0001	30
0110	1101	40	0110	1100	40
1000	0111	50	1000	0111	50
1010	0001	60	1010	0000	60
1011	1011	70	1011	1011	70
1101	0111	80	1101	1111	80
1111	0011	90	1111	0111	90

C. WANDER METER CALIBRATION

Calibration of the wander meters is accomplished by displacing a focused star image a known amount at the entrance to the Seeing Monitor and noting the wander meter reading. Initial calibration was carried out at Hughes Research Laboratories using collimated 6328 Å light focused through an f/15 lens that was mounted on an x-y-z micrometer mount. Known x and y displacements were made and wander meter readings were noted for each of the magnification settings.

The angular displacement θ_w is related to the x or y displacement via $\theta_w = \frac{\Delta x}{F}$ where F is taken to be the focal length of the B=30 telescope, 741 in.

Plots of wander meter reading versus angular displacement are shown in Figures D-5 to D-7. The meter calibration values are summarized below.

Magnification Setting	Wander Meter Cal'bration (arc sec/div)
0.1 - 2	0.096
0.3 - 6	0.27
0.5 - 10	0.45

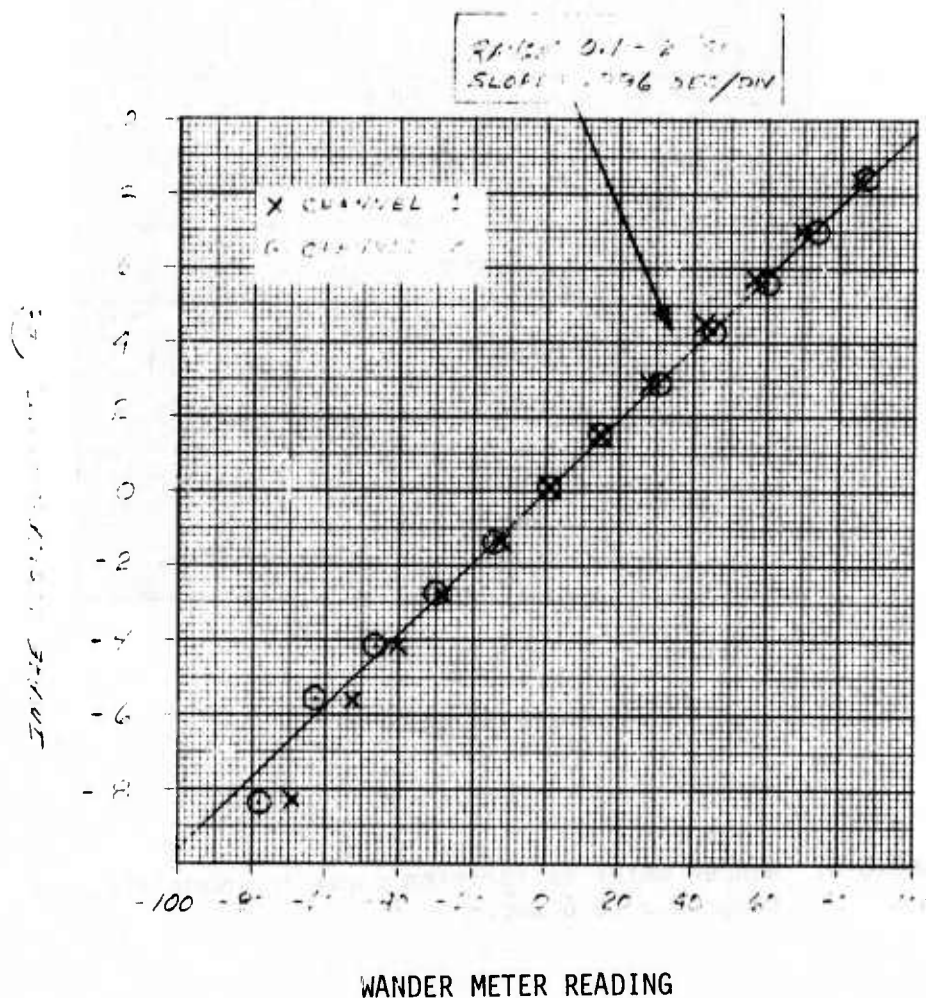


Figure D-5. Wander meter calibration curve for magnification range 0.1 to 2 sec.

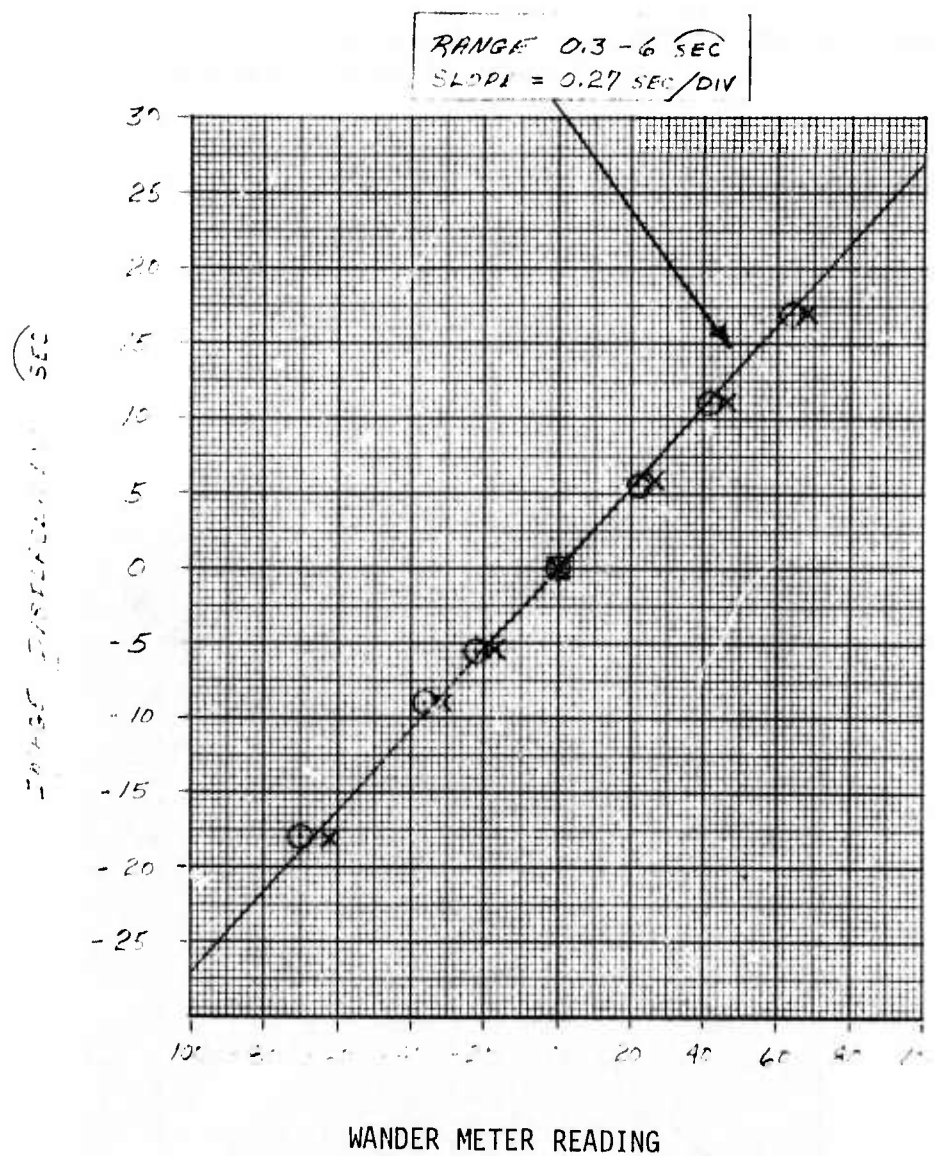


Figure D-6. Wander meter calibration curve for magnification range 0.3 to 6 sec.

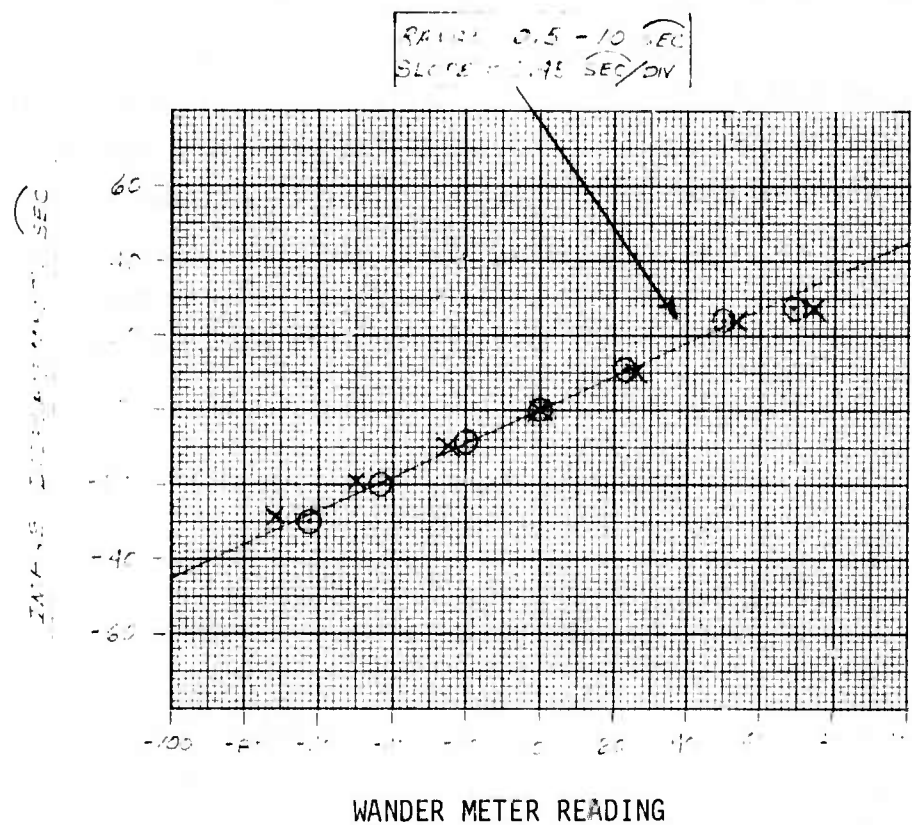


Figure D-7. Wander meter calibration curve for magnification range 0.5 to 10 sec.

D. CALIBRATION OF WANDER LIGHTS

The wander lights located above each wander meter display a digital count that represents the position of the image in the field of view. The binary number that is displayed is generated for an eight bit counter that starts counting when the start pulse is generated and stops when the slot reference pulse arrives. The relation between the wander meter reading and the wander lights for each channel is given in Table D-3. To generate the values in this table, the image was moved in the field of view and the binary numbers for each channel were recorded for each ten-unit reading on the corresponding wander meter.

TABLE D-3
Wander Lights Calibration

Wander Meter Reading	LED Binary Number (ON = 1, OFF = 0)	
	Channel 1	Channel 2
-100	1101 1101	1101 1111
-90	1101 1100	1101 1101
-80	1101 1010	1101 1011
-70	1101 1001	1101 1010
-60	1101 0111	1101 1000
-50	1101 0110	1101 0110
-40	1101 0100	1101 0100
-30	1101 0011	1101 0010
-20	1101 0001	1101 0000
-10	1101 0000	1100 1111
0	1100 1110	1100 1101
10	1100 1101	1100 1011
20	1100 1011	1100 1001
30	1100 1010	1100 0111
40	1100 1000	1100 0101
50	1100 0111	1100 0100
60	1100 0101	1100 0010
70	1100 0100	1100 0000
80	1100 0010	1011 1110
90	1100 0001	1011 1101
100	1011 1111	1011 1100

E. CALIBRATION OF ORIENTATION LIGHTS

The angular position of the dove prism is sensed by a 6 bit shaft encoder. Hence, the full 2π image rotation is divided into 64 angular increments, each value of which is indicated on the 6 orientation lights on the control panel. The values of the 6 digit grey coded number are given in Table D-4 starting at 0° and continuing for clockwise rotation.

TABLE D-4
Dove Prism Binary Grey Code Calibration
(1 = ON, 0 = OFF)

Image Orientation (degrees)	Orientation Lights	Image Orientation (degrees)	Orientation Lights
0	110 011	180.0	000 011
5.6	111 011	185.6	001 011
11.25	111 010	191.3	001 010
16.9	111 000	196.9	001 000
22.5	111 001	202.5	001 001
28.1	111 101	208.1	001 101
33.8	111 100	213.8	001 100
39.4	111 110	219.4	001 110
45.0	111 111	225.0	001 111
50.6	011 111	230.6	101 111
56.3	011 110	236.3	101 110
61.9	011 100	241.9	101 100
67.5	011 101	247.5	101 101
73.1	011 001	253.1	101 001
78.8	011 000	258.8	101 000
84.4	011 010	264.4	101 010
90.0	011 011	270.0	101 011
95.6	010 011	275.6	100 011
101.3	010 010	281.2	100 010
106.9	010 000	286.9	100 000
112.5	010 001	292.5	100 001
118.1	010 101	298.1	100 101
123.8	010 100	303.8	100 100
129.4	010 110	309.4	100 110
135.0	010 111	315.0	100 111
140.6	000 111	320.6	110 111
146.3	000 110	326.3	110 110
151.9	000 100	331.9	110 100
157.5	000 101	337.5	110 101
163.1	000 001	343.1	110 001
168.8	000 000	348.8	110 000
174.4	000 010	354.4	110 010

F. FIELD OF VIEW MEASUREMENT

The field of view at each magnification setting was measured by translating the spot focused at the entrance to the Seeing Monitor while viewing the reticle wheel chopping pattern on an oscilloscope (PM output BNC). The point at which the chopping pattern was seen to degrade was taken to be the limit of the FOV. The distance between extremes was measured and divided by 741 in, the focal length of the B=30 telescope to give the following fields of view.

Magnification Setting	Field of View, arc sec
0.1 - 2	28
0.3 - 6	70
0.5 - 10	130

G. OPTICAL TRANSMISSION MEASUREMENTS

A He-Ne laser and power meter were used to measure the optical transmission of the Seeing Monitor at different points along the optical train and thence to assign optical efficiencies to the different components. The total optical efficiency measured up to the position of the reticle wheel is 0.36 (0.18 for each channel).

The breakdown for the different elements is as follows:

Element	Optical Efficiency
Lenses	0.96
Mirrors	0.90
Beam Splitter	0.90 (total)
Dove Prism	0.82

H. BAND PASS FILTERS

Provision has been made for the use of different band pass filters to be inserted in the optical path between the reticle wheel and the photomultiplier tubes. These filters are contained in spring loaded holders that can be securely and reproducibly located. Ten (10) filter holders have been provided; eight (8) of these (4 pair) contain band pass filters and two are opaque (to be used for blocking the light at the photomultiplier if necessary). The band pass filters have transmission maxima centered around $\sim 6000 \text{ \AA}$, peak transmittance between 80 and 85%, and widths (FWHM) of 640, 900, 1200, and 1800 \AA . The spectral transmission curves of the band pass filters are shown in Figs. D-8 through D-11.

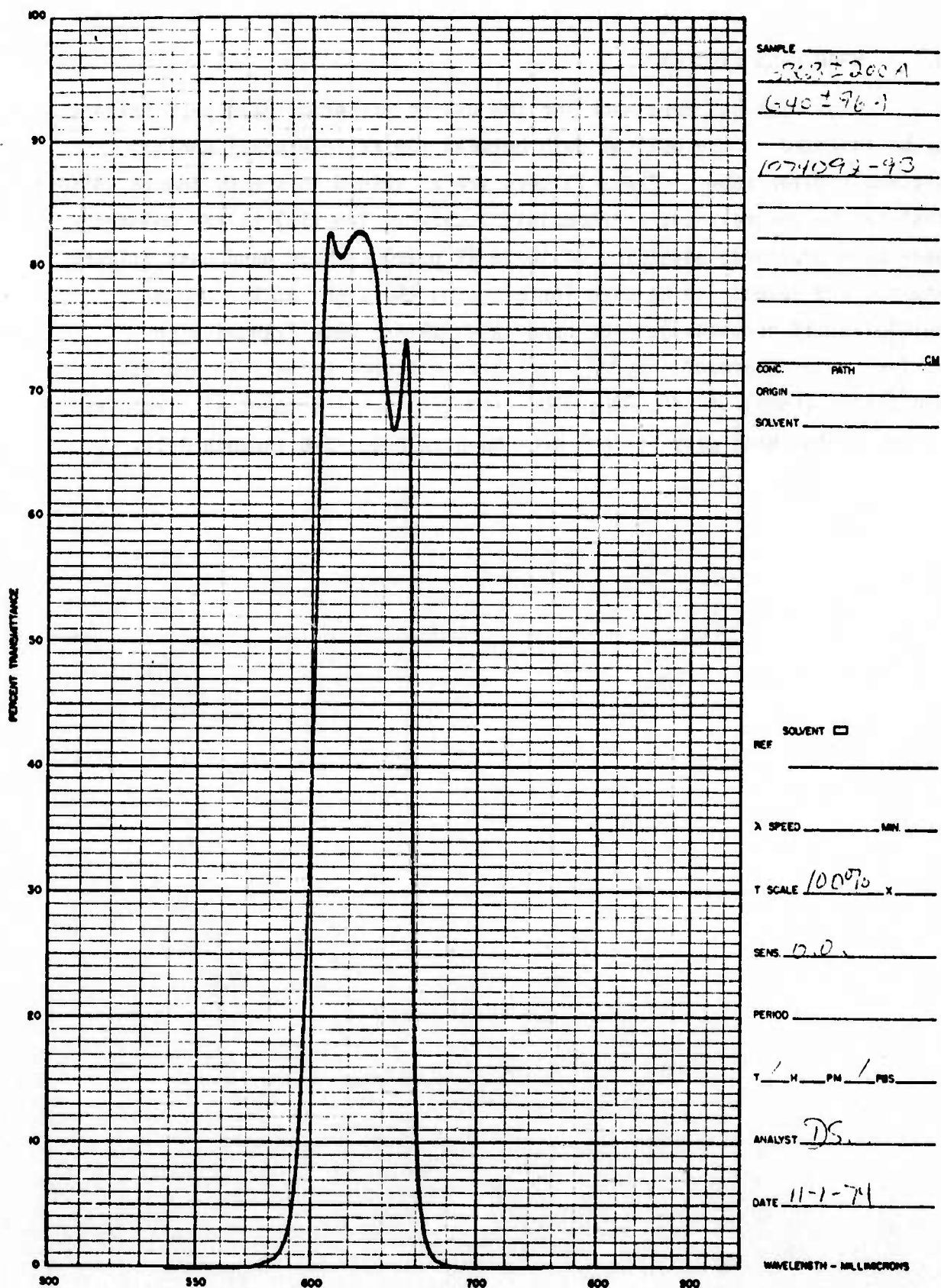


Figure D-8. Spectral transmission curve for 640 Å filter.

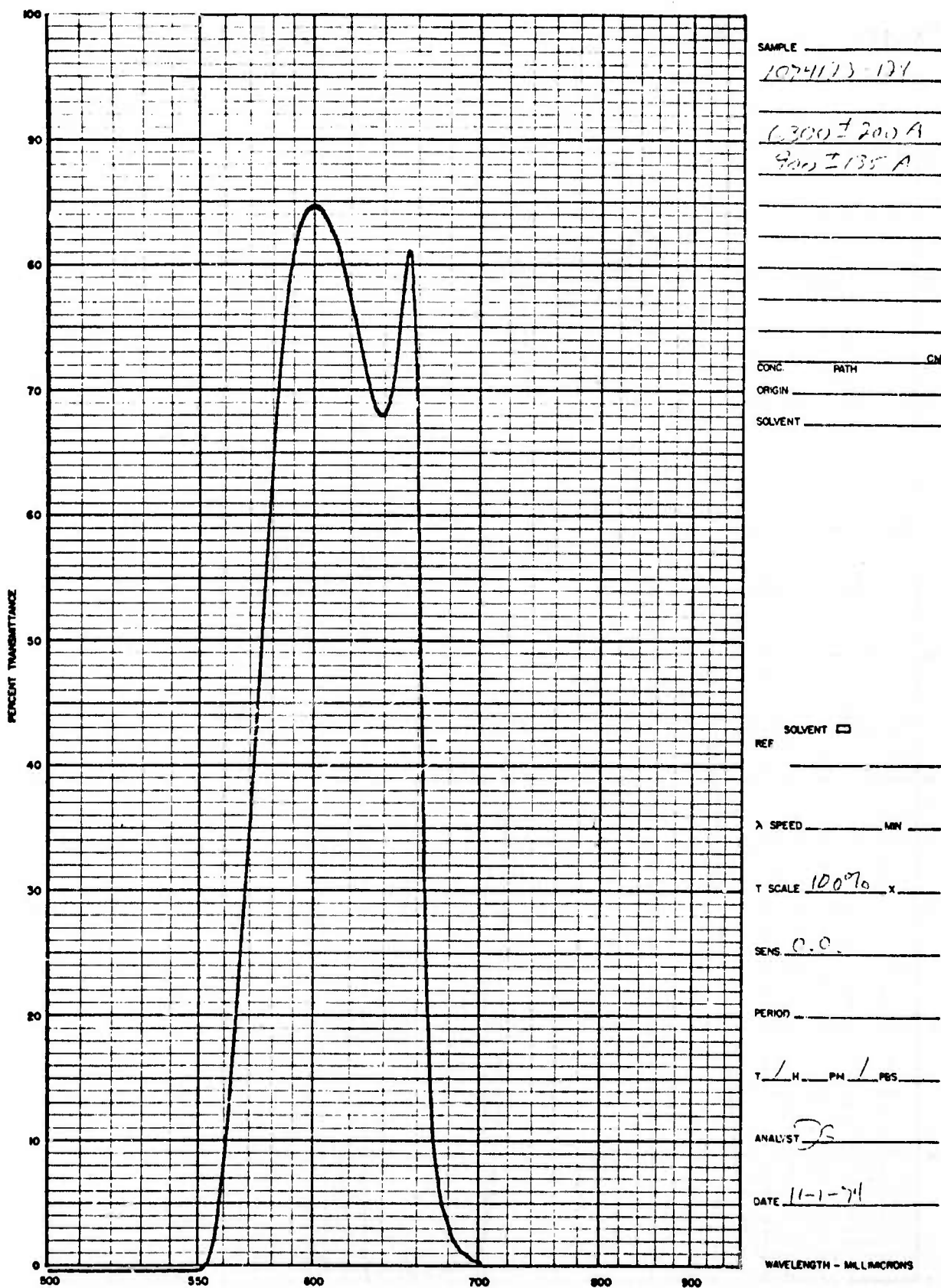


Figure D-9. Spectral transmission curve for 900 Å filter.

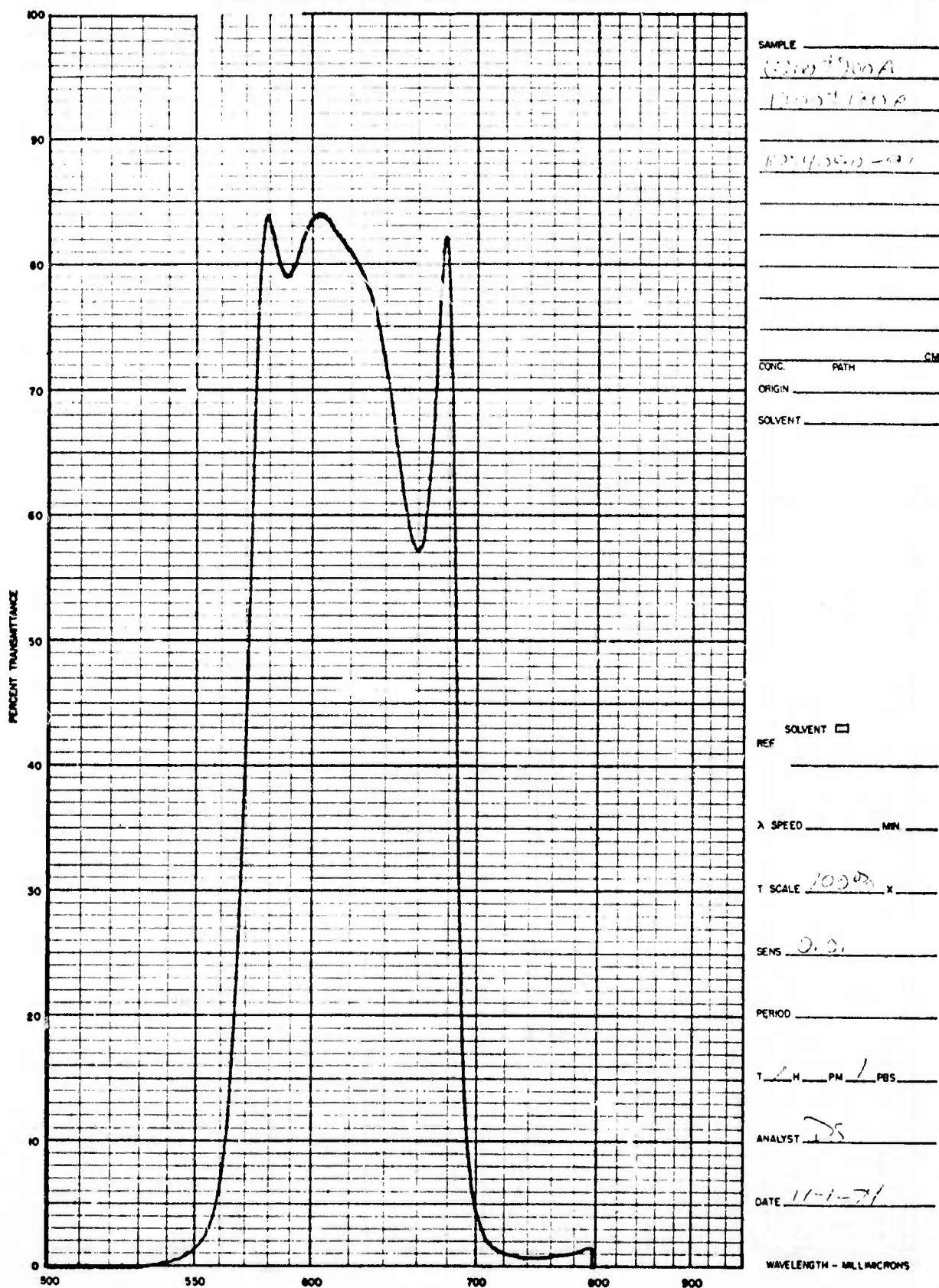


Figure D-10. Spectral transmission curve for 1200 Å filter.

APPENDIX E

NOISE-EQUIVALENT QUANTUM EFFICIENCY MEASUREMENTS

The noise-equivalent quantum efficiency of photomultiplier PMT 2 was determined by measuring the fluctuations on the photomultiplier output signal. The measurement was accomplished at four light levels, spanning about four orders of magnitude. In all four cases, the result was about 4% noise-equivalent quantum efficiency. This value is 0.3 times the quoted cathode quantum efficiency of 13%.

Table E-1 lists the experimental conditions, the $\sigma(e)/e$ as measured from photographs of an oscilloscope trace, and the resulting noise-equivalent quantum efficiency.

The light source was a 6328 Å laser with a pinhole for attenuation and a lens and iris to form a collimated beam. Different filters were placed in this beam to provide different levels of illumination. The filters were the metal film on glass type. The power at the photomultiplier cathode was 0.0309 μ W as measured with a United Detector Technology Model 40X Opto-Meter. The filter attenuation factors were calibrated using the same meter. The tube was operated at the indicated cathode (and dynode-chain) voltages. These were selected to give anode currents of 1 to 10 μ A.

The photomultiplier outputs were amplified as usual by the onboard electronics preamp, mid amp, and post amp and the result is shown in Figs. 1a - 1d. In each figure the upper trace shows the reticle wheel chopping pattern. The lower trace is an expanded version of the first light zone shown on the upper trace:

PRECEDING PAGE BLANK-NOT FILMED

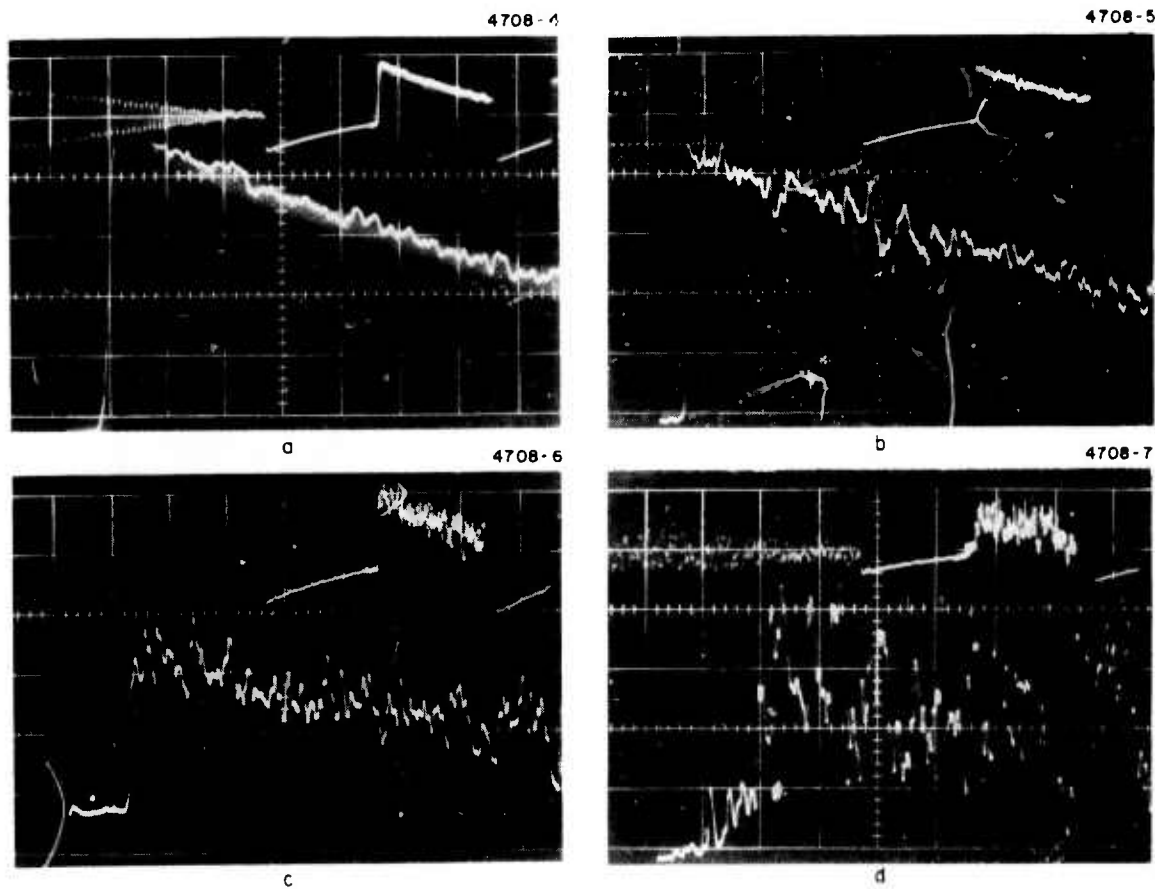
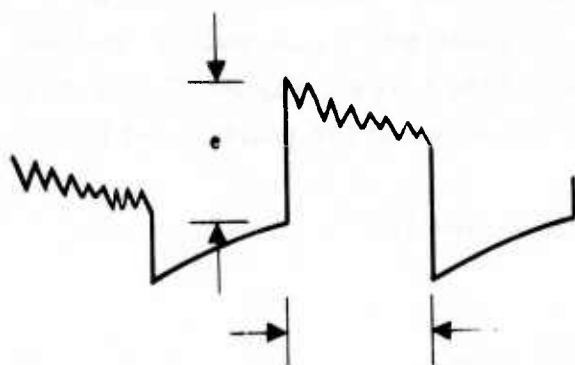


Figure E-1. Photomultiplier outputs.



This zone is lower trace.

$\sigma(e)$ was determined by quantizing the lower trace at two-millimeter intervals. If these quantized values are e_i then

$$\sigma(e) \equiv \left(\frac{1}{N} \sum_{i=1}^N (e_i - e_0)^2 - \left[\frac{1}{N} \sum_{i=1}^N (e_i - e_0) \right]^2 \right)^{1/2}$$

The average e_0 was automatically subtracted by passing a straight line through the lower trace and reading $e_i - e_0$, i.e., the distance from the straight line.

Table E-2 gives the values of $e_i - e_0$ for each of the four cases. The numbers are given with one unit equalling 2.5 millimeters.

The value of e is also read off the lower trace as the height of the dark-to-light transition. For the four cases these are

Case	1a	1b	1c	1d
e	22.0	19.5	10.8	11.2

The ratio $\sigma(e)/e$ is given in Table E-1.

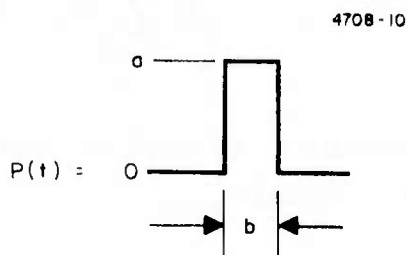
The noise-equivalent time constant of the circuits between the photomultiplier and the scope trace was calculated from its experimentally-measured point-spread function: under very low light

level conditions single pulses were observed. They were of varying heights but all had the same time dependence. The shape of these pulses is the point-spread function. A pulse was quantized by reading points from a photograph of its oscilloscope trace. Figure E-2 is this photograph. Figure E-3 is a re-plotted curve of the points read from Fig. E-2.

The noise-equivalent integration time is

$$\tau = \frac{(\int P(t) dt)}{\int P^2(t) dt}$$

This above equation is easily obtained from probability theory. (In fact, if



then

$$\tau = \frac{(ab)^2}{a^2 b} = b \text{ as expected})$$

From the data of Fig. E-3, then we obtain $\tau = 1.395$ microseconds. The noise-equivalent photoelectrons per second is

$$n_p = \frac{1}{\tau} \left(\frac{e}{\sigma(e)} \right)^2$$

This n_p is given in Table E-1. Finally, on the last line of Table E-1 the noise equivalent quantum efficiency n_p/n is tabulated.

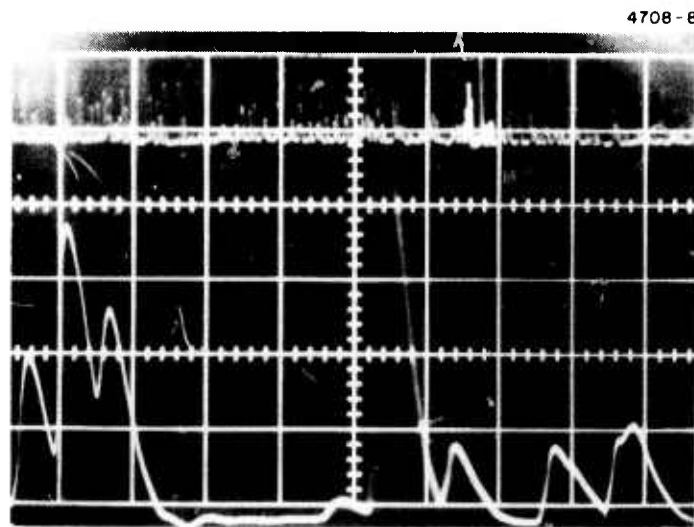


Figure E-2. Individual pulses from photomultiplier.

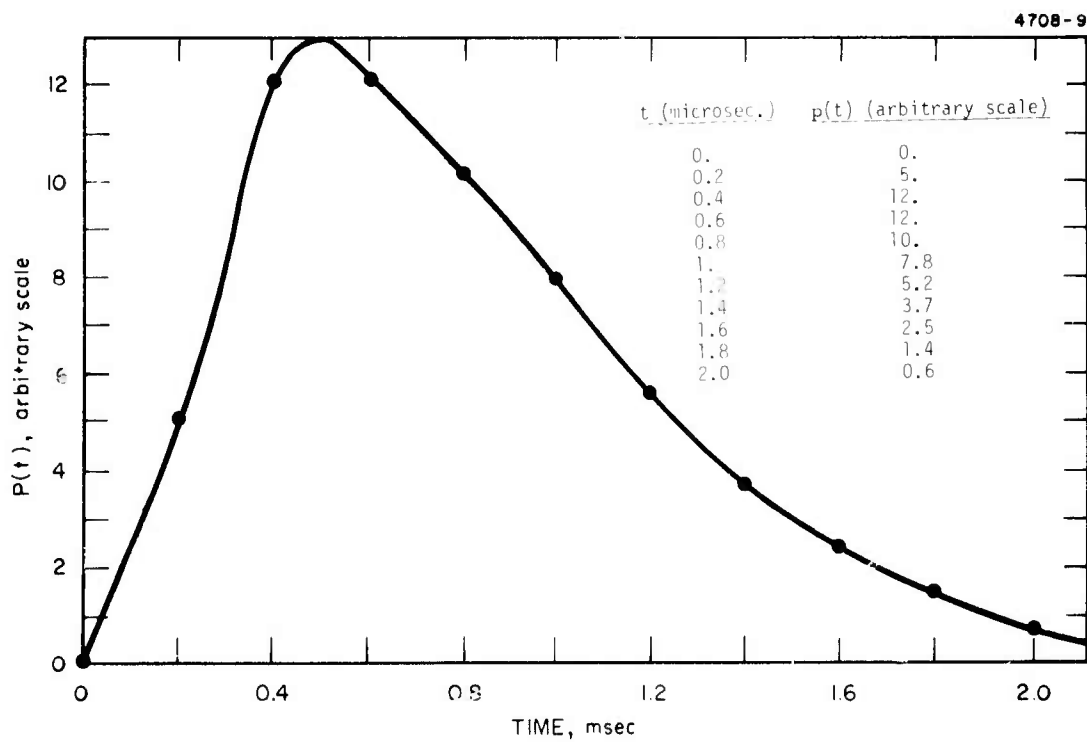


Figure E-3. Point-spread function.

Table E-1

Light Wavelength (Angstrom)	6328	6328	6328	6328
Beam Power (Microwatts)	0.0309	0.0309	0.0309	0.0309
Filter - Nominal Value	None	ND1	ND2	ND2 + ND. 7
Actual filter attenuation factor	1.000	0.095	0.0105	0.000210
Cathode and dynode chain voltage	-470 V	-570	-770	-770
Photograph number (Fig. E-1)	a	b	c	d
Incident photons/sec, n	0.98×10^{11}	0.93×10^{10}	1.03×10^9	2.10×10^8
$\sigma(e)/e$ as measured from Fig. E-1	0.013	0.046	0.129	0.30
Noise-equivalent photoelectrons per second n_p	4.24×10^9	3.38×10^8	4.20×10^7	7.96×10^6
Noise-equivalent quantum efficiency n_p/n at 6328 Å	0.043	0.036	0.042	0.038

Table E-2. Values of $e_i - e_o$

Case			
1a	1b	1c	1d
0	0.1	2.0	+4.0
0	0.4	2.0	+5
-0.2	0.6	0.8	-1
-0.1	-0.8	-1.0	+5
-0.2	0.4	2.0	0
0.4	-0.9	0.7	0
0.6	-2.2	0	+4
0.3	0.3	2.4	-3
-0.4	0.25	-0.9	-2.7
0	0.1	0.7	+3.2
-0.2	-0.6	-0.8	0
-0.15	0	-0.3	-4
0.1	0.5	-2.0	-3.5
0	0	-1.0	-2
-0.4	1.1	-1.2	-1.5
-0.4	-1.2	-0.6	-1.3
0.3	-3.1	0	-2.2
1	1.0	1.2	+4.0
0.6	-0.5	0	-3.2
0	-1.7	1.2	+2.7
-0.1	0	-0.2	+1.8
0.5	-1.0	1.0	-2.5
-0.1	0.1	2.0	+3.0
0.1	-0.6	0	-1.0
-0.1	-0.1	0.4	-4.0
-0.2	0	0.5	-7.0
-0.4	-0.9	1.1	4.0
0.1	-0.2	2.2	0
0	0	-2.0	2.2
0.6	-0.6	0	3.0
-0.3	-0.7	-2.4	6.2
0	-0.2	1.6	-3.0
0	-0.6	2.0	-5.0
0.5	-1.6	1.0	
	1.9	1.0	
		-3.2	
Resulting $\sigma(e)$			
0.291	0.888	1.39	3.00

APPENDIX F

ALIGNMENT TECHNIQUE FOR PRIMS TRANSMITTER

Various alignment studies were performed during this program. The results of these studies are presented below.

In this experiment the wavelength was 6943 \AA and the detector aperture was 0.005 in. The angle required for heterodyne photomixing was $7 \times 10^{-4} \text{ rad}$. By using a 30 in. (76 cm) focal length lens to bring the beams to a common focus, it was found to be possible to perform final angular alignment to within this specification. Specifically the input beam diameter was 3 mm and the estimated focal spot size for either polarization beam was of the order of $1.4 \times 10^{-4} \text{ m}$. The angle subtended by the spot at the focal distance (76 cm) was of the order of $2 \times 10^{-4} \text{ rad}$. By alternately blocking one polarization (P_1) and adjusting the mirrors for the other polarization (P_2) the system was brought into alignment visually if the spots were made to overlay.

Final alignment for a space object experiment will require alignment within 1 m at a range of 400 km or $2.5 \times 10^{-6} \text{ rad}$. If a pair of 2 cm diameter laser beams are passed into a photomultiplier and the beam angles are adjusted for optimum photomixing then the angular accuracy of alignment will be of the order of $4 \times 10^{-6} \text{ rad}$. When the beam is then passed through a telescope and recollimated to a larger diameter for transmission to a target, the angular misalignment of the two polarizations will be reduced by the telescope magnification (for the 24 in. beam director the reduction will be about a factor of 30).

Initial alignment, however, has proven to be the most difficult part of the experiment and special techniques have been developed to accomplish this task. Two additional components, a $\lambda/4$ waveplate oriented at 45° , and a reflector are used to accomplish the initial alignment (see Fig. 1). These components were placed between the

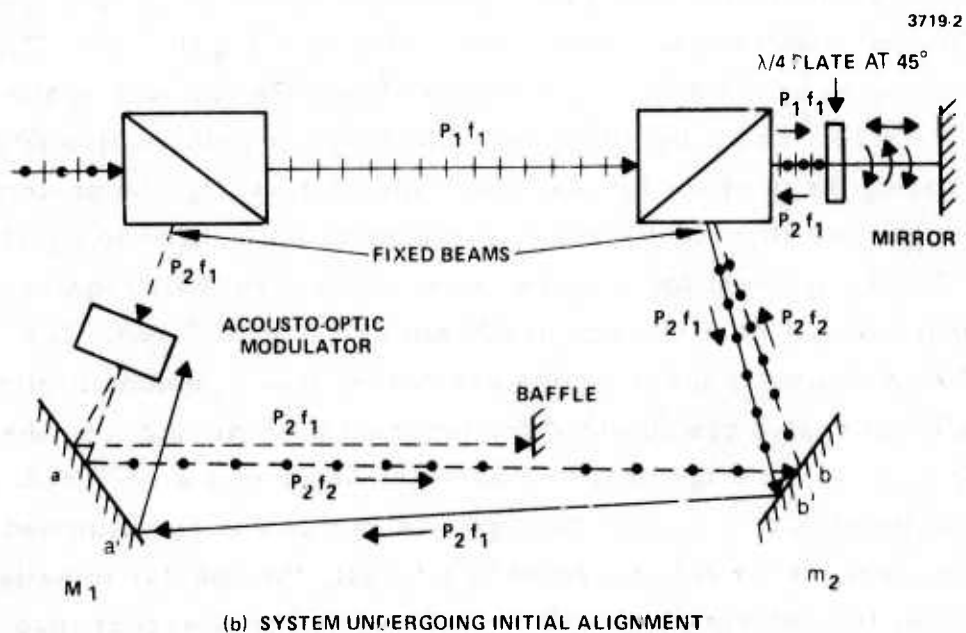
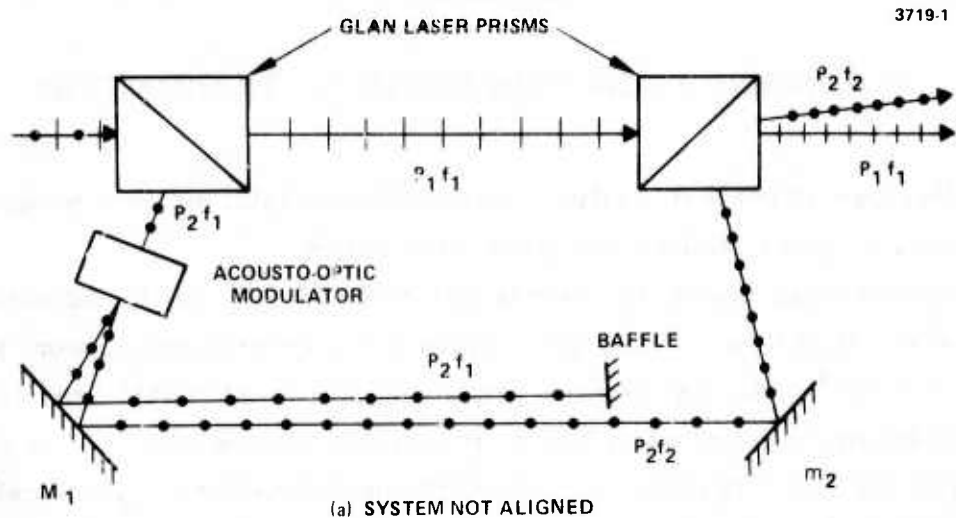


Figure F-1. Optical system modification for initial alignment.

second glan laser prism and the 30 in. focal length lens. The mirror is first adjusted to retroreflect the laser output polarization P_1 back through the system and then the $\lambda/4$ waveplate is rotated until the polarization P_1 is the same as P_2 . The retrodirected wave P_1 then exits from the second glan laser prism at exactly the proper angle and position that P_2 should enter the prism. By alternately adjusting mirrors M_1 and M_2 both beams can be made to reflect from each mirror at the same points (such that A' falls on A and B falls on B'). This method is facilitated by attaching a piece of paper first to one mirror and adjusting the other mirror and then vice versa. Because of proximity of mirror 1 to the acousto-optic modulator, the diffracted and undiffracted beams are not well resolved and some estimation of spot position was required. The longer the distance between the mirrors and the other optical elements the easier this alignment procedure becomes. In the field experiment it will be necessary to use as much bench space as feasible for this part of the system in order to minimize alignment time.

I. Helium Neon Laser Modulator Prealignment

An analytic study of the use of a helium neon laser to prealign the modulator system was performed during this program. The angle between the acoustic transducer face and the incident optical beam is given by

$$\frac{\theta}{2} = \frac{f_s \lambda_L}{2v_s} \quad (1)$$

where f_s is the ultrasonic frequency, λ_L is the wavelength of light and v_s is the sound velocity in the diffracting medium. If it is desired to align the laser for 150 MHz at the ruby laser wavelength of 6943 Å a proportionality equation can be written in the form:

$$f_{s1} \lambda_{L1} = f_{s2} \lambda_{L2}$$

or

(2)

$$f_{s2} = f_{s1} \frac{\lambda_{L1}}{\lambda_{L2}}$$

Using $f_{s1} = 150 \times 10^6 \text{ Hz}$, $\lambda_{L1} = 6943 \text{ Å}$, $\lambda_{L2} = 6328 \text{ Å}$ we find $f_{s2} = 164.6 \times 10^6 \text{ Hz}$. Thus using an rf drive frequency of 164.6 MHz and a 6328 Å helium neon alignment laser, it is feasible to prealign the acousto-optic modulator system for ruby laser operation provided the two laser beams are collinear and the frequency is changed back to 150 MHz when the ruby laser is operated. This technique was not useful in the set of experiments performed on this contract because the glan laser prisms had output windows that were not perpendicular to the initially reflected polarization waves. Thus when the wavelength was changed from 6943 to 6328 Å the straight through polarization wave P_1 was undeviated but the reflected orthogonal polarization wave P_2 underwent refraction and exited at different angles for the two wavelengths. A different prism design with all exit and entrance windows perpendicular to the entering and exiting polarizations will eliminate this problem. Additionally it was found that with a sufficiently high repetition rate laser the use of helium neon prealignment may be avoided completely because the diffracted beam can be visually or electronically monitored while the modulator orientation is manipulated for optimum modulation.

APPENDIX G

PULSE TESTING OF RCA C31094A PHOTOMULTIPLIER

The tube manufacturer (RCA) states that the output impedance of the tube must be matched using 50 Ω coaxial components. Since our oscilloscope (Tektronix 7904) uses BNC input connectors, we used BNC connectors throughout our optical heterodyne tests. Using a time domain reflectometer we later found that BNC connectors can produce significant impedance mismatch when used over a broad frequency bandwidth (400 MHz). Similar mismatch effects occurred at the input terminals to one of the rf preamplifiers and the filters used in the heterodyne experiments. An impedance mismatch will cause fast rise signals to reflect back into the photomultiplier where reflection occurs at the anode. Thus a single pulse can be converted into a series of pulses. Ordinarily the 30 nsec Gaussian shaped optical pulse does not have enough spectrum to excite this ringing effect, but when sufficiently low light levels are employed, quantum noise effects can give rise to high frequency components in the pulse. Another effect observed in the tests was that light leaking into the photomultiplier after the optical attenuator due to the presence of multiple optical paths could yield short duration pulses which could cause the system to ring.

In all of the tests reported below the photomultiplier output was carefully matched using general radio components and RG8U cables to minimize loss. Where the signals were coupled into the oscilloscope a 10x (20 dB) attenuator was placed before the General Radio to BNC adapter to provide isolation. The input impedance match of an Avantek wide-band amplifier fitted with high frequency connectors was found to be satisfactory for use as a photomultiplier post amplifier for use in some of the tests. Several photomultiplier dc biasing networks were available for the tests. One of these (AJ2219) was designed for fastest rise time and highest gain. The other network was designed

for the highest linear output current and showed poorer rise time and some pulse shape distortion. Figure G-1(a) shows the fast network photomultiplier response to an 18 nsec (FWHM) pulse at an attenuated power level of 4×10^{-7} W. The number of photocathode electrons in the pulse is approximately 1100. For comparison the response of an ITT photodiode with known (subnanosecond) response time to the laser output is shown in Fig. G-1(b). The pulse shapes are very similar with the photomultiplier output pulse being slightly wider and showing slight noise. This quantum noise is absent in the photodiode because the number of photons collected is many orders of magnitude larger (the PMT gain is 10^6).

The signal to noise ratio in a quantum noise limited detector is given by

$$\frac{S}{N} = \frac{\eta P}{h\nu B} \quad (1)$$

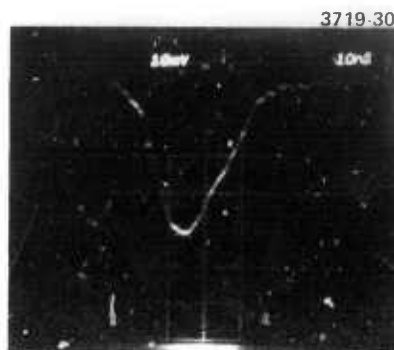
Where η is the photocathode quantum efficiency, P is the incident optical power, $h\nu$ is the energy per photon and B is the receiver bandwidth.

This may also be written as

$$\frac{S}{N} = \frac{\eta E / \Delta T}{h\nu B} \quad (2)$$

where E is the energy of the optical pulse in joules and ΔT is the full width half maximum time duration of a Gaussian like pulse. The quantity $\eta E / h\nu$ is the number of photocathode generated electrons in the pulse (N_c) so that this can be written as

$$\frac{S}{N} = \frac{N_c}{B\Delta T} \quad (3)$$

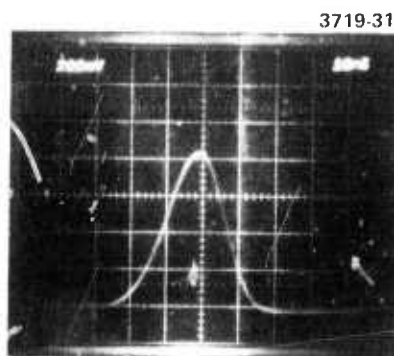


(a) PMT RESPONSE TO SINGLE MODE
Q SWITCHED ATTENUATION LASER

$$P \approx 4 \times 10^{-7} \text{ W}$$

$$n_c = 1100$$

$$n = 1.1 \times 10^9$$



(b) PHOTO DIODE RESPONSE TO
SINGLE MODE Q SWITCHED
LASER

Figure G-1.
Comparative response of photo-
multiplier and photodiode to
single mode laser pulse.

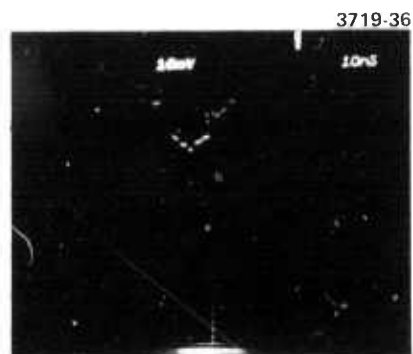
In the present case $N_c = 1100$, $B = 4 \times 10^8$ Hz, $\Delta T \approx 20$ nsec so that the signal to noise ratio at the peak is

$$\frac{S}{N} = \frac{1100}{4 \times 10^8 \times 20 \times 10^{-9}} = \frac{1100}{8} = 137 \text{ (21 dB)}$$

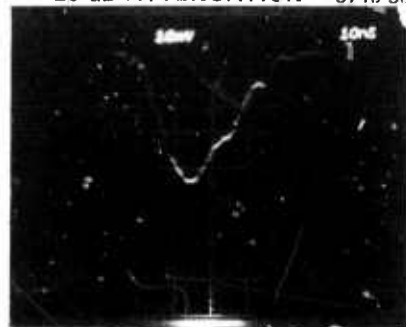
At other points in the pulse the S/N is correspondingly less. Thus the ripple (of the order of 0.7%) observed in the PMT output is consistent with quantum noise effects rather than tube oscillation.

The effects of optical pulse attenuation are shown in Figs. G-2(a), (b), and (c) where the number of photocathode generated electrons are 440, 910 and 1100. The peak response is approximately linear with power and the signal to noise ratio degrades in proportion to the number of photoelectrons. For the weakest signal (4400 electrons) the signal to noise ratio is 55 (17.4 dB) corresponding to a ripple of 1.8%. This result is in agreement with the observable data. Figure G-2(d), (e), and (f) is a series of data on amplifier impedance matching to the photomultiplier output. We selected an available Avantek AV8 amplifier with 400 MHz bandwidth for this application. Because the amplifier did not have response to dc a dc bias tee and an output coupling capacitor were used at the PMT output. A 20 dB padding attenuator was also used at the input connector to the oscilloscope to avoid mismatch effects. Figure G-2(d) shows the unamplified pulse. Figure G-2(e) shows the pulse passed first through a 24 dB amplifier and then through a 26 dB attenuator. Figure G-2(f) shows the signal after first passing through 26 dB of attenuation and then 24 dB of gain. No significant pulse shape distortion was observed for either case where amplification was used, although slight amplifier saturation is indicated in Fig. G-2(e) by virtue of the peak flattening and pulse undershoot.

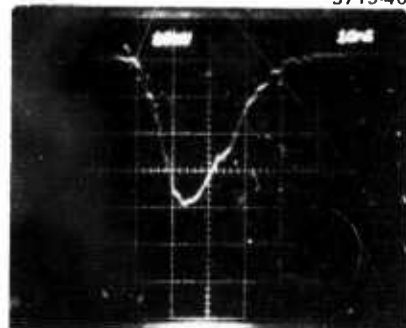
The motivation for this series of experiments was to explain the anomalous PMT responses observed in the heterodyne tests. Early



(a) $P = 1.6 \times 10^{-7} \text{ W}$
 $n_c = 440$
 $n = 4.4 \times 10^8$
 20 dB ATTENUATION 3719-38



(c) $P = 3.3 \times 10^{-7} \text{ W}$
 $n_c = 910$
 $n = 9.1 \times 10^8$
 20 dB ATTENUATION 3719-40



(e) $P = 4 \times 10^{-7} \text{ W}$
 $n_c = 1100$
 $n = 1.1 \times 10^9$



(b) $P = 4 \times 10^{-7} \text{ W}$
 0 dB ATTENUATION



(d) $P = 4 \times 10^{-7} \text{ W}$
 24 dB AMPLIFICATION
 26 dB ATTENUATION



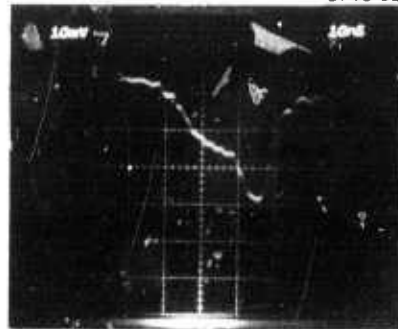
(f) $P = 4 \times 10^{-7} \text{ W}$
 26 dB ATTENUATION
 24 dB AMPLIFICATION

Figure G-2. Photomultiplier fast network response and amplifier impedance matching.

in this measurement series various anomalies were observed which were subsequently traced to multipath effects, these due to leakage of light into the PMT which had not passed through an optical neutral density attenuator, and light which had reflected from the walls and various parts of the apparatus. Careful baffle construction eliminated this problem but the anomalies are shown here for future reference. Figure G-3(a) and (b) show a type of multipath pulse distortion which can be resolved into a direct short pulse and a diffuse wide pulse. Figure G-3(c) and (d) show the effect of several different pulses arriving simultaneously but at different power levels. The gain in this case is 20 dB greater.

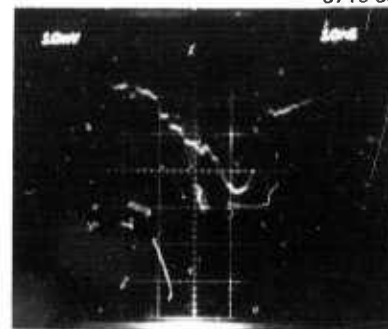
Time response tests were also made on a high linear current network for this PMT with less satisfactory results. In general the PMT and network tended to ring more easily and the pulse rise time and time width were distorted. The peak response was linear with power for larger signal levels but greater pulse distortion was evident at lower signal levels than observed in the case of the fast rise network.

3719-32



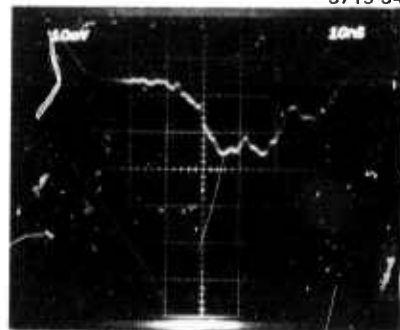
(a) MULTIPATH
TIME RESPONSE

3719-33



(b) MULTIPATH
TIME RESPONSE

3719-34



(c) MULTIPATH TIME
RESPONSE WITH (10x)
SIGNAL ATTENUATION

3719-35



(d) MULTIPATH TIME
RESPONSE WITH (10x)
SIGNAL ATTENUATION

Figure G-3. Laser multipath effects using fast photo-multiplier network.

APPENDIX H

OPTIONAL FIBER PROPAGATION LOSS EXPERIMENTS

A cw helium neon laser test system was accordingly implemented to make the attenuation measurements with greater precision. In this measurement procedure the input and output end of each fiber was separated from the bundle. A set of input and output cladding mode suppressors was needed to isolate the core propagation data from the cladding mode effects which affect shorter fibers. Part of the incident power was sampled with a beam splitter and attenuators and the measurements were made with the aid of ratio measuring electronics. The sample and output detectors were silicon photodiodes. The fiber position was adjusted until maximum transmission was obtained for the fiber and the ratio value observed on a Kiethly digital voltmeter. The ratio measurement technique was needed to correct for short fluctuations of the laser output power.

The mode strippers consisted of 2 in. long black velvet sandwiches impregnated with glycerol, an index matching fluid. Earlier grooved slabs of black glass were tried as mode strippers but the fibers were broken upon insertion into the grooves. The mode strippers would be more effective if they were made longer.

Two sets of data were taken and are shown in Fig. H-1. Due to the large time consumed in handling each set of fiber ends and to occasional fiber breakage, it was not possible to obtain two complete sets of data. However, a sufficient number of points was taken to establish a curve which verifies the expected fiber attenuation of less than 10 dB/km. The measurement repeatability was within 1 dB and the largest deviation from the best fit curve was less than 2 dB. In conclusion the largest loss measured was of the order of 2 dB and was attributed to end face results.

PRECEDING PAGE BLANK-NOT FILMED

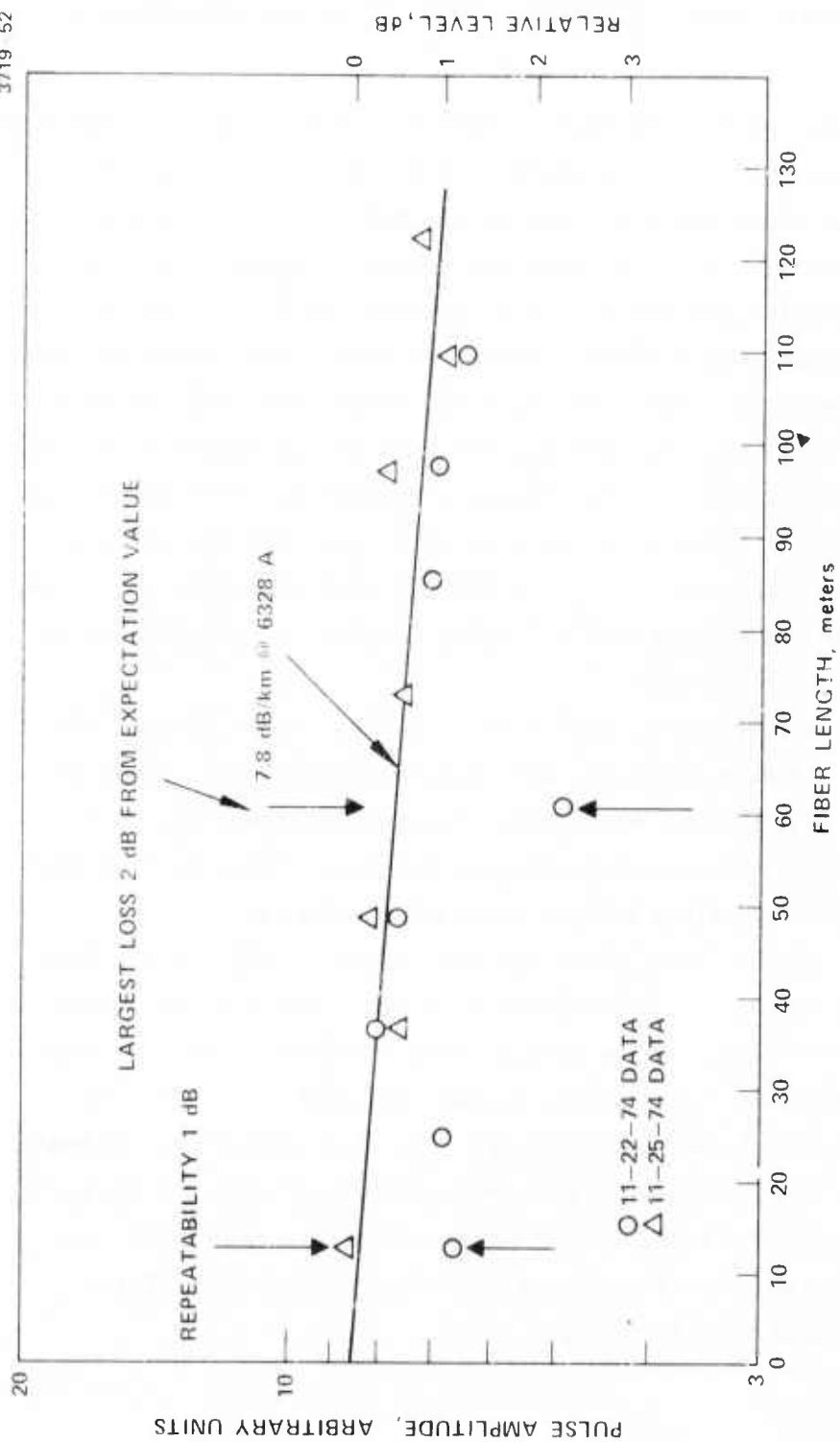


Figure H-1. Helium-neon fiber loss measurements.

A photograph of the test apparatus is shown in Fig. H-2 and the details of the output mode suppressor and photodetector are shown in Fig. H-3.

These results tend to substantiate the theory that excitation of cladding mode propagation at the shorter delays adversely influences the attenuation measurements and that the mode stripping devices have not been made long enough to completely eliminate these effects. In the experiment option the optical fibers are to have the cladding stripped from the input ends to provide the highest density of packing. Thus the cladding modes would not be excited by the target signals and the need for mode strippers may cease to exist.

The fiber optic delay times were checked by taking a series of photographs of the entire trace with a selected portion intensified and then displaying on an expanded scale the intensified pulses.

M10702

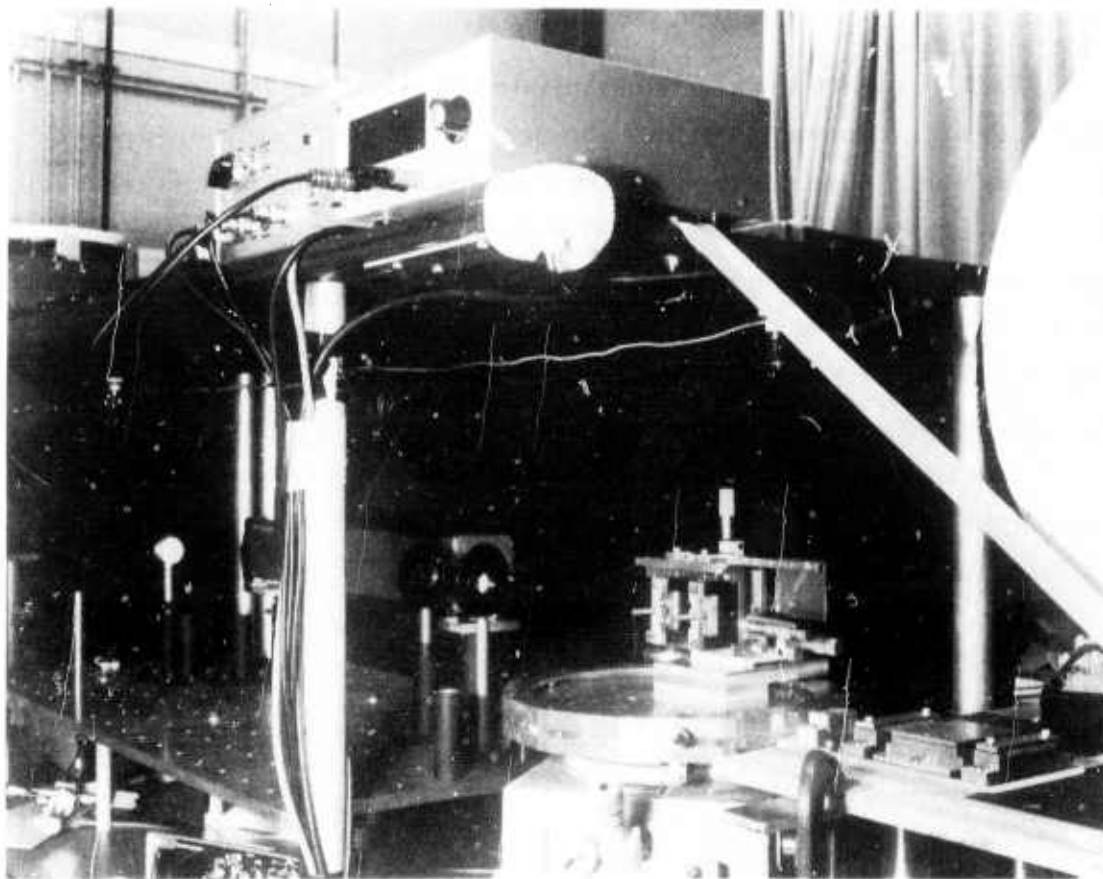


Figure H-2. Fiber loss measurement apparatus.

M10703

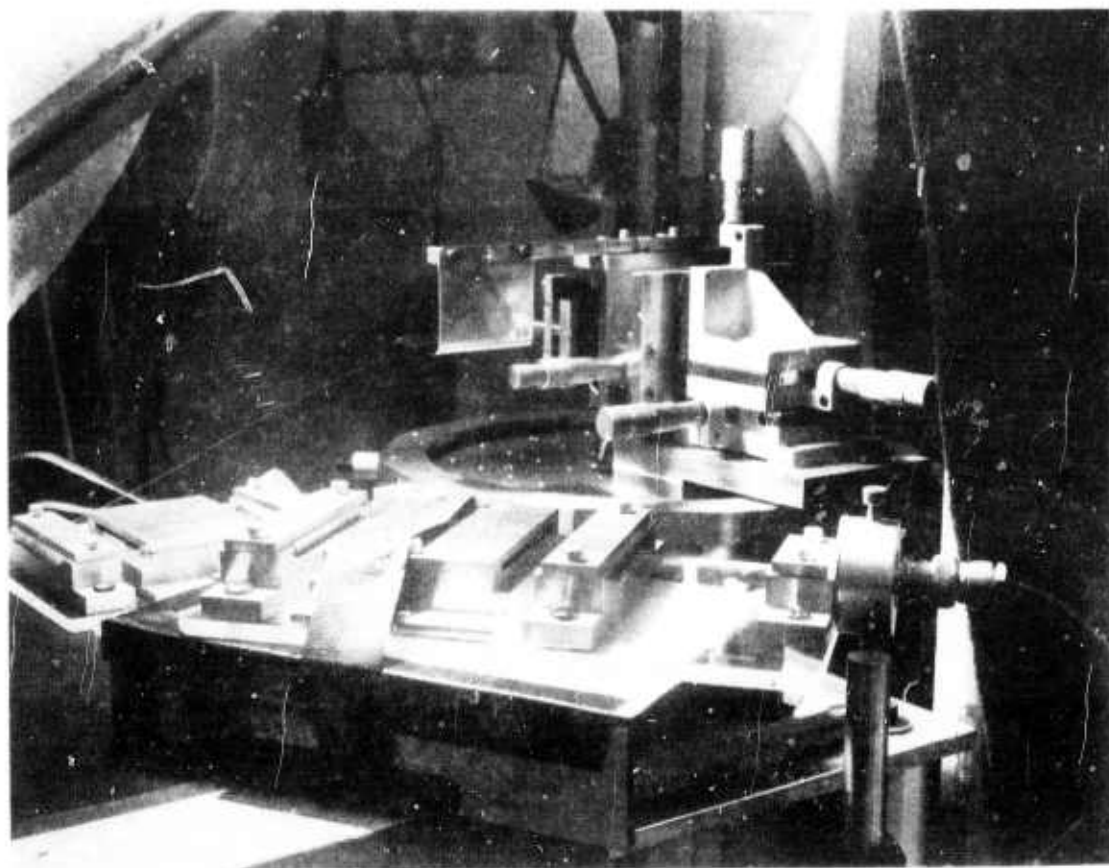


Figure H-3. Closeup view of single fiber measurement setup.

APPENDIX I

CLADDING REMOVAL FROM OPTICAL FIBERS

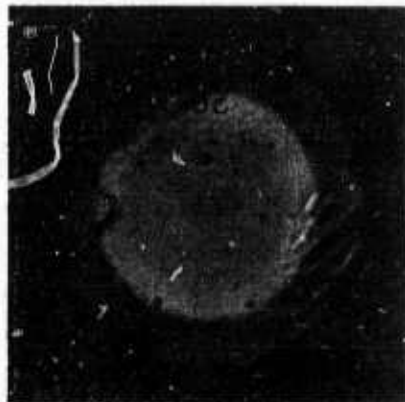
In order to obtain a high optical packing density in the time domain multiplex PRM system it is necessary to remove the glass outer cladding which is an integral part of the fiber. A series of experiments was performed to accomplish this goal using a diluted hydrofluoric acid solution. Several preliminary dilutions were tried until a reasonable etching time and rate were obtained. The final etch formula was 50% HF and 50% H_2O . The removal rate was approximately 0.000066 in. per minute. The time to remove the cladding was approximately 20 minutes with the etch constantly rotated about the fiber at 150 rpm. The nominal fiber diameter was 0.005 in. with a core diameter of 0.0034 in. The fibers were uniformly etched over the total length immersed.

Figure I-1(a) shows the fiber cross section before etching to be 0.0049 in. Figure I-1(b) shows the cross section after etching to be 0.0036 in. with some degradation of the end face. Figure I-1(c) shows the etched fiber cross section after being recleaved to show the true cross section. A similar set of results is shown in Fig. I-2 for a larger diameter fiber (0.0052 in.) with a larger diameter core. Figure I-3 shows the average diameter of the fibers before and after etching showing very uniform side walls for both cases.

In conclusion it has been shown that the technology for fiber cladding removal is known and is directly applicable to the problem of achieving high fiber packing densities in the time multiplex array.

PRECEDING PAGE BLANK NOT FILMED

3719-42



(a) MICROGRAPH OF
CLEAVED FIBER
CROSS SECTION, 0.0049 in.

3719-43



(b) MICROGRAPH OF FIBER END
AFTER 20 min ETCH
CROSS SECTION, 0.0036 in

3719-44



(c) MICROGRAPH OF FIBER
CROSS SECTION
AFTER 20 min ETCH

Figure I-1. Chemical removal of glass outer cladding from corning multimode fiber.

3719-45



(a) MICROGRAPH OF
CLEAVED FIBER
CROSS SECTION, 0.0052 in.

3719-46



(b) MICROGRAPH OF FIBER END
AFTER 20 min ETCH
CROSS SECTION, 0.0043 in.

3719-47



(c) MICROGRAPH OF FIBER END
AFTER 25 min ETCH
CROSS SECTION, 0.0041 in.

Figure I-2. Chemical removal of glass outer cladding from corning multimode fiber.

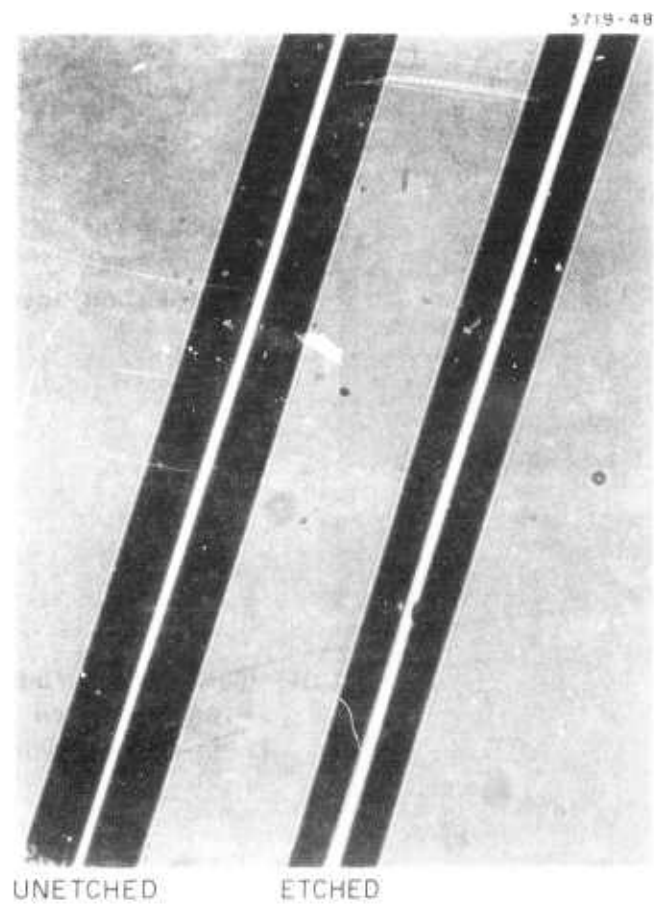


Figure I-3. Micrograph of fiber before and after etching.

MISSION of Rome Air Development Center

RADC is the principal AFSC organization charged with planning and executing the USAF exploratory and advanced development programs for information sciences, intelligence, command, control and communications technology, products and services oriented to the needs of the USAF. Primary RADC mission areas are communications, electromagnetic guidance and control, surveillance of ground and aerospace objects, intelligence data collection and handling, information system technology, and electronic reliability, maintainability and compatibility. RADC has mission responsibility as assigned by AFSC for demonstration and acquisition of selected subsystems and systems in the intelligence, mapping, charting, command, control and communications areas.

